

METAL POWDER PRODUCTION BY PYROLYSIS OF METAL OXALATES AND CARBONYL CLUSTERS

by

Joanne Hayley Smith
B.Sc. (Hons), (Natal)

Submitted in partial fulfillment of the academic
requirements for the degree of
Master of Science
in the
School of Chemical and Physical Sciences,
University of Natal

Pietermaritzburg
June 2001

ABSTRACT

Chapter One serves as an introduction to, and background information, on the thermal decomposition of metal oxalates and homonucleus carbonyl clusters. Emphasis is placed on the compounds under investigation, namely the oxalates of iron(II), cobalt(II) and nickel(II) oxalate dihydrate and their corresponding binary and ternary compounds, as well as triiron dodecacarbonyl and tetracobalt dodecacarbonyl. Topics specifically addressed are their structures as well as the thermodynamics of the dehydration and decomposition of compounds of this type. Given this background, the overall aims of the work are presented. These include finding the reaction conditions to form metal powders from metal oxalates, and a preliminary study of carbonyl clusters to see if they too may be used in the production of metal powders.

Chapter Two gives the results of the dehydration and decomposition of the metal oxalates, characterised by way of infrared, scanning electron microscopy, X-ray diffraction and thermogravimetric analysis. The compounds under investigation are those of the single oxalates of iron, cobalt and nickel; the binary systems of Fe-Co, Fe-Ni and Co-Ni, in the molar ratios of 3:1, 1:1 and 1:3 for each system; and the ternary oxalate system in the molar ratios of Fe₁:Co₁:Ni₁, Fe₈:Co₁:Ni₁, Fe₁:Co₈:Ni₁ and Fe₁:Co₁:Ni₈. It was found that under certain reaction conditions all these compounds, excluding the ferrous oxalate dihydrate, decompose to the metal. It was found through experiments to modify the morphology of the crystals under investigation that the decomposition product is controlled by the crystal lattice system the starting material is synthesised in. When in the cobalt/nickel oxalate α -crystal system, decomposition is to the metal, or in the case of the binary and ternary systems, to the alloy. If the oxalate is synthesised in the crystal system of the iron oxalate, the resultant decomposition product is the respective oxide. Experiments were carried out on the iron/cobalt binary system to prove this hypothesis. Depending on the conditions of synthesis, the iron/cobalt binary system can form in either the crystal system analogous to iron (1), or analogous to cobalt (2). The products of pyrolysis for each case differs, with (1) decomposing to the oxide and (2) decomposing to the alloy.

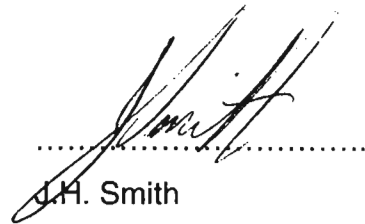
Chapter Three is a brief, preliminary study describing the thermal decomposition of triiron dodecacarbonyl and tetracobalt dodecacarbonyl. Characterisation of the pyrolysis products is given by infrared, scanning electron microscopy, X-ray diffraction and thermogravimetric analysis. A tentative theory for their decomposition route under an atmosphere of nitrogen is given. It was found that neither compound decomposed fully to the central metal, but that a mixture of oxide and metal were left. The conclusion reached from this study was that neither carbonyl under investigation was particularly successful. Although in both instances metal was produced, both contained large amounts of the respective oxide. This makes them unsuitable for an industrial application to form metal powders.

Chapter Four describes in detail the all the experimental, materials, methods, techniques and equipment used in this study.

DECLARATION

The experimental work described in this dissertation was carried out in the School of Chemical and Physical Sciences, University of Natal, Pietermaritzburg, under the supervision of Professor John S. Field and Doctor Ray Chapman.

These studies represent original work by the author and have not otherwise been submitted in any form for any degree or diploma to any University. Where use has been made of the work of others it is duly acknowledged in the text.



.....
J.H. Smith

We hereby certify that this statement is correct.

.....
Professor R.J. Haines
Supervisor

.....
Professor J.S. Field
Co-Supervisor

Pietermaritzburg
June 2001

TABLE OF CONTENTS

ABSTRACT	ii
DECLARATION	iii
LIST OF FIGURES	viii
LIST OF TABLES	xi
ACKNOWLEDGEMENTS	xiii

LITERATURE REVIEW

1. INTRODUCTION	1
1.1 THERMAL DECOMPOSITION OF OXALATES	2
1.1.1 Simple Bivalent Transition Metal Oxalates	3
1.1.1.1 Structures	3
1.1.1.2 Dehydration.....	7
1.1.1.3 Thermodynamics of Thermal Decomposition.....	9
1.1.1.4 Kinetics and Mechanism of Thermal Decomposition	15
1.1.1.5 Important Control Parameters	16
1.1.2 Solid Solutions of Bivalent Transition Metal Oxalates	18
1.2 THERMAL DECOMPOSITION OF METAL CARBONYLS	19
1.2.1 Structure and Bonding in Binary Metal Cluster Carbonyls	20
1.2.1.1 Bonding.....	20
1.2.1.2 Structures	22
1.2.2 Thermal decomposition of Homonuclear Metal Cluster Carbonyls	
25	
1.2.2.1 Thermal Decomposition of Unsupported $Fe_3(CO)_{12}$	25
1.2.2.2 Thermal Decomposition of Unsupported $Co_4(CO)_{12}$	27
1.3 AIMS OF THIS WORK	28

INVESTIGATION OF METAL OXALATES

2. INTRODUCTION	29
2.1 SYNTHESIS AND CHARACTERIZATION OF SINGLE OXALATES	29
2.1.1 C and H Microanalysis	30
2.1.2 IR Analysis	30

2.1.3	Particle Size Analysis and Scanning Electron Microscopy (SEM)	32
2.1.4	X-Ray Powder Diffraction (XRD)	34
2.2	PYROLYSIS STUDIES OF SINGLE OXALATES	34
2.2.1	Thermogravimetric Analysis	35
2.2.2	Characterisation of Furnace Products	37
2.2.2.1	XRD	37
2.2.2.2	SEM	39
2.3	SYNTHESIS AND CHARACTERISATION OF BINARY OXALATES	41
2.3.1	C and H Microanalysis	41
2.3.3	Particle Size Analysis and SEM	44
2.3.4	XRD	49
2.3.4.1	Iron-Cobalt Binary Oxalate System	49
2.3.4.2	Iron-Nickel Binary Oxalate System	51
2.3.4.3	Cobalt-Nickel Binary Oxalate System	53
2.4	PYROLYSIS STUDIES OF BINARY OXALATES	56
2.4.1	Thermogravimetric Analysis	56
2.4.1.1	Iron-Cobalt System	56
2.4.2.1	Iron-Cobalt Binary Oxalate System	63
2.4.2.2	Iron-Nickel Binary Oxalate System	65
2.4.2.3	Cobalt-Nickel Binary Oxalate System	65
2.5	SYNTHESIS AND CHARACTERISATION OF TERNARY OXALATES	72
2.5.1	C and H Microanalysis	73
2.5.3	Particle Size Analysis and SEM	75
2.5.4	XRD	78
2.6	PYROLYSIS STUDIES OF TERNARY OXALATES	82
2.6.1	Thermogravimetric Analysis	82
2.6.2.1	XRD	86
2.6.2.2	SEM	89
2.7	MORPHOLOGY VARIANCE	89
2.7.1	Synthesis and Characterisation of Cobalt Oxalate Dihydrate	92
2.7.2	Synthesis and Characterisation of Equimolar Binary Iron-Cobalt Oxalate	97
2.8	CONCLUSIONS	102

INVESTIGATION OF METAL CARBONYL CLUSTERS

3. INTRODUCTION	105
3.1 TRIIRON DODECACARBONYL	105
3.1.1 Characterisation of Thermal Decomposition Products.....	106
3.1.1.1 Thermogravimetric Analysis	106
Tube Furnace.....	108
3.1.1.2 IR.....	108
3.1.1.3 XRD.....	109
3.1.1.4 SEM.....	111
3.2 TETRACOBALT DODECACARBONYL.....	114
3.2.1 Characterisation of Thermal Decomposition Products.....	114
3.2.1.1 Thermogravimetric Analysis	114
3.2.1.2 Tube Furnace.....	118
3.2.1.3 IR.....	118
3.2.1.4 XRD.....	118
3.2.1.5 SEM.....	119
3.3 CONCLUSION	122
EXPERIMENTAL	
4. INTRODUCTION	123
4.1.1 Oxalate Chemistry	123
4.1.2 Carbonyl Chemistry.....	123
4.2 METHODS.....	123
4.2.1 4.2.1.Synthesis of Bivalent Transition Metal Oxalates	123
4.2.2 Pyrolysis	125
4.2.2.1 Pyrolysis of Metal Oxalates	125
4.2.2.2 Pyrolysis of Metal Carbonyls	126
4.3 INSTRUMENTS	126
4.4 TECHNIQUES.....	127
REFERENCES.....	128
APPENDIX I.....	135

LIST OF FIGURES

Figure 1.1 Molecular structure of the uncoordinated oxalate species, $C_2O_4^{2-}$, with D_{2d} symmetry [41].....	3
Figure 1.2 Structural units of bivalent transition metal oxalates, where $M = Fe^{2+}$, Ni^{2+} or Co^{2+} [45] a) the mono-oxalato species, (b) the bisoxalato species, (c) the polymer.....	5
Figure 1.3 Structure of bivalent, transition metal oxalates (where M is Fe^{2+} , Ni^{2+} or Co^{2+}).....	11
Figure 1.4 Ellingham diagram showing the relationship between ΔG_6 and ΔG_7 [71]	13
Figure 1.5 Dependence of decomposition temperature on the ionic radius of the metal for oxalates of bivalent transition metals [62].....	14
Figure 1.6 Bonding modes of CO: (a) terminal (T), (b) doubly bridged (B), (c) triply bridged (B), and (d) the (μ, η^2-CO) entity	21
Figure 1.7 Structure of $Fe_3(CO)_{12}$	23
Figure 1.8 Structure of $Co_4(CO)_{12}$	24
Figure 2.1 SEM photograph of the single oxalate dehydrates. (a) iron(II), (b) cobalt(II) and nickel(II)	33
Figure 2.2 XRD comparison of single oxalates.....	36
Figure 2.3 TGA of ferrous, cobalt and nickel oxalate dihydrate under an N_2 atmosphere at a ramp rate of $5^\circ C$ per minute.	37
Figure 2.4 XRD patterns of cobalt and nickel, formed after pyrolysing $CoC_2O_4 \cdot 2H_2O$ and $NiC_2O_4 \cdot 2H_2O$ respectively, under a nitrogen atmosphere.	38
Figure 2.5 XRD pattern of Fe_3O_4 , formed after pyrolysing $FeC_2O_4 \cdot 2H_2O$ under nitrogen atmosphere.....	39
Figure 2.6 SEM photographs of single oxalates of (a) Fe, (b) Co and (c) Ni pyrolysed under an N_2 atmosphere at $390^\circ C$ for 1 hour	40
Figure 2.7 SEM photographs of the binary coprecipitated oxalates of Fe and Co in the ratios of (a) Fe3:Co1, (b) Fe1:Co1 and (c) Fe1:Co3.....	46
Figure 2.8 SEM photographs of the binary coprecipitated oxalates of Fe and Ni in the ratios of (a) Fe3:Ni1, (b) Fe1:Ni1 and (c) Fe1:Ni3	47

Figure 2.9 SEM photograph of the binary coprecipitated oxalates of Co and Ni in the ratios of (a) Co ₃ :Ni ₁ , (b) Co ₁ :Ni ₁ and (c) Co ₁ :Ni ₃	48
Figure 2.10 XRD pattern comparison of physical mixtures and coprecipitated iron-cobalt binary system.....	50
Figure 2.11 XRD pattern comparison of physical mixtures and coprecipitated iron-nickel binary system	52
Figure 2.12 XRD pattern comparison of physical mixtures and coprecipitated cobalt-nickel binary system.....	54
Figure 2.13 TGA traces of iron-cobalt binary system, at 5°C/min under N ₂	58
Figure 2.14 TGA traces of iron-nickel binary system, at 5°C/min under N ₂	60
Figure 2.15 TGA traces of iron-nickel binary system, at 5°C/min under N ₂	62
Figure 2.16 XRD pattern of Fe-Co oxalate system pyrolysis products	64
Figure 2.17 XRD pattern of Fe-Co oxalate system pyrolysis products	66
Figure 2.18 XRD pattern of Fe-Co oxalate system pyrolysis products	67
Figure 2.19 SEM photograph of binary coprecipitated oxalates of Fe and Co in the ratios of (a) Fe ₃ :Co ₁ , (b) Fe ₁ :Co ₁ and (c) Fe ₁ :Co ₃ pyrolysed under N ₂ atmosphere at 390°C for 1 hour.....	69
Figure 2.20 SEM photograph of binary coprecipitated oxalates of Fe and Co in the ratios of (a) Fe ₃ :Co ₁ , (b) Fe ₁ :Co ₁ and (c) Fe ₁ :Co ₃ pyrolysed under N ₂ atmosphere at 390°C for 1 hour.....	70
Figure 2.21 SEM photograph of binary coprecipitated oxalates of Fe and Co in the ratios of (a) Fe ₃ :Co ₁ , (b) Fe ₁ :Co ₁ and (c) Fe ₁ :Co ₃ pyrolysed under N ₂ atmosphere at 390°C for 1 hour.....	71
Figure 2.22 SEM photographs of ternary coprecipitated oxalates of Fe, Co and Ni in the ratios of (1) Fe ₁ :Co ₁ :Ni ₁ and (2) Fe ₈ :Co ₁ :Ni ₁	76
Figure 2.23 SEM photograph of the equimolar mixture of iron(II), cobalt and nickel oxalates.....	78
Figure 2.24 XRD patterns of ternary oxalates (a) coprecipitated and (b) mixtures	80
Figure 2.25 TGA traces showing a comparison between coprecipitated ternary oxalates and the corresponding mechanical mixtures. (1) Equimolar sample, (2) Fe ₈ :Co ₁ :Ni ₁	83
Figure 2.26 Thermal decomposition products of ternary coprecipitated oxalates.	87

<i>Figure 2.27 SEM photographs of ternary coprecipitated oxalates of Fe, Co and Ni in the ratios of (a) Fe1:Co1:Ni1 and (b) Fe8:Co1:Ni1 pyrolysed under N₂ atmosphere at 390°C for 1hour.....</i>	<i>90</i>
<i>Figure 2.28 Malvern particle size distribution of original CoC₂O₄.2H₂O and modified CoC₂O₄.2H₂O (µm).....</i>	<i>93</i>
<i>Figure 2.29 SEM photographs showing the crystal morphologies of the two different methods of preparation of cobalt oxalate dihydrate. (1) conventional treatment, (2) modified treatment.....</i>	<i>94</i>
<i>Figure 2.30 TGA curves showing comparison of two different samples of cobalt oxalate. (conditions: ramp rate of 5°C/min under N₂).....</i>	<i>95</i>
<i>Figure 2.31 XRD comparison of differing synthetic routs of cobalt oxalate</i>	<i>96</i>
<i>Figure 2.32 SEM photographs showing a comparison between the (1) original and (2) modified equimolar Ferrous/Cobalt binary coprecipitated oxalates</i>	<i>98</i>
<i>Figure 2.33 XRD patterns of the single oxalates of iron and cobalt with the different preparation routes of binary oxalate Fe1:Co1</i>	<i>101</i>
<i>Figure 2.34 TGA curves showing the differing temperatures of dehydration and decomposition of the different equimolar iron-cobalt binary oxalates.....</i>	<i>102</i>
<i>Figure 3.1 TGA curves of Fe₃(CO)₁₂ at two different heating rates</i>	<i>107</i>
<i>Figure 3.2 IR spectra of Fe₃(CO)₁₂ and product after pyrolysis at 100°C for 24 hours under a nitrogen atmosphere.</i>	<i>108</i>
<i>Figure 3.3 XRD patterns of triiron dodecacarbonyl pyrolysis products, after 24 hours at 100°C and 900°C respectively.</i>	<i>110</i>
<i>Figure 3.4 SEM photograph of Fe₃(CO)₁₂.....</i>	<i>112</i>
<i>Figure 3.5 SEM photograph of Fe₃(CO)₁₂ pyrolysed for 3 hours at 100°C.</i>	<i>112</i>
<i>Figure 3.6 SEM photographs of Fe₃(CO)₁₂ pyrolysed for 24 hours at 100°C (a) 1000 x and (b) 100 x.....</i>	<i>113</i>
<i>Figure 3.7 TGA curve of Co₄(CO)₁₂ at a heating rate of 5°C/min under N₂</i>	<i>116</i>
<i>Figure 3.8 TGA curve of Co₄(CO)₁₂ at a heating rate of 1°C/min under N₂</i>	<i>117</i>
<i>Figure 3.9 Pyrolysis products of tetracobalt dodecacarbonyl, showing patterns of CoO and Co.</i>	<i>120</i>
<i>Figure 3.10 SEM photograph of Co₄(CO)₁₂ pyrolysed for 24 hours at 100°C, magnification at (a) 100 x and (b) 5000 x.....</i>	<i>121</i>

LIST OF TABLES

<i>Table 1.1 Primary decomposition products of simple oxalates and the heats of formation (ΔH_e) per equivalent of corresponding metal oxide under N_2 [66]. ...</i>	<i>10</i>
<i>Table 2.1 Elemental analysis of Single Oxalates.....</i>	<i>30</i>
<i>Table 2.2 Infrared spectra and vibrational assignments for iron(II), cobalt(II) and nickel(II) oxalate dihydrate in the solid state.....</i>	<i>31</i>
<i>Table 2.3 Principal d-values (\AA) for single oxalates of cobalt and nickel.....</i>	<i>34</i>
<i>Table 2.4 Temperatures of dehydration and decomposition, and corresponding weight losses for ferrous, cobalt and nickel oxalates under N_2.....</i>	<i>35</i>
<i>Table 2.5 Percentage Yields of Binary Oxalates and Mole ratios used in the Binary Coprecipitation Reactions.....</i>	<i>42</i>
<i>Table 2.6 Elemental Analysis of Coprecipitated Binary Oxalates.....</i>	<i>42</i>
<i>Table 2.7 Infrared spectra and vibrational assignments for the Fe-Ni coprecipitated binary oxalates in different molar ratios.....</i>	<i>43</i>
<i>Table 2.8 Mean particle size of coprecipitated ternary oxalates.....</i>	<i>44</i>
<i>Table 2.9 Principal d^a-values (\AA) for the Fe-Co oxalate system^b.....</i>	<i>51</i>
<i>Table 2.10 Principal d^a-values (\AA) for the Fe-Ni binary oxalate system^b.....</i>	<i>53</i>
<i>Table 2.11 Principal d^a-values (\AA) for the Co-Ni binary oxalate system^b.....</i>	<i>55</i>
<i>Table 2.12 Temperatures of dehydration, decomposition and weight losses for binary coprecipitated iron-cobalt oxalate system under N_2 at ramp rate of $5^\circ/\text{min}$.....</i>	<i>57</i>
<i>Table 2.13 Temperatures of dehydration, decomposition and weight losses for binary coprecipitated iron-nickel oxalate system under N_2 at ramp rate of $5^\circ/\text{min}$.....</i>	<i>59</i>
<i>Table 2.14 Temperatures of dehydration, decomposition and weight losses for binary coprecipitated cobalt-nickel oxalate system under N_2 at ramp-rate $5^\circ/\text{min}$.....</i>	<i>61</i>
<i>Table 2.15 Principal d-values (\AA) for the pyrolysis products of the Fe-Co oxalate system.....</i>	<i>63</i>
<i>Table 2.16 Principal d-values (\AA) for the pyrolysis products of the Fe-Ni oxalate system.....</i>	<i>65</i>

<i>Table 2.17 Principal d-values (Å) for the pyrolysis products of the Co-Ni oxalate system.....</i>	<i>68</i>
<i>Table 2.18 Mole ratios and Percentage Yields used in the Ternary Coprecipitation Reactions</i>	<i>72</i>
<i>Table 2.19 Elemental Analysis of Coprecipitated Ternary Oxalates.....</i>	<i>73</i>
<i>Table 2.20 Infrared spectra and vibrational assignments for the coprecipitated ternary oxalates in different molar ratios.</i>	<i>74</i>
<i>Table 2.21 Mean particle size of coprecipitated ternary oxalates.....</i>	<i>75</i>
<i>Table 2.22 Principal d-values (Å) for ternary coprecipitated oxalates</i>	<i>82</i>
<i>Table 2.23 Temperatures of dehydration, decomposition and weight losses for ternary coprecipitated oxalates under N₂ at ramp rate of 5°/min.....</i>	<i>85</i>
<i>Table 2.24 Principal d-values (Å) for the pyrolysis products of the ternary oxalate system Fe1:Co8:Ni1 and Fe1:Co1:Ni8, and those for the pure metals of cobalt and nickel [51].</i>	<i>88</i>
<i>Table 2.25 Principal d values (Å) for the pyrolysis product of the ternary oxalate system Fe8:Co1:Ni1 and for pure metallic iron [51].....</i>	<i>88</i>
<i>Table 2.26 Mean particle size of the original cobalt oxalate dehydrate (1) and the modified form (2).</i>	<i>92</i>
<i>Table 2.27 Mean particle size of the original equimolar iron-cobalt oxalate (1) and the modified form (2).....</i>	<i>97</i>
<i>Table 2.28: IR data comparing the two equimolar iron-cobalt binary oxalate with the single oxalates of iron(II) and cobalt(II)</i>	<i>99</i>
<i>Table 2.29 Temperatures of dehydration and decomposition for equimolar iron-cobalt coprecipitated oxalate systems under N₂ at a ramp rate of 5°/min</i>	<i>100</i>
<i>Table 3.1 Comparison of TG analysis of Fe₃(CO)₁₂ at differing heating rates</i>	<i>106</i>
<i>Table 3.2 d-values (Å) of the pyrolysis products of Fe₃(CO)₁₂</i>	<i>109</i>
<i>Table 3.3 Comparison of TGA curves of Co₄(CO)₁₂ at differing heating rates....</i>	<i>115</i>
<i>Table 3.4 d values (Å) for the solid pyrolysis products of Co₄(CO)₁₂.....</i>	<i>119</i>
<i>Table 4.1 Mole ratios used in the Binary Coprecipitation Reactions</i>	<i>124</i>
<i>Table 4.2 Mole ratios used in the Ternary Coprecipitation Reactions</i>	<i>125</i>

AKNOWLEDGEMENTS

I would like to take the opportunity to thank De Beers Diamond Research Laboratories (DRL) for the funding and equipment they provided to make this investigation possible. I would also like to thank my supervisor Prof. John Field and my mentor Dr. Ray Chapman for their continued interest, input and ideas, without which I would not have been able to complete this dissertation.

Other notable contributions and help were gratefully received from Belinda White at the Centre for Electron Microscopy of Natal University, Pietermaritzburg, and Hester Burkes of the DRL. Prof. Jeff Hughes was invaluable with his help on X-ray diffraction. All the help of the men at the Mechanical Workshop, especially Paul Forder who was able to create new glassware essential to the research, was very much appreciated. I would also like to thank James Ryan who was on hand to fix anything I broke.

I would like to thank Barbara de Leeuw, who has been a great help and a supportive friend. Lastly, I would like to thank Justin Pooley for his help, support and encouragement, especially during the last stretch.

LITERATURE REVIEW

1. INTRODUCTION

The processes of metal powder preparation, and the fundamentals and principles that form their basis, are gaining interest due to the number of applications arising for these materials. The use of metals in the form of powders, films and coatings is gaining momentum for the production of catalysts, battery and fuel cells and electrodes [1]. The preparation of finely divided, micro- and nanometer scale particles as colloids or aggregates is a well-developed field that involves a variety of chemical and physical techniques [2,3]. The preparation procedure has a great effect on the characteristics of the products, such as particle size distribution, shape, microstructure, porosity, purity and reactivity.

Besides the so-called mechanical processes [4] that are already widely used for metal powder production on an industrial scale, (e.g. grinding and milling of crushable metals, granulation and atomization), various other processes are becoming increasingly important, such as the reduction of metal oxides and other compounds. Small noble-metal particles are commonly made by mild reduction [5-7]. Rieke and co-workers and others have reduced salts of the more active metals in ethereal or hydrocarbon solvents, either heterogeneously with alkali metals (slow), or homogeneously with radical anions of aromatic compounds, such as naphthalene (fast) [8-12]. The products of such reactions are highly reactive metal powders. Two more recent developments are reduction with alkali-metal organoborohydride solutions, such as $\text{NaB}(\text{Et})_3\text{H}$, which yields both single metals and alloys of the iron-group elements and the noble metals [13], and reduction with BH_4^- for Co, Ni, Au, Ag, Pt etc. [14]. These techniques are often aided with ultrasound [15,16]. Tsai *et al.* [17] have produced nanometer-size metal powders by homogeneous reduction with alkalides and electrides in aprotic solvents. Bimetallic colloids have also been produced by similar reduction methods [18-29]. These methods have resulted in the formation of extremely reactive metal particles with sizes between 10 and 100 nm [14]. Evaporation techniques [30, 31], matrix isolation (solvated metal atom dispersion) [32, 33], sol-gel processes [34],

electrochemical methods [35, 36] and pyrolysis precursors [37] have also been used to prepare small metal particles.

The thermal decomposition of various metal compounds is frequently used to prepare metal powders of high purity. Although these processes produce metal powders that are coarser than other techniques, the products are more stable and easier to produce on a large scale. Other advantages of thermal decomposition over reduction and other chemical methods are well-documented [38]. The two thermal decomposition processes concerned with in this study, are common methods for the preparation of metals and metal oxides, namely the thermal decomposition of a metal oxalate precursor $M(C_2O_4)_n$, and the decomposition of metal carbonyls, $M(CO)_n$.

1.1 THERMAL DECOMPOSITION OF OXALATES

The usual preparation of various ferromagnetic materials (alloys, ferrites and oxides) involves the solid reaction between two or more metals or metal oxides. These reactions generally require high temperatures in order to get the cations or metal atoms to diffuse over large distances ($\sim 10^4$ Å). Starting with metal ions in a solid solution can eliminate the need for this long-range diffusion and reduce the diffusion distance to that of the lattice spacing of a few Å [37]. Much of the work undertaken in this dissertation explores the dehydration and decomposition of the simple bivalent transition metal oxalates of iron, nickel and cobalt to the metal product, as well as of their binary and ternary solid solutions to form alloys. Dollimore [39] has extensively discussed the possibility of producing metal and alloy powders with very high surface areas by decomposition of the corresponding oxysalts.

1.1.1 Simple Bivalent Transition Metal Oxalates

The thermal decomposition of bivalent, transition metal oxalates takes place in two distinct steps. This is because most transition metal oxalates are hydrated, necessitating a definite and distinct dehydration step before actual decomposition can take place. Numerous researchers have extensively studied both these processes since the 1950's. Before these processes can be discussed, however, some understanding of the structure of the oxalates is needed, as is an understanding of the bonding involved. Techniques such as X-ray diffraction (XRD) and Infrared (IR) spectroscopy have been used to elucidate the structures of various bivalent, transition metal oxalates.

1.1.1.1 Structures

The free oxalate ion in aqueous solution has a D_{2d} staggered structure with an angle of 90° between the planes defined by the two $-CO_2$ groups (Figure 1.1) [40-42]. The uncomplexed oxalate anion possesses vibrational modes of the following symmetry:

$$\Gamma_{\text{vib}} = 3A_1 + B_1 + 2B_2 + 3E$$

all of these are Raman active, with the $2B_2$ and $3E$ modes being IR active. As seen in Figure 1.1, all four of the oxygen atoms have equivalent symmetry and thus only one symmetric $\nu(\text{CO})$ stretching vibration is visible in the IR spectrum of B_2 symmetry [40].

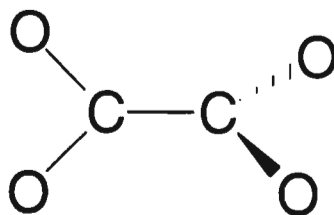


Figure 1.1: Molecular structure of the uncoordinated oxalate species, $C_2O_4^{2-}$ with D_{2d} symmetry [41]

There have been several X-ray crystallographic and IR spectroscopic studies of the transition metal oxalates, $MC_2O_4 \cdot 2H_2O$, where $M = Fe, Co$ or Ni . Clearly the local symmetry is reduced when the oxalate ion bonds to a transition metal. The exact symmetry depends on the mode of co-ordination of the oxalato group, there being three distinct possibilities. The first possibility is that the transition metal oxalate contains a mono-oxalato unit [Figure 1.2(a)].

Here the symmetry of the MC_2O_4 group is C_{2v} . In this point group, the vibrational modes become:

$$\Gamma_{\text{vib}} = 6A_1 + 2A_2 + 5B_1 + 2B_2$$

All of which are active in both the IR and Raman [43-46]. The two oxygen atoms that are coordinated to the metal atom now differ from the outer two in the oxalate moiety. There are now two pairs of $\nu(\text{CO})$ vibrations that occur, the symmetric and asymmetric vibration of the terminal $\nu(\text{C}=\text{O})$ and coordinated $\nu(\text{CO})$ groups [47, 48]. Four $\nu(\text{CO})$ bands are thus expected. When the mono-oxalato species is discrete, the $\nu(\text{C}=\text{O})$ stretching vibration is identified by a shift to higher wave numbers from the position in the free oxalate ion [45].

The second possibility is that the mono-oxalate species, MC_2O_4 , is repeated as a unit in a linear polymer chain (Figure 1.2(b)). This polymerisation is believed to lower the local symmetry to C_1 , because of distortions at the metal atom centre, and thus all vibrational bands become both IR and Raman active [43-46]. The origins of the distortions at the metal centre that leads to the lower C_1 symmetry were not discussed by the authors [43-46].

According to Edwards *et al.* [43-46], there is the third possibility of a discrete bisoxalato metal anion species of formula $M(\text{C}_2\text{O}_4)_2^{2-}$ (Figure 1.2(c)). The two oxalato groups are symmetrically coordinated, with the symmetry of this planar unit being D_{2h} . The vibrational modes in this point group have the following symmetry:

$$\Gamma_{\text{vib}} = 7A_g + 2B_{1g} + 3B_{2g} + 5B_{3g} + 3A_u + 7B_{1u} + 7B_{2u} + 4B_{3u}$$

With this symmetry, the A_g , B_{1g} , B_{2g} and B_{3g} vibrational modes are Raman active and the B_{1u} , B_{2u} and B_{3u} modes are IR active. The A_u vibrational mode is not active in either the Raman or IR spectra [45]. This means that there are seven polarised bands expected in a Raman spectrum, with no coincidences between the Raman and IR spectra as expected for a centrosymmetric complex.

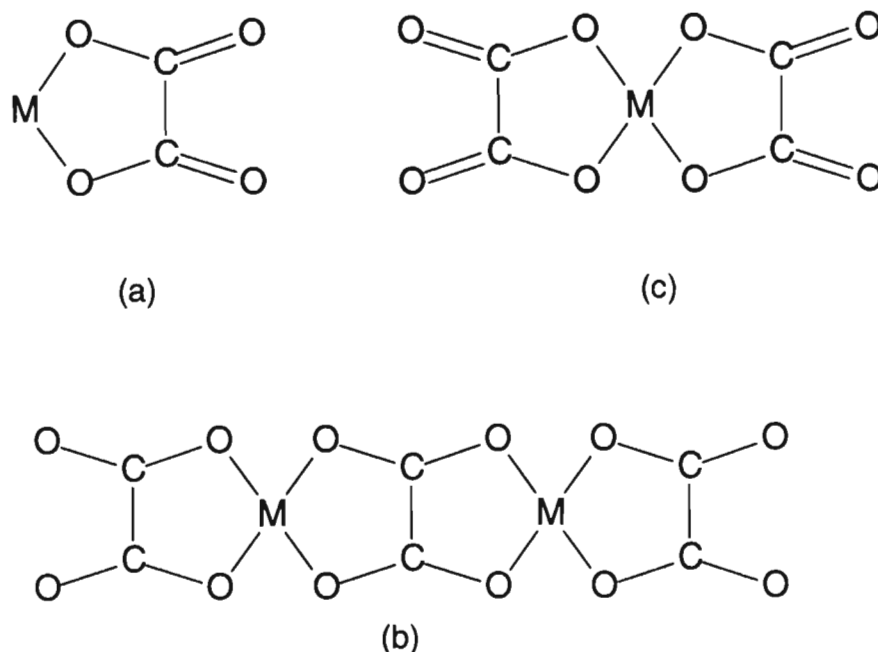


Figure 1.2: Structural units of bivalent transition metal oxalates, where $M = Fe^{2+}$, Ni^{2+} or Co^{2+} [45] a) the mono-oxalato species, (b) the bisoxalato species, (c) the polymer

The solid state structures of nickel(II) and cobalt(II) oxalates are very similar, with both compounds crystallising in the monoclinic space group of $C2/c$ (C_2^6), with four formula units per cell [49, 50]. Both are referred to as α -type crystals although there is also an orthorhombic, β form of the compounds. The XRD patterns of these two compounds are very similar, with a slight shift of peaks to higher 2θ values in the nickel(II) oxalate pattern due to the smaller size of the nickel ion [51]. Each of these transition metal oxalates exhibits the same vibrational bands in both IR and Raman spectra. According to Edwards *et al.* [43, 44], this involves forming a polymer chain, with a repeat unit of C_1 symmetry. These polymer chains form layers which are held together by the hydrogen bonds of the associated water molecules [43-46]. Such an argument is consistent with the formation of the compounds as dihydrates i.e., $MC_2O_4 \cdot 2H_2O$, where $M = Co$ or

Ni. Edwards *et al.* further suggests that the metal atoms are octahedrally coordinated with water molecules at the apices. These oxalates have been shown to be isomorphous and polymeric [52].

Iron(II) oxalate, like nickel(II) and cobalt(II) oxalates, also crystallises in a monoclinic, α -type system, with the space group $I2/c$ (the alternative setting for $C2/c$). It also has an orthorhombic, β -type crystal alternative [49]. The α -form differs quite significantly, however, from the nickel(II) and cobalt(II) analogues insofar as the XRD pattern [51] and the IR and Raman spectra [43-46] are concerned. Edwards *et al.* research has shown that there is no coincidence in the bands of the IR and Raman spectra for iron(II) oxalate. This suggests that the Mutual Exclusion Rule [53] applies, and that the local symmetry at the iron atom is centrosymmetric. The bisoxalato compound shown in Figure 1.2(b) is centrosymmetric with bidentate co-ordination, and represents the most likely structure for the iron(II) oxalate. In this configuration the iron atom adopts a position equidistant from the four co-ordinating oxygen atoms [46]. Clearly the structure of the iron(II) oxalate cannot simply involve the co-ordination of two oxalate moieties with an iron atom. Edwards and Russell [45] propose that iron(II) oxalate in the solid state is also polymeric, but with a repeat unit of local symmetry D_{2h} [Figure 1.2(b)]. Water molecules above and below the plane of the repeat unit are believed to complete the octahedral co-ordination at the iron atom, and to link, through hydrogen bonding, one plane to another.

There is clearly a difference in the structure and bonding of the iron(II) oxalate compared with that of the nickel(II) and cobalt(II) oxalates. The XRD and IR/Raman data show this, as do the behavioural differences during decomposition. Until single crystal X-ray studies are carried out on all three compounds, the exact differences are not known. Unfortunately, due to the extreme insolubility of the compounds, recrystallisation is extremely difficult, and the possibility of a single crystal of X-ray quality remote.

1.1.1.2 Dehydration

All the transition metal oxalates are hydrated and therefore go through a dehydration step before decomposition. This step, at first, seems straightforward, as it is always endothermic in nature [54]. However, the physical characteristics of the material formed in the dehydration process are affected by a number of factors that include the texture of the solid starting material and the speed at which water is lost i.e., the kinetics of the dehydration process. This is exemplified by the hydrated oxalates, in that the temperature (and hence the rate) at which dehydration takes place, plays a large role in determining the specific surface area of the resultant product. Large pores tend to develop in the oxalate as dehydration takes place, increasing the surface area of the material. The lower the temperature of dehydration, the more pronounced the porosity becomes, since the water is removed relatively slowly and can escape without much disruption to the original particles [55]. If the rate of dehydration is high, smaller non-porous particles are formed in which much of the lattice strain has been relieved [56, 57]. These hydration reactions are reversible [58]; nevertheless the anhydrous oxalate can be isolated as a stable intermediate product [56]. Some research has also been carried out on the effects of pressure as dehydration takes place. At low water vapour pressure or in a vacuum, amorphous anhydrous materials with high surface area are often produced. Higher vapour pressures of water tend to produce crystalline anhydrous products with much lower surface area. This is known as the Smith-Topley effect and has been observed for a number of oxalates and other oxysalts [59]. In the study conducted for this dissertation, the Smith-Topley effect was not observed, as the dehydration and decomposition were determined using a rising temperature program. By adding an extra parameter of rising temperature, the gas is removed as fast as it is formed and thus no measurement of water vapour pressure can be made [60, 61]. It has been found that the use of pressure change techniques for inducing and studying dehydration is quite limited [56, 57], since the water vapour remains in contact with the sample and only the initial stages of the dehydration can be followed.

For this reason researchers have favoured temperature change techniques such as thermogravimetry (TG) with differential thermogravimetric analysis to monitor the dehydration of oxalates. Application of these techniques in oxygen or in an inert atmosphere has shown that the product of decomposition is independent of the atmosphere used in the dehydration step, with the exception of ferrous oxalate for which, in air, no anhydrous product can be isolated. What is crucial, however, is the heating *rate* used. Exact heating rates will depend largely on the equipment used, the amount of material and the rate at which gas is passed over the sample [54, 62, 63]. It has been found that the thermogravimetric curves of most transition metal oxalates show no stable dehydration states when obtained at a fast heating rate. Ferrous oxalate is a particularly difficult case, where no anhydrous stage is observed if the TG heating rate is too fast. However, when the heating rate is slowed down, separation of the dehydration and decomposition stages can be obtained [63]. In a study of the dehydration of some transition metal oxalates, the enthalpies of dehydration for $\text{FeC}_2\text{O}_4 \cdot 2\text{H}_2\text{O}$, $\text{CoC}_2\text{O}_4 \cdot 2\text{H}_2\text{O}$ and $\text{NiC}_2\text{O}_4 \cdot 2\text{H}_2\text{O}$ was measured as 62.3, 57.3 and 55.2 $\text{kJmol}^{-1} \text{H}_2\text{O}$, respectively [64]. Water molecules in these compounds are reported [65] to be coordinated directly to the metal ion, and therefore the dehydration temperature and enthalpy of hydration are dependent on both the nature and size of the cation. The temperature at which dehydration takes place gives information about the dissociation energy of M-OH_2 . According to Nagase *et al.* [64] it can be supposed that since the water molecules are bonded directly to the metal ions by electrostatic forces, the bond energy is a function of the size of the metal ion. Their observation that the dehydration temperature increased with $1/r$, where r is the ionic radius of the bivalent transition metal is consistent, since the metal- H_2O bond is expected to strengthen as the ionic radius of the metal ion decreases.

1.1.1.3 Thermodynamics of Thermal Decomposition

The thermal decomposition of bivalent transition metal oxalates proceeds by several different routes. These processes result in different decomposition products, namely the metal, the metal oxide, or the metal carbonate [62]. A number of factors determine the nature of the decomposition product formed. The stability of the metal oxide, as measured by the enthalpy of formation of the oxide (ΔH_e), is one such factor. The importance of metal oxide stability can be clearly seen in Table 1, which lists the decomposition products obtained on heating the oxalates of a variety of metals along with their ΔH_e values [66]. The less stable the oxide (i.e. low $-\Delta H_e$ values) the more likely the oxalate is to decompose to the metal. Antimony and bismuth are the exceptions as they show mixed behaviour, forming a mixture of both the metal and the oxide. A possible explanation for this could be that these are metalloids and thus have fundamentally different characteristics from typical metals. Iron(II) appears also to be an exception, in that either the metal or the oxide is formed, depending on the conditions of decomposition [66]. This dual nature of iron(II) is to be expected given that the heat of formation for FeO of $-31.9 \text{ kcal mol}^{-1}$ is on the border between the heat of formations for oxides derived from oxalates which decompose to the metal and oxalates that decompose to the oxide (Table 1.1). Acheson and Galwey [67] have also noted a correlation between the activation energy for the decomposition of oxalates and the heat of formation of the appropriate oxide. Macklen [68] found that the heat of stabilities of four divalent oxalates in nitrogen diminished in the sequence of decreasing electronegativities of the cations $\text{Mn} > \text{Fe} > \text{Co} > \text{Ni}$.

This discussion of the thermal decomposition of oxalates will be restricted, mainly, to the three oxalates under study, i.e., ferrous oxalate, nickel oxalate and cobalt oxalate.

Table 1.1: Primary decomposition products of simple oxalates and the heats of formation (ΔH_e) per equivalent of corresponding metal oxide under N_2 [66].

Oxalate	$-\Delta H_e$ (kCal)	Product
Cobalt	119.7	Metal
Nickel	122.2	
Cadmium	127.2	
Tin	145.2	
Lead	69.0	
Antimony	97.9	Antimony and bismuth give a mixture
Bismuth	96.2	of metal and oxide
Silver	15.5	
Magnesium	300.8	Oxide
Aluminium	273.2	
Chromium (III)	188.3	
Manganese (II)	192.5	
Iron (III)	134.3	
Zinc	174.1	
Iron (II)	133.5	In Iron (II) oxalate the metal is also formed (depending on conditions)
Cerium (III)	303.3	Oxide and some carbon
Thorium (IV)	307.1	
Praseodymium	304.6	
Lanthanum	297.1	
Lithium	297.9	Carbonate
Sodium	207.9	
Potassium	180.7	
Calcium	334.3	
Strontium	295.4	
Barium	279.1	

Although there are differences in the bonding of the ferrous oxalate, as compared to that of nickel and cobalt oxalates, as discussed above, Mahomed and Galwey [69] concluded that the factors controlling the decomposition rate of ferrous oxalate are the same as those in the other bivalent oxalates, with the energy barrier to anion breakdown being the strength of the bond between the metal ion and the carboxyl oxygen.

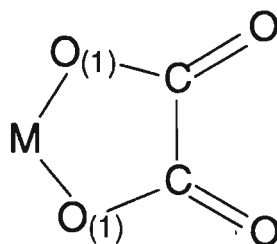


Figure 1.3: Structure of bivalent, transition metal oxalates (where M is Fe^{2+} , Ni^{2+} or Co^{2+})

After dehydration, the pyrolysis of oxalates is single-stage decomposition [70]. The route the decomposition takes, depends on the strength of the metal-oxygen bond. The extent to which the metal-oxygen bond is covalent depends on the size, charge and electronegativity of the central metal cation i.e., on its polarising power. Thus the nature of cation will determine the reaction route [54]. The more covalent the $M-O_{(1)}$ bond, the stronger it is (Figure 1.3). Thus the strength of the $M-O_{(1)}$ bond affects the decomposition route by determining the temperature at which the rupture of the $M-O_{(1)}$ bond is possible. Of particular relevance is whether the $M-O_{(1)}$ bond or the $C-O_{(1)}$ bond is broken first. Should the reaction proceed via the rupture of the $C-O_{(1)}$ bond, it will be followed by breaking of one of the $M-O$ bonds, due to the inability of the metal to accommodate two O atoms. The $C-C$ bond then breaks to give as the resulting products the metal oxide and equimolar proportions of CO and CO_2 gas [Equation (1)]. The reaction can also proceed via the direct rupture of the two $M-O$ bonds followed by the breaking of the $C-C$ bond to produce the metal and two moles of CO_2 [Equation (2)] [54, 62].



Thermodynamic arguments can now be applied, as follows, to determine which of the above two reactions will be favoured under equilibrium conditions and in an inert atmosphere i.e., whether the bivalent metal oxalate will decompose to form the metal oxide [Equation (1)] or the metal [Equation (2)].

K_1 and K_2 are the equilibrium constants for reactions 1 and 2

$$K_1 = \frac{[\text{MO}][\text{CO}][\text{CO}_2]}{[\text{MC}_2\text{O}_4]} \quad (3)$$

$$K_2 = \frac{[\text{M}][\text{CO}_2]^2}{[\text{MC}_2\text{O}_4]} \quad (4)$$

(The square brackets denote the activity.)

$$\text{Then } K_1/K_2 = \frac{[\text{MO}][\text{CO}]}{[\text{M}][\text{CO}_2]} \quad (5)$$

K_6 and K_7 are equilibrium constants for reactions 6 and 7



A similar analysis affords:

$$(K_7/K_6)^{1/2} = \frac{[\text{MO}][\text{CO}]}{[\text{CO}_2][\text{M}]} \quad (8)$$

$$\text{Thus } K_1/K_2 = (K_7/K_6)^{1/2} \quad (9)$$

If the standard free energy of formation ($\Delta G^\circ = -RT \ln K$) for reaction 6 is denoted by ΔG_6 , and for reaction 7 by ΔG_7 then for $\Delta G_6 < \Delta G_7$, there must be the relation $K_6 > K_7$. Hence by equation (9) it also follows that $K_1 < K_2$, and reaction (2) will predominate over reaction (1). This behaviour is clearly illustrated by an Ellingham diagram. As can be seen in Figure 1.4., for cobalt and nickel ΔG_7 exceeds ΔG_6 (represented by CO), and as such, reaction (2) will predominate over reaction (1), resulting in the formation of the metal powder. The ferrous ion is unique in that the $T - \Delta G_7$ plot crosses the $T - \Delta G_6$ plot at $>500^\circ\text{C}$. This means that, according to the temperature at which decomposition takes place, different products will be formed. Since the interest is in the formation of metal powders, temperatures lower than 500°C will have to be utilised. The Zn line illustrates the case in which $\Delta G_6 > \Delta G_7$. In this case reaction (7) predominates over reaction (6) and zinc oxide is the expected product of the thermal decomposition of zinc oxalate (Table 1.1).

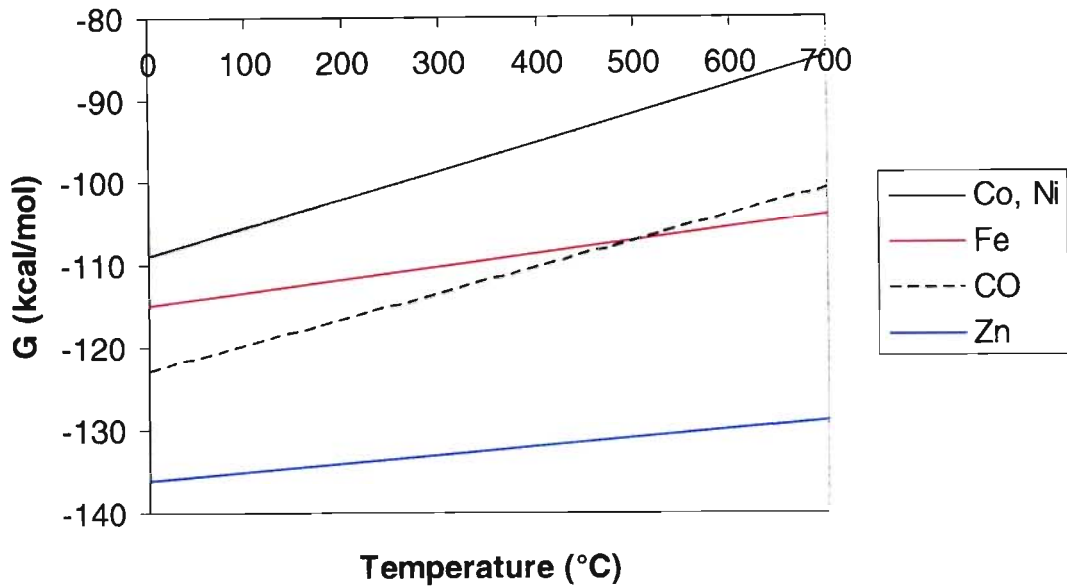


Figure 1.4: Ellingham diagram showing the relationship between ΔG_6 and ΔG_7 [71]

These arguments apply to equilibrium conditions and thus slow rates of temperature increase must be used in order to approximate equilibrium [62]. The gaseous products produced during decomposition should also be removed in the nitrogen stream to favour the production of one final solid product, either the metal or the metal oxide. If any oxygen is present, the metal powder is immediately oxidised [74].

For oxalates that produce the metal in a nitrogen atmosphere, i.e., follow the decomposition route of equation 2, the decomposition temperature represents the temperature at which the M-O link is ruptured, and thus depends critically on the size and charge of the metal ion. Kornienko [72] and Robin [73] have attempted to relate decomposition temperatures with the fundamental properties of the metal ions of bivalent transition metals. Dollimore *et al.* [62] also related the decomposition temperatures to the ionic radii of the bivalent transition metals (Figure 1.5.).

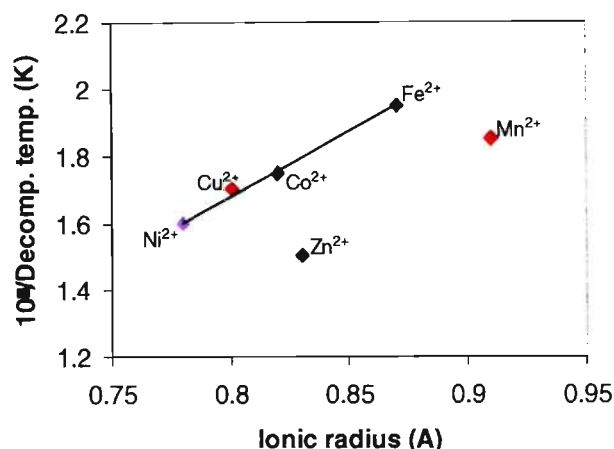
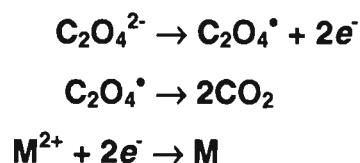


Figure 1.5: Dependence of decomposition temperature on the ionic radius of the metal for oxalates of bivalent transition metals [62]

The two bivalent transition metal oxalates, manganese and zinc, which lie off the line, give the oxide as their decomposition product in both nitrogen and air. From this plot and the thermodynamic arguments discussed previously, it appears that all three of the oxalates under investigation thermally decompose to their respective metals. This, however, does not seem to be the case. Dollimore *et al.* found that although the thermodynamic treatment of ferrous oxalates should yield the metal, the product was in fact Fe_2O_3 . A number of researchers [63, 65, 68, 69, 75-77] have found the primary decomposition product to be FeO , but that this was unstable below $573\text{ }^\circ\text{C}$ and decomposed to Fe and Fe_3O_4 . Mu and Perlmutter [80] found only Fe metal as the final thermal decomposition product. Nicholson [75] reported the behaviour of ferrous oxalate on heating to be very sensitive to the presence of traces of oxygen in the prevailing atmosphere. Clearly an inert atmosphere is essential if the metal is the desired product of the thermal decomposition of a metal oxalate [78].

1.1.1.4 Kinetics and Mechanism of Thermal Decomposition

The kinetics of the thermal decomposition of metal oxalates have been extensively studied and various mechanisms have been proposed [54]. A general observation is that, as the decomposition proceeds, the reaction rate increases. This is partly due to an increase in the surface area of the solid, but is also believed to be due to the formation of metal nuclei, in the case where the metal is the decomposition product. Jacobs and Kureishy [57] have reported an overall mechanism for the decomposition of nickel oxalate (Scheme 1.1), which can possibly be extended to all of the oxalates considered in this study [38, 54]. It involves a transfer of electrons from an oxalate ion to a metal ion, followed by the decomposition of the resultant oxalate radicals to form two moles of CO₂ [54, 56, 63]. The electron transfer step is believed to be rate determining [57].



Scheme 1.1: Proposed decomposition pathway [57]

It has also been concluded [79] that in the decomposition of manganese(II) oxalate, the initial oxidation of a small proportion of the cation, $\text{Mn}^{2+} \rightarrow \text{Mn}^{3+}$, provided the active intermediate that participated in the subsequent decomposition of the salt. There is also evidence that the decomposition of copper(II) oxalate proceeds to completion through the intervention of the copper(I) salt, $\text{Cu}_2\text{C}_2\text{O}_4$. Taken together these observations indicate that the mechanisms of decomposition of bivalent metal oxalates have in common an electron transfer step that is probably rate-determining. Mohamed and Galwey [69] have concluded that the factors controlling the decomposition rate of ferrous oxalate are the same as for other bivalent metal oxalates.

Because the decomposition of the anion occurs at the interface between the product and the oxalate, the electron transfer process may consist of several

intermediate steps in which the electrons are initially transferred to vacancies present at the interface. Another possibility is that the mechanism is one in which the interface affects the energy of positive hole formation by band bending [70], rather than by the provision of acceptor energy levels. Since the reaction follows the form of:



*(If the oxalate is hydrated, there will be intermediate stages.)

the solid product, in this case the metal, is formed in an 'activated', dispersed state, due to a large internal area and the presence of lattice strain. Referring back to equation 10, each crystallite of A decomposes as a whole giving a micelle of B composition, but in the pseudo-lattice of A. This micelle is highly strained, and thus would recrystallise into the stable, normal lattice of B. The recrystallisation would spread out from B nuclei, so that the net result would be that each crystallite of A would give rise to N micelles of B (N being greater than unity), with a corresponding increase in specific area [70, 78].

1.1.1.5 Important Control Parameters

Mu and Permuter [80] studied the effects of heating rates on the dehydration and decomposition of oxalates. According to their results, increasing the heating rate from 1°C/min to 5°C/min typically leads to an increase in the maximum dehydration and decomposition temperatures of between 20 and 40°C. The increase for NiC₂O₄ and FeC₂O₄ is even greater at between 80 and 90°C. This is clearly a reflection of the time needed for heat conduction in the solid. The rates and temperatures of heating during decomposition are thus very important, and greatly affect the surface area of the metal powders produced [39, 54, 57, 62]. At any given temperature, two competing processes contribute to surface area changes. The process increasing the surface area is generally accepted as strain resulting from the differences between the specific volumes of reactant and solid product, as has been discussed above. The process reducing surface area is that of sintering. Sintering refers to the increase in particle size and reduction in

surface area at elevated temperatures, and is thus temperature related. In its simplest form, this process represents a tendency for the system to reduce the total surface energy [81]. The mechanisms involved in sintering have been studied by Hüttig [82], and are summarised here in terms of temperature, and expressed as

$$\tau = T/T_m$$

where τ is the temperature (K) at which a substance is sintered, T is the absolute temperature of the solid, in this case a metal powder, and T_m is the melting point.

Various situations arise as follows:

1. Below $\tau = 0.23$, a process of adhesion between particles occurs with a reduction in surface area.
2. In the region $\tau = 0.2 \sim 0.36$ surface diffusion occurs leading to an initial increase in surface activity when surface area and capillaries are enlarged.
3. In the region $\tau = 0.33 \sim 0.45$ surface diffusion results in sintering.
4. In the region $\tau = 0.37 \sim 0.53$ internal lattice diffusion occurs and initially may lead to activation. In this region the last traces of occluded volatile materials are often expelled.
5. In the region $\tau = 0.45 \sim 0.80$ lattice diffusion continues with further sintering. Single crystals may be formed.
6. Above $\tau = 0.8$ a light reactivation may occur before melting.

Hüttig [82] obtained these results from observations on metals and metal oxides (particularly ceramics). In most of the systems the value $\tau = 0.5$, where the temperature of the solid is half that of the melting temperature, is so important and visible, it can be easily recognised. It is known as 'the Tamman Temperature' [83, 84], and is of significance because it is at this temperature that sintering occurs by the diffusion of species through the bulk material [81].

In this study, sintering was kept at a minimum, as the aim was to produce metal powders in a finely divided, dispersed state. Precautions were taken to stop any decrease in surface area and increase in size (refer to Chapter 2).

1.1.2 Solid Solutions of Bivalent Transition Metal Oxalates

The quest for high purity, finely-divided metal powders and metal oxides has led to the wide use of coprecipitation techniques for the preparation of mixed metal oxalates [85-87]. In the precipitation-filtration technique, the metal ions are simultaneously precipitated in the required stoichiometric proportions. In many cases a single-phase solid solution precipitates, assuring homogeneity. Even if segregation occurs during precipitation, the degree of mixing is far superior to that of conventional mixing techniques. The oxalate ion is one of the most popular precipitating agents, due to the relative ease of decomposition [88]. Bimetal oxalate solid solutions have been prepared and studied by Wickham [89] and Robin [73], from the mid 1950's. Schuele successfully prepared Co-Fe, Ni-Fe, Zn-Fe, Mg-Fe and Mn-Fe oxalate solid solutions, but failed with the Cu-Fe system [90]. He concluded that ions with nearly the same radii could form solid solutions with each other. Recently solid solutions of Ni-Co oxalate have been prepared [38, 91]. Due to the similarity in both charge and solid state ionic radii of nickel and cobalt ions, there is a complete range of solid solution and very little change in lattice composition as both nickel oxalate dihydrate and cobalt oxalate dihydrate form α -type crystals [92]. Donia *et al.* [93] also prepared and identified the solid solution of Co-Cu oxalate. In this solid solution, the two metals have somewhat different ionic radii, and as such have a limited range of solution. High cobalt content leads to the solid solution, as it has the larger ionic radius. Ternary solid solutions are also of interest, and the ternary oxalate of Ni-Fe-Zn has been prepared by similar methods by Fischer *et al.* [94] in order to form ferrites of spinel structure.

As with the single oxalates, these solid solutions can be decomposed thermally at moderately low temperatures to form alloys or mixtures of the metal oxides. They can therefore be used as an intermediate product containing metal ions in the required stoichiometric ratio [38]. The decomposition of coprecipitated oxalates is similar to that of the single oxalates [38, 91, 93]. The temperatures of decomposition however differ from those of the parent oxalates. There is also a marked difference in the thermal decomposition of mixed oxalates as opposed to coprecipitated oxalates [38, 91, 93]. The coprecipitated solid solutions behave as

a single compound, and form final products more readily than physical mixtures [91]. In thermogravimetric studies the coprecipitated oxalates show single symmetrical weight losses for dehydration and decomposition, and the mixtures are expected to have poorly resolved weight losses for dehydration, and well resolved individual weight losses for anhydrous oxalate decomposition [91].

The resultant metal powders of the thermally decomposed coprecipitated oxalates are alloys. Schuele [90] formed alloys with cobalt-iron systems and nickel-iron systems when thermally decomposing the corresponding binary oxalates in the reducing atmosphere of hydrogen.

In the present study the ternary solid solutions of Co–Ni–Fe are prepared and investigated. The radii of the three metals are very similar, and thus a full range of solutions is expected. [$r(\text{Fe}^{2+}) = 0.76 \text{ \AA}$; $r(\text{Co}^{2+}) = 0.74 \text{ \AA}$; $r(\text{Ni}^{2+}) = 0.72 \text{ \AA}$] [95].

1.2 THERMAL DECOMPOSITION OF METAL CARBONYLS

The thermal decomposition of mononuclear carbonyls has become an industrially important method for purifying certain transition metals. In the Mond process, crude nickel is refined to very pure nickel using a carbonyl method. Crude nickel and CO react at 100°C to form $\text{Ni}(\text{CO})_4$, which on further heating to ca 200-300°C, decomposes to Ni and CO. If the $\text{Ni}(\text{CO})_4$ is formed under high pressure, the vapour is condensed to a liquid, purified, vaporised, then rapidly heated to 300°C. The result is the formation of fine, high purity nickel powder of particle size less than 10 μm . This is a highly selective process, as under operating conditions of relatively low temperatures and pressures, the carbonyls of other elements present, such as iron and cobalt, are not readily formed. The Mond process has been modified to purify iron, with higher pressures being needed for the reaction of CO with iron to form $\text{Fe}(\text{CO})_5$. The reason the Mond process works so well with these two elements is that nickel and iron are the only two transition metals that react directly with CO to form carbonyls.

Of interest in this work is the thermal decomposition of homoleptic transition metal cluster carbonyls, in order to obtain finely divided metal powders. These are compounds containing three or more metal atoms held together, mainly, by metal-metal bonds, and to which CO is bonded. Carbon monoxide, CO, is the most important π -acceptor ligand, and forms a host of neutral, anionic and cationic transition-metal complexes. There is at least one known type of carbonyl derivative for every transition metal [96]. A general formulation would be $M_x(\text{CO})_y$, where M is a metal in the zero oxidation state and x and y are integers. The bonding and structures of these molecules will first be described following which the limited data available on their thermal decomposition will be reviewed.

1.2.1 Structure and Bonding in Binary Metal Cluster Carbonyls

Cluster complexes containing several metal atoms held together, mainly, by metal-metal bonding have received increasing attention because of (i) interest in the rules governing their stoichiometry and structure, and (ii) possibilities for their use in homogeneous and heterogeneous catalysis [97]. The Sidgwick concept of effective atomic number or 18-electron rule has been very useful in predicting the formulae of these compounds [98]; this is briefly reviewed in the next section. Also, it should be noted that molecular orbital and ligand field calculations have provided more insight into detailed features of bonding in the metal carbonyls.

1.2.1.1 Bonding

The 18-electron rule requires each metal atom to interact with a sufficient number of CO molecules and additionally, in polynuclear complexes, with sufficient neighbouring metal atoms, to allow the metal to achieve the electronic structure of the subsequent inert gas in the periodic table. Each CO is counted as supplying a pair of electrons either in a terminal (T) or bridging (B) position (Figure 1.6).

Neighbouring metal atoms contribute one electron through a metal-metal bond of bond order one. In some special cases, bridging carbonyls interacting both through the carbon as well as the oxygen of the CO group (μ,η^2 -CO) contribute

four electrons [99, 100], but these types of compounds will not be discussed in this brief review. The possible bonding modes for CO in metal cluster carbonyls are summarised in Figure 1.6.

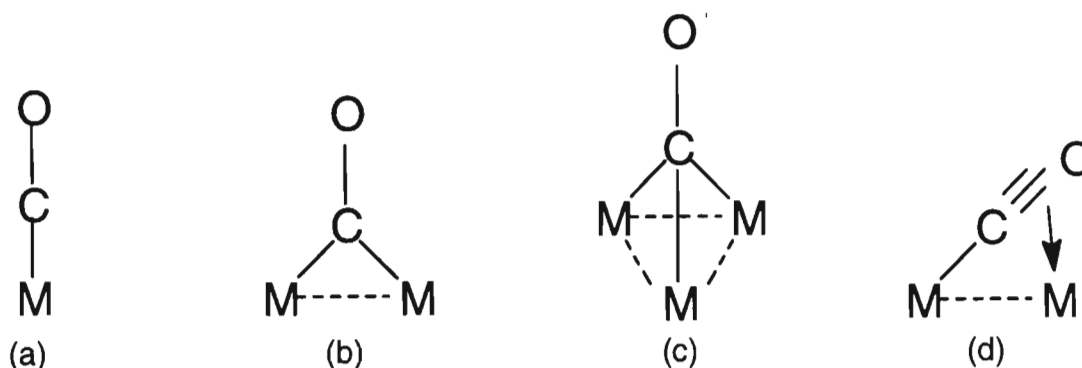


Figure 1.6: Bonding modes of CO: (a) terminal (T), (b) doubly bridged (B), (c) triply bridged (B), and (d) the (μ, η^2) -CO entity

An example of a cluster compound which obeys the 18-electron rule is $\text{Ir}_4(\text{CO})_{12}$. Iridium metal atom has nine valence electrons and coordinates to three CO molecules which leaves the electron count per metal atom at only 15; thus coordination to three other iridium atoms satisfies the 18 electron count. Overall the electron count is 60, and there are six covalent metal-metal bonds. Many metals containing an odd number of electrons achieve the inert gas configuration by forming a covalent metal-metal bond or by the CO molecules acting as bridges between two metals where each metal receives one electron from each CO molecule. In some complexes, a CO molecule forms a bridge between three metal centres. In these cases, the CO is still counted as a two-electron donor (Figure 1.6(c)). Nearly every metal forming a carbonyl obeys the 18-electron rule, although as clusters of greater than six central metal atoms are reached, it becomes unwieldy and misleading. Wade's rules [101] take over as a more accurate way of predicting stoichiometry. For the purposes of this investigation the 18-electron rule will serve.

Bond lengths and infrared spectra support the multiple-bond character of the M-CO bonds. Co-ordination of a CO molecule to a metal centre can change the C-O bond order. According to the description of σ - and π -bonding, increased σ -

bonding between a metal and CO results in a decreased bond order for the C-O bond. Increased π -bonding results in more electron density occupying the π^* orbitals of CO and hence a decrease in the C-O bond order. Changes in the bond order of C-O are reflected in the shifts of the C-O stretching frequencies in the infrared spectrum of a particular metal carbonyl. As the bond order increases, the C-O stretching frequencies shift to higher energies. Compared to the stretching frequencies of free CO (2143 cm^{-1}), terminal carbonyl groups in neutral metal complexes have stretching frequencies in the range of $2125\text{-}1900\text{ cm}^{-1}$, showing a reduction in the bond order on coordination. By changing the electron density on the central metal and noting the change in the C-O stretching frequencies, a qualitative assessment of π -back bonding can be made. Assuming the σ bond remains fairly constant [101, 102], any change in the electron density should result in the increase or decrease in electron density flowing through the σ - π -bonding orbitals. As the negative charge on the central metal atom is increased, the π^* orbitals of CO must accept more electron density, and hence the C-O bond order should decrease [103].

1.2.1.2 Structures

A great number of complexes with nuclearity of three and higher have been discovered since the early 1970s. Many of these contain two or more different metals, other ligands in addition to CO, and have heteroatoms such as hydrogen, carbon, sulphur or phosphorus associated with the cluster [104]. Cluster compounds of nuclearity up to five or six may be termed "electron precise" [105]; that is, the lines of connectivity between metal atoms represent localised two-centre two-electron bonds. In higher nuclearity cluster complexes, bonding electrons are delocalized over several metal centres, and suitable delocalized bonding schemes are required to describe the bonding network [105]. The present study focuses on the homonuclear polynuclear carbonyls, $\text{Fe}_3(\text{CO})_{12}$ and $\text{Co}_4(\text{CO})_{12}$.

Structure of $\text{Fe}_3(\text{CO})_{12}$

For trinuclear cluster complexes, open (chain) or closed (cyclic) structures are possible. The nature of the cluster formed depends for the most part on the number of valence electrons; 50 in the first and 48 in the latter. The determination of the $\text{Fe}_3(\text{CO})_{12}$ structure proved to be difficult and in fact remained in doubt for several years. This was due to molecular disorder in the crystal that complicated the interpretation of the X-ray diffraction pattern. An early report on the crystal structure claimed the molecule was a monoclinic prism and established the molecular formula [106]. The structure was then shown to be a triangular array of iron atoms with two bridging and ten terminal CO molecules (Figure 1.7). This accepted structure was initially deduced from an X-ray crystal structure of the $\text{Fe}_3(\text{CO})_{11}\text{H}^-$ analogue [107] after a reasonable model for the disorder was devised [108]. A later re-determination of the crystal structure, provided reasonably precise bond distance and angle data [109].

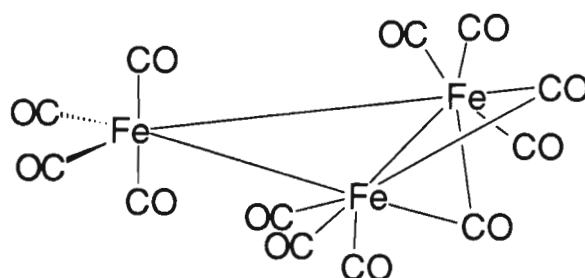


Figure 1.7: Structure of $\text{Fe}_3(\text{CO})_{12}$

The currently accepted structure is that there is a triangle of Fe atoms, the molecule as a whole possessing approximate C_{2v} symmetry. Two of the sides consist of Fe-Fe bonds unsupported by CO bridges, while the third Fe-Fe bond is bridged by two CO ligands. These CO bridges appear to be asymmetric, thus lowering the symmetry to C_2 . There has been an observed fluxionality of the compound, even in the solid state. The mechanism of this fluxionality has been described as the rotation of the iron triangle within the fixed carbonyl shell [110-113]. Originally, motion about the pseudo three-fold axis of the Fe_3 triangle was proposed, but motion about the two-fold axes of the compound may fit the data

better. The ^{13}C - ^{57}Fe couplings are consistent with this motion of the iron triangle [114]. Unfortunately, crystallographic disorder and crystal twinning [115] complicate analysis of this motion.

Structure of $\text{Co}_4(\text{CO})_{12}$

Tetracobalt dodecacarbonyl is the other compound under observation and, as with the triiron dodecacarbonyl, a brief review of the structure is given. There are three types of structure observed for tetranuclear cluster complexes: tetrahedral, open tetrahedral (butterfly) or square planar, with typical total valence electron counts of 60, 62 and 64, respectively. The earliest tetracobalt cluster complexes found were $\text{Co}_4(\text{CO})_{12}$ and the rhodium and iridium analogues. The 60-valence electron tetranuclear complex $\text{Co}_4(\text{CO})_{12}$, contains a tetrahedral array of cobalt atoms and three bridging and nine terminal CO ligands (Figure 1.8.). The structure in solution, however, is reported to have four bridging CO ligands [116]. The rhodium analogue is isomorphous to the tetracobalt species.

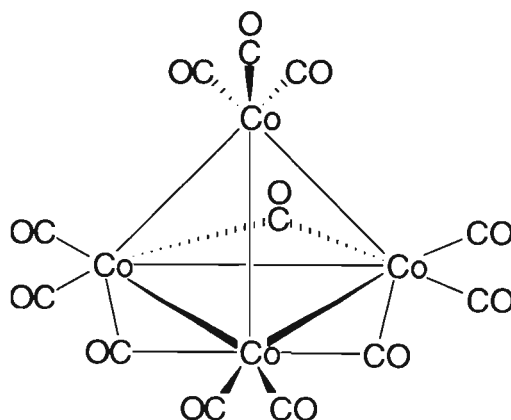


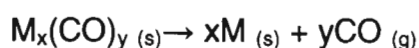
Figure 1.8: Structure of $\text{Co}_4(\text{CO})_{12}$

The tetracobalt dodecacarbonyl also has a solid state dynamic behaviour similar to that of the triiron dodecacarbonyl [117]. The crystallographic disorder deduced from the diffraction data is consistent with the movement of the central metal core.

1.2.2 Thermal decomposition of Homonuclear Metal Cluster Carbonyls

Although metal clusters (without ligands), sufficiently small enough to be distinguished from metals, are of great theoretical interest, experimental studies of "naked" metal atoms, or "naked" clusters have been limited, since even at low temperatures they form larger aggregates [118], rendering them unsuitable for most catalysis purposes. Thus there have been extensive studies carried out on the thermal decomposition of supported homonuclear and heteronuclear metal cluster compounds [119-131]. This is because by dispersing the metal atoms in a low temperature matrix or by immobilising them on a support the aggregation can be kept to a minimum. The fact that there is interaction between the substrate of the support and the cluster carbonyl, rules out any equivalence with the corresponding unsupported cluster carbonyls.

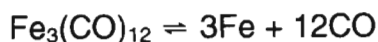
This study is concerned with the thermal decomposition of *unsupported* triiron dodecacarbonyl and tetracobalt dodecacarbonyl. In terms of the expected thermal decomposition products for both binary cluster compounds, it was hoped that the metal and carbon monoxide would be formed:



The thermodynamic driving force for this decomposition route is clearly the intrinsic stability of the carbon monoxide molecule. This reaction is also favoured on entropy grounds. However, as our, and other investigations show, the decomposition does not follow the anticipated route.

1.2.2.1 Thermal Decomposition of Unsupported $Fe_3(CO)_{12}$

According to magnetic susceptibility studies of $Fe_3(CO)_{12}$ by Cutforth and Selwood [132], one reaction product of the thermal decomposition of $Fe_3(CO)_{12}$ is finely divided iron, which results in long-stored samples becoming pyrophoric. Magnetic susceptibility measurements estimate that 3×10^{-3} percent iron impurity is formed after 80 days at room temperature. The simple reversible decomposition



was excluded by Cutforth and Selwood [132], as their sample was sealed in an evacuated tube connected to a mercury manometer, and showed no carbon monoxide evolution. They proposed instead the following decomposition reaction

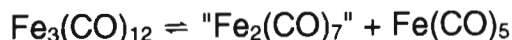


although the ennearcarbonyl, $\text{Fe}_2(\text{CO})_9$, might be involved instead of, or in addition to, the pentacarbonyl. Cutforth and Selwood did not, however, take the study further in order to prove their postulate.

Fillman and Tang [133] studied the thermal decomposition of a number of binary metal carbonyls by thermogravimetry-mass spectrometry. Their finding, with regard to the thermal decomposition of triiron dodecacarbonyl, was a single step decomposition centred at 150°C at a ramp rate of 10°C/min under an argon atmosphere. The mass-spectrometry data also showed the major evolution of CO gas in a single peak. Fillman and Tang's result [133] ruled out metallic iron as the final product as the final weight loss was less than expected theoretically for decomposition to metal. An alternative explanation of iron carbide or iron oxide formation arising from dissociation of the CO molecule was suggested as more likely [133].

This result differed from that of Eady *et al.* [134], who have found that the pyrolysis (90-114°C) of $\text{Fe}_3(\text{CO})_{12}$ in sealed evacuated tubes led to the formation of $\text{Fe}(\text{CO})_5$ and metallic iron. It was suggested that the initial degradation takes place via the ejection of a saturated (18-electron) metal fragment *viz.* $\text{Fe}(\text{CO})_5$, based on the detection of the iron pentacarbonyl in gas phase studies for $\text{Fe}_3(\text{CO})_{12}$ and disproportionation reactions to form mixed metal clusters [135]. The arrangement of carbonyl groups around two of the Fe atoms in $\text{Fe}_3(\text{CO})_{12}$ (each with 3 terminal

and 2 bridging CO groups = 5CO's), renders $\text{Fe}_3(\text{CO})_{12}$ ideally suitable for the degradation pathway of:



A rupture of the iron triangle is necessary for the ejection of $\text{Fe}(\text{CO})_5$. Since $\text{Fe}_3(\text{CO})_{12}$ has weaker metal-metal bonds than metal-carbonyl bonds, this initial step in the thermal decomposition of $\text{Fe}_3(\text{CO})_{12}$, is strongly favoured [136].

1.2.2.2 Thermal Decomposition of Unsupported $\text{Co}_4(\text{CO})_{12}$

Labroue *et al.* [137] elucidated the kinetic parameters for the thermal decomposition of unsupported $\text{Co}_4(\text{CO})_{12}$ in a hydrogen atmosphere. They found that the mass of the sample was as important a parameter as the heating rate in the decomposition reaction. Their report shows that $\text{Co}_4(\text{CO})_{12}$ exhibits a multifeature CO evolution profile [133] consistent with the formation of either $\text{Co}_4(\text{CO})_8$ or the dimer $\text{Co}_2(\text{CO})_4$ as an intermediate, after sequential losses of CO. According to Fillman and Tang [133] the dicobalt intermediate subsequently decomposes completely to metallic cobalt at about 183°C.

In a later study, Labroue *et al.* [138] could find no evidence for the $\text{Co}_4(\text{CO})_8$ intermediate. This study showed that the decomposition took place in two stages. First the carbonyl ligands were removed as CO, with no reaction with the hydrogen gas under which the experiment was conducted. Second, there was the successive stepwise formation of the hydrocarbon species, CH_4 . When they repeated the experiment under a helium atmosphere, CO_2 was detected, indicating carbon formation by CO disproportionation. However, Labroue *et al.* [138] found that when decarbonylation was over, metallic cobalt was deposited on the wall of the glass reaction vessel as a mirror.

1.3 AIMS OF THIS WORK

The overall aim of this study was to produce and characterise pure, finely divided metal and alloy powders via the thermal decomposition of (i) single, binary and ternary oxalates of iron, cobalt and nickel, as well as their solid solutions, and (ii) the metal cluster carbonyls, $\text{Fe}_3(\text{CO})_{12}$ and $\text{Co}_4(\text{CO})_{12}$.

As discussed above, metal powders are the expected products of the thermal decomposition of the oxalates of Fe^{2+} , Co^{2+} and Ni^{2+} . In these cases it is also important to establish the physical and mechanical properties of the powders with regard to purity and particle size.

Since little is known regarding the thermal decomposition of cluster carbonyls, the study of the decomposition of $\text{Fe}_3(\text{CO})_{12}$ and $\text{Co}_4(\text{CO})_{12}$ must be regarded as preliminary. The primary aim was simply to establish the nature of the decomposition products and hence the feasibility of the metal carbonyl cluster route for the preparation of metal powders.

The crystalline cluster carbonyl compounds have a much lower melting point than the oxalates, and thus much lower temperatures are required for their decomposition. In fact, $\text{Fe}_3(\text{CO})_{12}$ can be purified by sublimation under slightly reduced pressures. In other respects, however, it was envisaged that the procedures used for their decomposition could be the same as for the oxalates in order to compare the two groups of compounds.

INVESTIGATION OF METAL OXALATES

2. INTRODUCTION

This chapter explores the synthesis and thermal decomposition of a few selected bivalent transition metal oxalates. The oxalates under study are those of iron(II) oxalate dihydrate, cobalt oxalate dihydrate and nickel oxalate dihydrate (Section 2.1.), as well as their binary (Section 2.2.) and ternary (Section 2.3.) coprecipitates and mixtures.

As discussed in Section 1.2, the products of the thermal decomposition of oxalates can be the oxide or the metal depending on the atmosphere used during the decomposition. In this study, the thermal decomposition was carried out under an atmosphere of nitrogen to encourage the production of metal and alloy powders.

2.1 SYNTHESIS AND CHARACTERIZATION OF SINGLE OXALATES

The oxalates of iron, cobalt and nickel have been studied extensively by the numerous researchers [37-65]. Since results have varied between the different groups, especially with regard to ferrous oxalate, some of the earlier work has been repeated in order to understand the subject before going on to the more complex binary and ternary solid solutions.

All three of the oxalates studied were commercially available from Aldrich and Strem Chemicals in a pure form, but in order to gain experience in the preparation of bivalent metal oxalates the single oxalates of iron(II), cobalt(II) and nickel(II) were prepared (Chapter 4) and characterized by means of carbon and hydrogen (C and H) microanalysis, infrared (IR) spectroscopy, Malvern particle size analysis, scanning electron microscopy (SEM) and X-ray powder diffraction (XRD).

2.1.1 C and H Microanalysis

The microanalytical data for %C and %H (Table 2.1) are in good agreement with those calculated for the single oxalates. All experimental and theoretical values agree within 3%. The number of molecules of waters of crystallisation was also confirmed by the weight loss incurred on heating the sample, as determined by thermogravimetry.

Table 2.1: Elemental analysis of Single Oxalates

Compound	C (%)	H (%)
FeC ₂ O ₄ .2H ₂ O	13.38 (13.34)	2.20 (2.24)
CoC ₂ O ₄ .2H ₂ O	13.12 (13.13)	2.18 (2.20)
NiC ₂ O ₄ .2H ₂ O	12.94 (13.15)	2.16 (2.21)

The figures in parentheses are the calculated, theoretical values.

2.1.2 IR Analysis

Vibrational assignments were made by comparing to the published values [40, 43-47]. The IR spectra and the assignments of the absorption bands are summarised in Table 2.2. The results obtained were similar to Donia's results for Ag₂M(C₂O₄)₂ compounds, where M is Co, Ni, Cu or Zn [85]. The overall patterns of the IR spectra were similar, indicating that the oxalate group coordinates to the metal ions under study in a similar fashion.

The results obtained for the ferrous oxalate were very similar to those published and interpreted by Edwards *et al.* [45]. The present work found two new features at 3339 and 3166 cm⁻¹, in the region where Edwards *et al.* report only one peak at 3349 cm⁻¹. This is possibly due to the improved resolution of the instrument used, although they report an extra stretching frequency at 1383 cm⁻¹, assigned to $\nu(\text{C-O})$, not observed in this study.

Table 2.2: Infrared spectra and vibrational assignments for iron(II), cobalt(II) and nickel(II) oxalate dihydrate in the solid state

Vibrational Assignment	FeOx (cm ⁻¹)	CoOx (cm ⁻¹)	NiOx (cm ⁻¹)
$\nu_{as}(\text{OH}_2)$	3339 br/s	3362 br/s	3379 br/s
$\nu_{sym}(\text{OH}_2)$	3166 m/sh	3154 m/sh	3166 m/sh
$\nu_{as}(\text{C}=\text{O})$	1622 s	1619 s	1624 s
$\nu_{sym}(\text{C}-\text{O}) + \nu(\text{C}-\text{C})$	1361 m	1360 m	1360 m
$\nu_{sym}(\text{C}-\text{O}) + \delta(\text{O}-\text{C}=\text{O})$	1316 m	1316 m	1316 m
$\nu(\text{O}-\text{M}-\text{O})$	822 m	825 m	830 m
$\delta(\text{O}-\text{C}=\text{O}) + \nu(\text{M}-\text{O})$	765 m	746 m	755 m
$\nu(\text{O}-\text{M}-\text{O})$	722 m	607 m	627 m
$\nu(\text{M}-\text{O}) + \nu(\text{C}-\text{C})$	493 m	493 m	489 m

*br (broad); sh (shoulder); s (strong); m (medium); w (weak)

There are larger discrepancies between this study and that of Edwards *et al.* for the cobalt and nickel oxalates [43, 44]. Edwards *et al.* observed features at 1967, 1920, 1383, 1058 and 790 cm⁻¹ for the cobalt oxalate dihydrate not observed in this study. For nickel oxalate dihydrate the same authors report features at 1660, 1560, 1475, 1445, 915 and 545 cm⁻¹, whereas the results of the present study showed stretching frequencies at 745 and 627 cm⁻¹. There are two types of both cobalt and nickel oxalates, an α and a β form; this study is concerned exclusively with the α -type. It is not stated whether Edwards *et al.* worked with the β -type, or a mixture of the two, and this could be a reason for these discrepancies observed.

The bands due to coordinated water are observed as a strong feature in the infrared spectra of all three of the oxalates studied. These bands were found at 3339 and 3166 cm⁻¹ for ferrous oxalate dihydrate, 3362 and 3154 cm⁻¹ for cobalt oxalate dihydrate and 3379 and 3166 cm⁻¹ for nickel oxalate dihydrate for the $\nu(\text{OH}_2)$ modes. There are slight differences in the values of the ferrous oxalate

dihydrate $\nu(\text{O-M-O})$ stretching frequency compared to that of the cobalt and nickel oxalates. It has been discussed that there are differences in bonding of the ferrous oxalate compared to that of the cobalt and nickel oxalates (Section 1.1.1), the differences seen in the IR spectra are too slight to determine their cause. The XRD data give a much clearer picture (Section 2.1.1, XRD).

2.1.3 Particle Size Analysis and Scanning Electron Microscopy (SEM)

The mean particle sizes of the single bivalent transition metals were measured using a Malvern particle size analyser (Chapter 4). The results of this particle size analysis show that the largest mean particle size was that of the nickel oxalate at $26.15\ \mu\text{m}$, followed by ferrous oxalate at $13.15\ \mu\text{m}$, with cobalt oxalate the smallest at $10.18\ \mu\text{m}$. These values can vary with different methods of preparation (Section 2.4). The data were obtained when the sample is prepared by reaction of oxalic acid with the relevant sulfate salts under the conditions specified in Section 4.2.

A comparison between these results and those obtained from the scanning electron microscope (Figure 2.1), shows that they differ quite markedly. The different techniques of SEM and Malvern particle size analysis give results on different aspects of the compounds.

The photographs of the single oxalates are shown in Figure 2.1. Ferrous oxalate [Figure 2.1.(a)], exhibits block like crystals of about $20\ \mu\text{m}$ in length and $10\ \mu\text{m}$ in width. Cobalt oxalate [Figure 2.1.(b)], is comprised of rod-like particles about $20\text{--}30\ \mu\text{m}$ in length and $2\ \mu\text{m}$ in width, while nickel oxalate dihydrate [Figure 2.1.(c)], showed rounded particles with a radius of about $2.5\ \mu\text{m}$; these seemed to form in aggregates of about $30\ \mu\text{m}$ in diameter.

One of the most interesting aspects of industrially important powders is their morphology. Size and shape affect the way powders flow and pack. Of the powders under study, the least favoured morphology is that of the cobalt oxalate. These long needles would make packing and mixing extremely difficult as the needles give a larger volume/mass ratio (Section 2.4.).

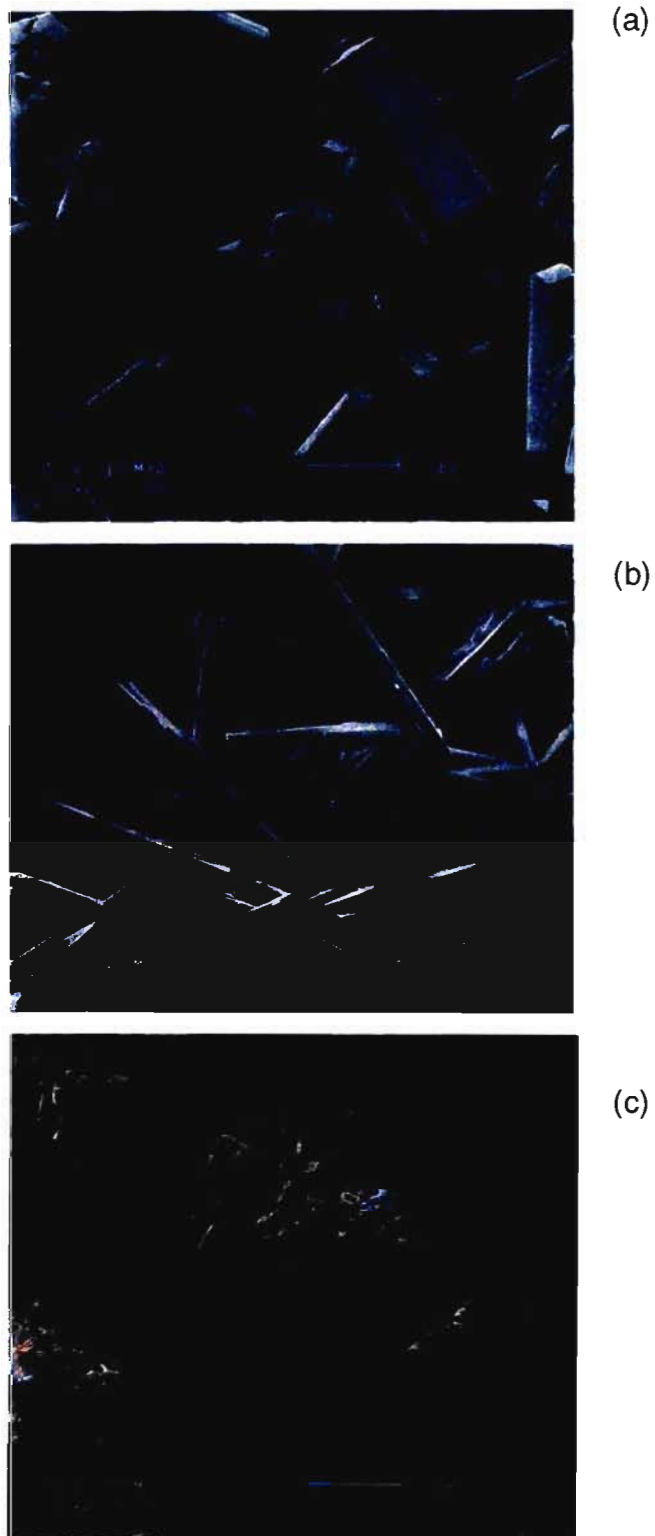


Figure 2.1: SEM photographs of the Single Oxalate Dihydrates.
(a) Ferrous, (b) Cobalt and (c) Nickel

The most favourable morphology is that of the nickel oxalate, whose spherical particles are small, giving an overall larger surface area, and are good for both packing and mixing. The blocks of the ferrous oxalate, although not as desirable as the small spherical particles of nickel oxalate, also pack well.

2.1.4 X-Ray Powder Diffraction (XRD)

The XRD patterns of the single oxalates are shown in Figure 2.2. Ferrous oxalate dihydrate exhibited a pattern typical for a primitive monoclinic crystal, which Deyrieux and Peneloux [138] designated the α -form. The cobalt and nickel oxalates were also designated the α -form, but exhibit a pattern of a centred monoclinic crystal. It is apparent when looking at the XRD patterns that the cobalt and nickel oxalates are isomorphous (as discussed in Section 1.1.1), whereas the structure of the ferrous oxalate is quite different.

There is an expected shift towards lower d-values in the pattern for the nickel oxalate as compared to that of the cobalt oxalate and, indeed this is quite evident in the XRD patterns shown in Figure 2.2 and the principal d-values shown in Table 2.3. This is because nickel has a smaller radius of 0.72 Å, than cobalt at 0.74 Å.

Table 2.3: Principal d-values (Å) for single oxalates of cobalt and nickel

CoC ₂ O ₄ .2H ₂ O (r=0.74Å)	4.718	3.901	2.965	2.563	2.101	1.918	1.879
NiC ₂ O ₄ .2H ₂ O (r=0.72Å)	4.693	3.904	2.937	2.517	2.060	1.901	1.862

2.2 PYROLYSIS STUDIES OF SINGLE OXALATES

Once the single oxalates had been synthesized and characterized, the next step was to thermally decompose them. To this end they were first studied by thermogravimetric analysis (TGA) in order to establish temperatures of dehydration and decomposition, and to gain an understanding of the products formed. Pyrolysis on a larger scale was then attempted in a tube furnace.

2.2.1 Thermogravimetric Analysis

The TGA curves in the range from room temperature to 500°C in a flowing nitrogen atmosphere, of ferrous, cobalt and nickel oxalates, are given in Figure 2.3. The thermal data obtained are summarized in Table 2.4.

The TG curves of all three oxalates show that decomposition takes place in two stages, as indicated by previous work [62,63, 67, 68, 72-78, 80]. The first step corresponds to the dehydration of the compounds and the weight loss for this step corresponded to the loss of two water molecules. This agrees with the microanalysis data and the proposed formulae of the oxalate compounds of $MC_2O_4 \cdot 2H_2O$, where M is Fe, Co or Ni.

Table 2.4: Temperatures of dehydration and decomposition, and corresponding weight losses for ferrous, cobalt and nickel oxalates under N_2

Oxalate	Dehydr. (°C)	% Weight Loss	Decomp. (°C)	% Weight Loss
$FeC_2O_4 \cdot 2H_2O$	170	19.95 (20.03)*	330	59.71 (60.07)
$CoC_2O_4 \cdot 2H_2O$	175	19.62 (19.72)	355	67.85 (67.79)
$NiC_2O_4 \cdot 2H_2O$	180	19.50 (19.69)	300	67.79 (67.88)

*Figures in parenthesis are the calculated theoretical values.

The total weight loss for the cobalt and nickel oxalates corresponded to the formation of their respective metals. This result was expected as it is in line with the thermodynamic argument put forward originally by Robin [73], and discussed in Thermodynamics of Thermal Decomposition (Section 1.1.1). The weight loss for the ferrous oxalate corresponded to the formation of FeO, and is consistent with the results of Broadbent *et al.* [63], Nagase *et al.* [64], Macklen [68, 76], Galwey [69], and Nicholson [75].

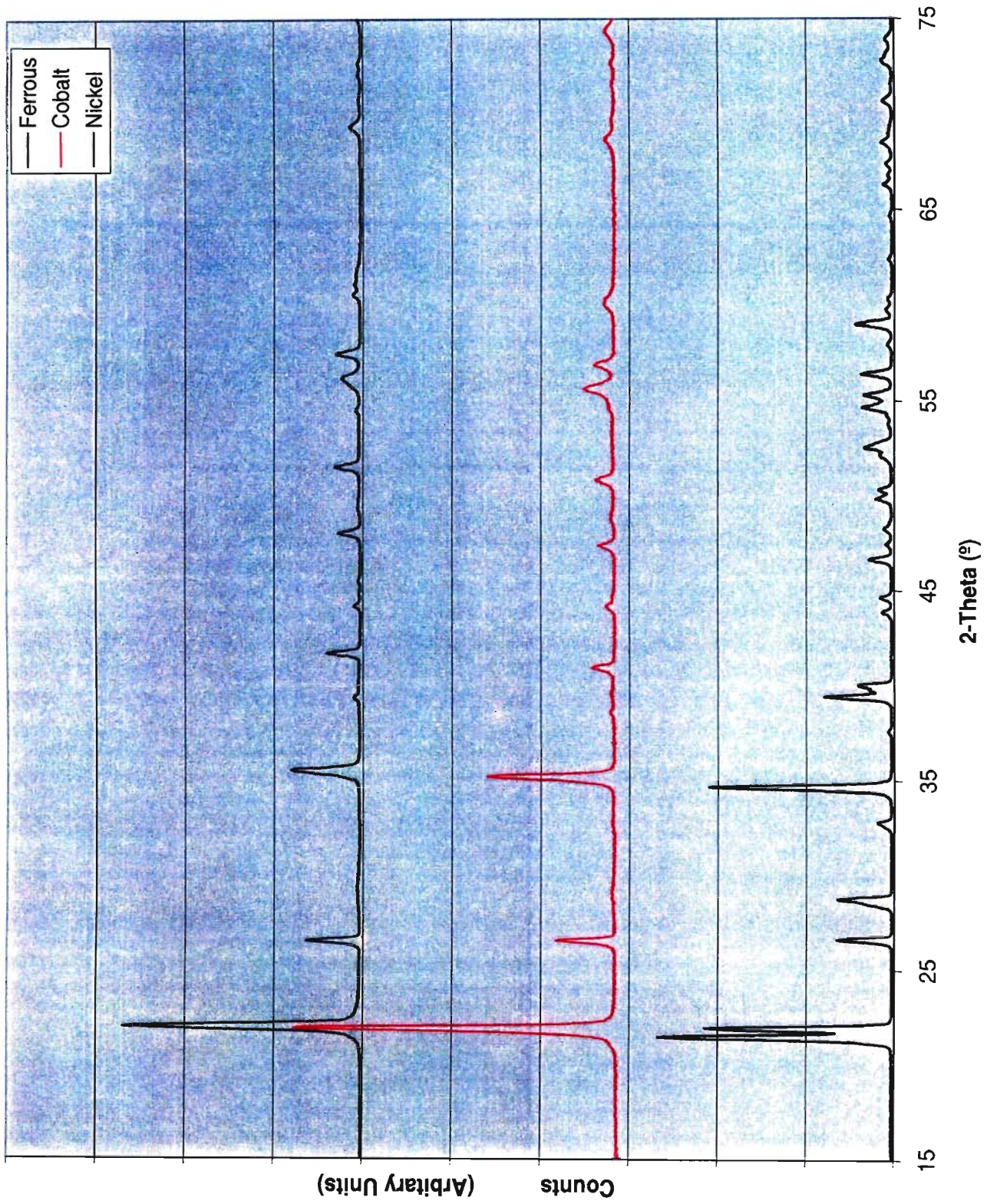


Figure 2.2 : XRD Comparison of Single Oxalates

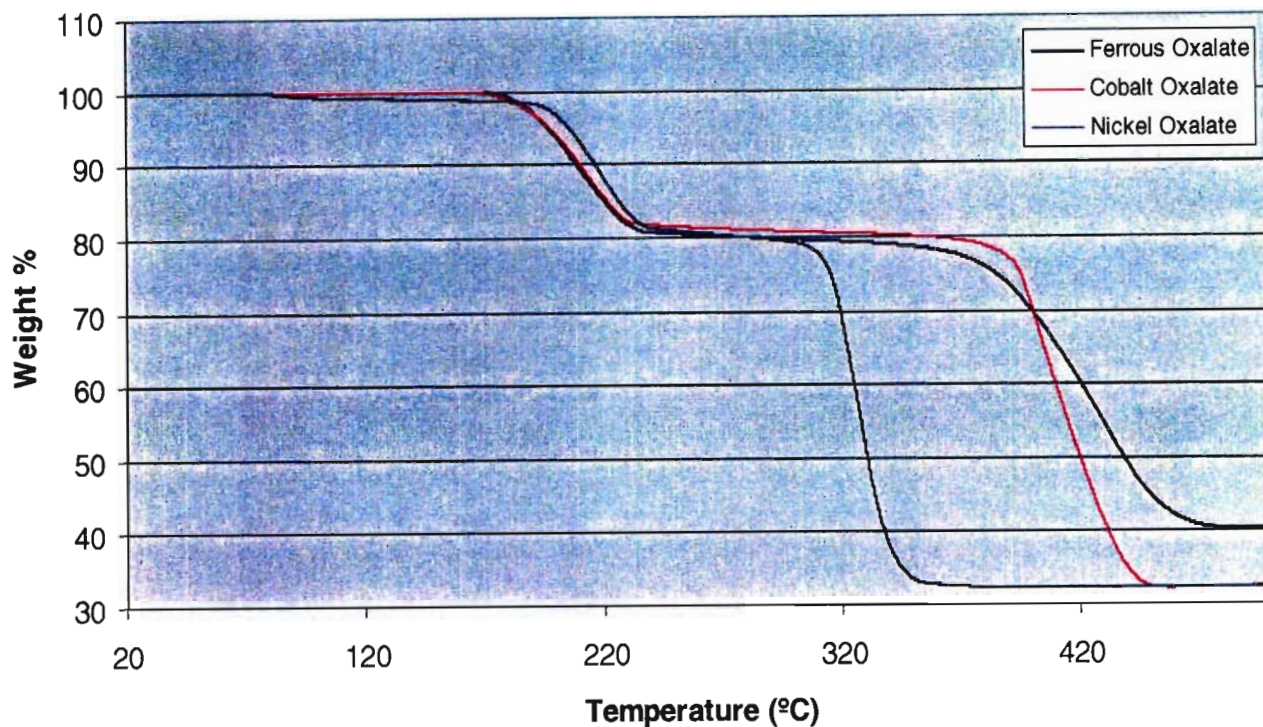


Figure 2.3: TGA of ferrous, cobalt and nickel oxalate dihydrate under an N_2 atmosphere at a ramp rate of 5°C per minute.

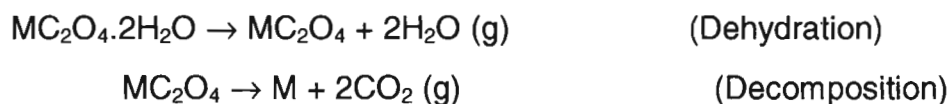
2.2.2 Characterisation of Furnace Products

The decomposition by TGA was done on a very small scale, with sample sizes typically being between 5 and 10 mg. The next step of the investigation was to scale up the experiment and to use samples of ca. 2 g, and to pyrolyse them in a tube furnace, again under a nitrogen atmosphere (Chapter 4). The resultant products were then characterised by XRD and SEM.

2.2.2.1 XRD

The pyrolysed, air sensitive products were coated in an epoxy glue, Pattex Epoxy Clear, to minimise oxidation while being examined by XRD; all manipulations were performed in an inert atmosphere glove box filled with dry, oxygen-free nitrogen. The results obtained for the thermal decomposition products of the single oxalates of iron, cobalt and nickel were the same as previously published [62,63, 67, 68, 72-78, 80].

The cobalt and nickel oxalates decomposed to their respective metals (Figure 2.4). The equations associated with this two step decomposition are as follows:



Where M is Co or Ni.

This result is consistent with the data obtained by TGA.

The decomposition product derived from the ferrous oxalate dihydrate showed the X-ray diffraction pattern of Fe_3O_4 (refer to Figure 2.5). The mass loss obtained by the TGA suggested the formation of FeO , however FeO is unstable below 573°C and therefore decomposes to Fe_3O_4 and Fe in the disproportionation reaction:

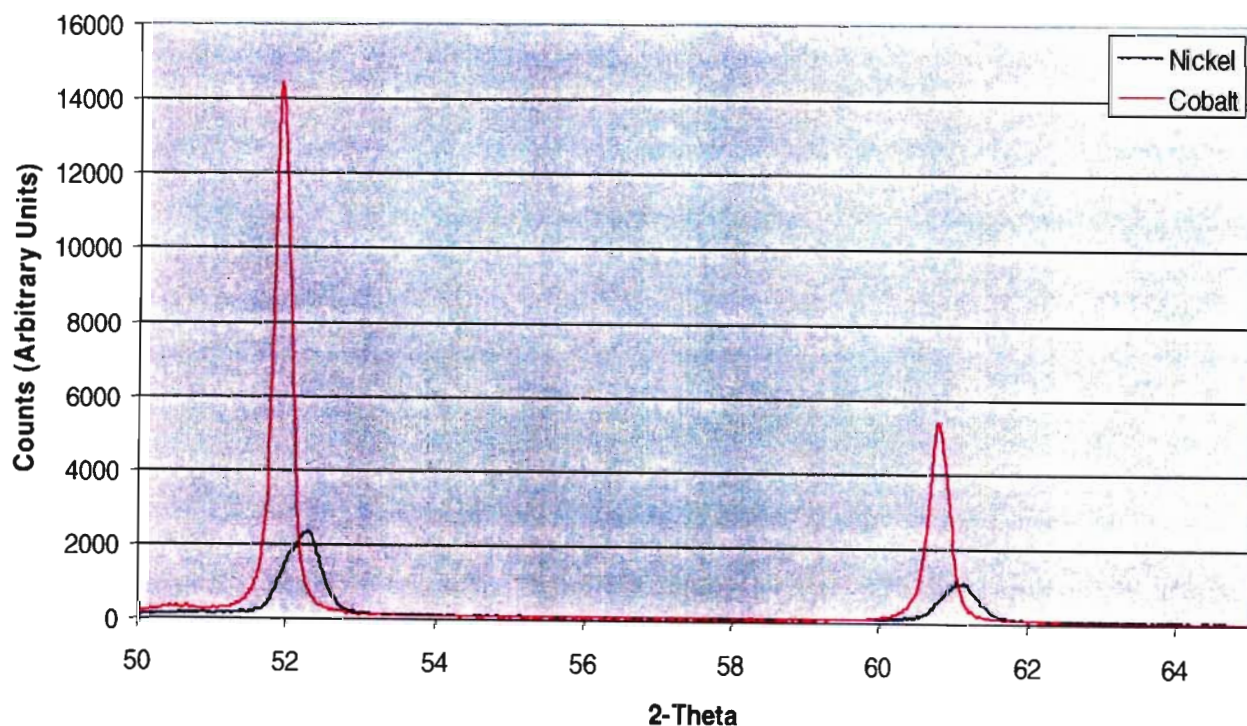
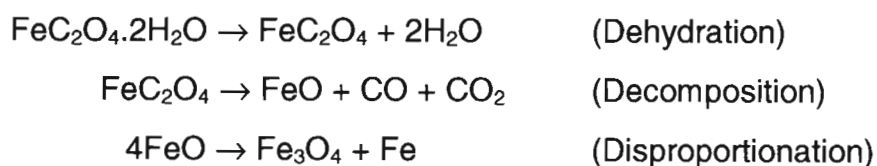


Figure 2.4: XRD patterns of cobalt and nickel, formed after pyrolysing $\text{CoC}_2\text{O}_4 \cdot 2\text{H}_2\text{O}$ and $\text{NiC}_2\text{O}_4 \cdot 2\text{H}_2\text{O}$ respectively, under a nitrogen atmosphere.

No evidence was found for metallic iron; however, this is not surprising, as the iron would be very dispersed, and probably exhibit very low long-range order. These results were consistent with those of Broadbent *et al.* [63], Nagase *et al.* [64], Macklen [68, 76], Galwey [69], and Nicholson [75].

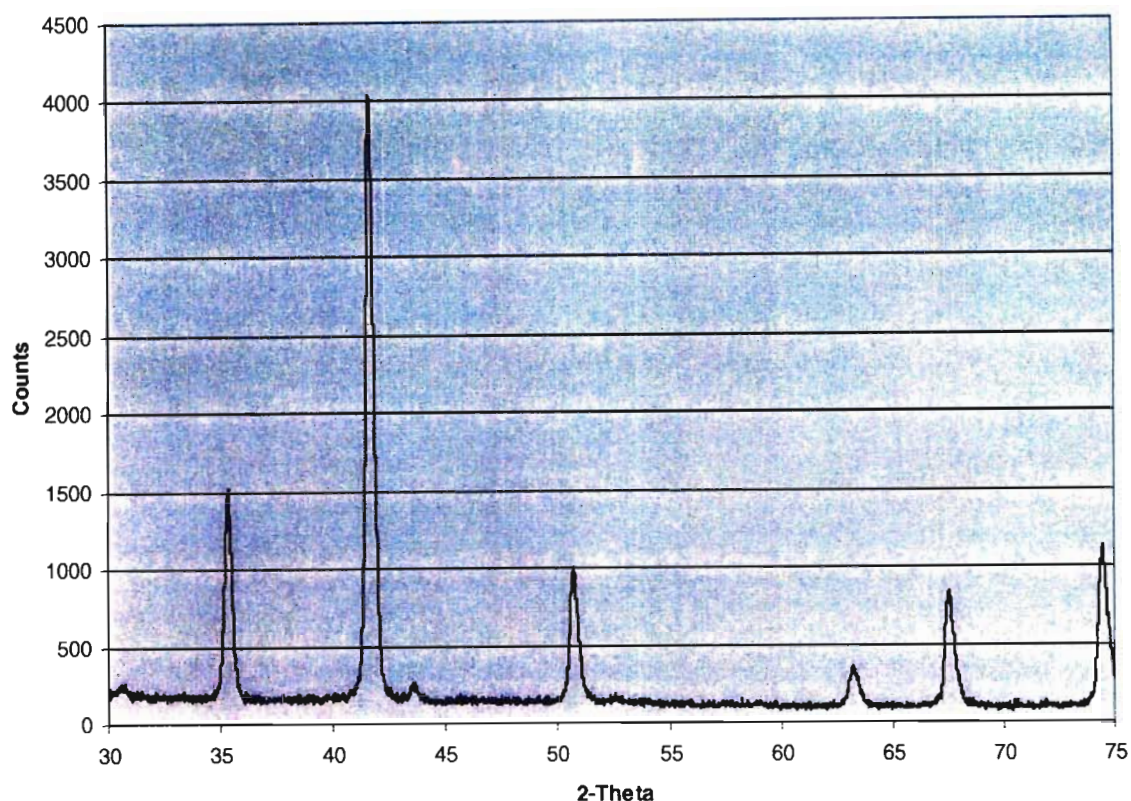


Figure 2.5 XRD pattern of Fe_3O_4 , formed after pyrolysing $FeC_2O_4 \cdot 2H_2O$ under nitrogen atmosphere.

2.2.2.2 SEM

In Figure 2.6 SEM photographs of the products obtained from the pyrolysis of the single oxalates are shown. Fissures, brought about by the escaping gases of the water of crystallisation and the CO or CO₂ can be most clearly seen in the SEM photographs of the ferrous oxalate decomposed product [Figure 2.6(a)]. In all cases it is interesting to note, although almost 70% w/v of the compound has been lost in the form of one gas or another, the overall volume of the crystals appears not to change. This implies that the metal powders produced, in the case of the cobalt and nickel oxalates, will be very reactive, as a result of their porous nature. The high reactivity of the metal powders to traces of oxygen present could also account for the production of Fe_3O_4 , in the case of the ferrous oxalate.

2.3 SYNTHESIS AND CHARACTERISATION OF BINARY OXALATES

As mentioned in Section 1.1.2, Schuele [90] prepared oxalates of the solid solutions of binary Fe-Co and Fe-Ni systems, and Gao *et al.* [37] and Gallagher [91] have prepared binary solid solutions of the Co-Ni system. They found a complete range of solution for all these systems.

In the present study binary solid solutions of the oxalates of the Fe-Co, Fe-Ni and Co-Ni systems were prepared in the molar ratios given in Table 2.5. The method of preparation was as in Section 2.1, with the metal sulfate solutions mixed in the correct molar proportions (Chapter 4). In Table 2.5, the percentage yields were good, all being above 96%. Because of these high yields, it was assumed that the resultant coprecipitated binary oxalates were of the correct stoichiometric ratios, and no further tests were performed to confirm this. Unfortunately microanalysis for % C and % H is of little assistance in this regard, because Fe, Co and Ni have very similar atomic weights.

Characterisation of the binary oxalates was by means of C and H microanalysis, IR spectroscopy, Malvern particle size analysis, SEM and XRD.

2.3.1 C and H Microanalysis

The microanalytical data for % C and % H (Table 2.6) are in good agreement the formulae of the binary solid solution proposed on the basis of the mole ratio of the metal sulfate salts used in the preparation (Table 2.5). The number of molecules of waters of crystallisation was also confirmed by the weight loss incurred on heating the sample, as determined thermogravimetrically.

Table 2.5: Percentage yields of binary oxalates and mole ratios used in the binary coprecipitation reactions

Exp. #	FeSO ₄ .7H ₂ O	CoSO ₄ .7H ₂ O	NiSO ₄ .7H ₂ O	% Yields
1(a)	3	1	-	97.8
1(b)	1	1	-	96.4
1(c)	1	3	-	97.2
2(a)	3	-	1	98.2
2(b)	1	-	1	97.1
2(c)	1	-	3	97.2
3(a)	-	3	1	98.7
3(b)	-	1	1	99.8
3(c)	-	1	3	97.4

Table 2.6: Elemental analysis of coprecipitated binary oxalates

Exp. #	Compound	C (%)	H (%)
1 (a)	Fe _{0.75} Co _{0.25} C ₂ O ₄ .2H ₂ O	13.15 (13.30)*	1.99 (2.23)
1 (b)	Fe _{0.50} Co _{0.50} C ₂ O ₄ .2H ₂ O	13.09 (13.25)	2.14 (2.22)
1 (c)	Fe _{0.25} Co _{0.75} C ₂ O ₄ .2H ₂ O	13.22 (13.20)	2.12 (2.22)
2 (a)	Fe _{0.75} Ni _{0.25} C ₂ O ₄ .2H ₂ O	13.28 (13.30)	2.24 (2.23)
2 (b)	Fe _{0.50} Ni _{0.50} C ₂ O ₄ .2H ₂ O	13.21 (13.24)	2.11 (2.22)
2 (c)	Fe _{0.25} Ni _{0.75} C ₂ O ₄ .2H ₂ O	13.20 (13.18)	2.18 (2.21)
3 (a)	Co _{0.75} Ni _{0.25} C ₂ O ₄ .2H ₂ O	13.12 (13.14)	2.19 (2.21)
3 (b)	Co _{0.50} Ni _{0.50} C ₂ O ₄ .2H ₂ O	12.96 (13.14)	1.96 (2.20)
3 (c)	Co _{0.25} Ni _{0.75} C ₂ O ₄ .2H ₂ O	13.02 (13.13)	2.06 (2.20)

*The figures in parentheses are the calculated values.

2.3.2 Infrared Spectroscopy

As with the single oxalates (Section 2.1.) vibrational assignments were made by comparison with values reported in the literature [40, 43-48]. The IR data for all three of the binary systems under investigation followed a similar trend, and thus only the data for the Fe-Ni system are given in Table 2.7. Tables A.1 and A.2 give the IR data of the other two systems (Appendix I).

The stretching frequencies found at *ca.* 3370 and 3130 cm^{-1} assigned as $\nu(\text{OH}_2)$, are very similar to those found for the waters of crystallisation in the single oxalates of iron, cobalt and nickel (Section 2.1). This shows that the bonding of the water molecules to the central metal ion of the bivalent metal oxalates is the same, whether the compound is single or binary.

The carbonyl stretching peaks at 1625, 1360 and 1315 cm^{-1} were also in good agreement with the single oxalates.

Table 2.7: Infrared spectra and vibrational assignments for the Fe-Ni coprecipitated binary oxalates in different molar ratios

Vibrational Assignment	Fe3:Ni1 (cm^{-1})	Fe1:Ni1 (cm^{-1})	Fe1:Ni3 (cm^{-1})
$\nu(\text{OH}_2)$	3360 br/s	3387 br/s	3383 br/s
$\nu(\text{OH}_2)$	3130 m/sh	3123 m/sh	3120 m/sh
$\nu_{\text{as}}(\text{C}=\text{O})$	1625 s	1624 s	1624 s
$\nu_{\text{sym}}(\text{C}-\text{O}) + \nu(\text{C}-\text{C})$	1360 m	1360 m	1360 m
$\nu_{\text{sym}}(\text{C}-\text{O}) + \delta(\text{O}-\text{C}=\text{O})$	1315 m	1315 m	1315 m
$\nu(\text{O}-\text{M}-\text{O})$	824 m	824 m	824 m
$\delta(\text{O}-\text{C}=\text{O}) + \nu(\text{M}-\text{O})$	776 m	775 s	765 m
$\nu(\text{O}-\text{M}-\text{O})$	738 m	735 w	730 m
$\nu(\text{M}-\text{O}) + \nu(\text{C}-\text{C})$	491 m	490 m	490 m

*br (broad); sh (shoulder); s (strong); m (medium); w (weak)

Inspection of the data in Table 2.8 shows that the peak positions and assignments are essentially the same whatever the composition of the binary oxalate and, indeed, match those for the single oxalates. This is to be expected, given that the various binary oxalates are isomorphous (see below) and, furthermore, have the same crystal structure as the centred monoclinic, α -form of the cobalt and nickel oxalates. As mentioned in Section 2.1, there is very little difference in the IR data of the single oxalates, and this also holds true for all the binary oxalate systems under investigation. A clearer picture of the crystal structures is gained from the XRD data (Figure 2.10).

2.3.3 Particle Size Analysis and SEM

Table 2.8 shows the results of the Malvern particle size analysis. Clarity of these trends is gained by the SEM photographs in Figures 2.7, 2.8 and 2.9.

Table 2.8: Mean particle size of coprecipitated ternary oxalates

Exp. #	Compound	Mean Particle Size
1 (a)	Fe ₃ :Co ₁	10.59 μm
1 (b)	Fe ₁ :Co ₁	13.06 μm
1 (c)	Fe ₁ :Co ₃	10.02 μm
2 (a)	Fe ₃ :Ni ₁	7.00 μm
2 (b)	Fe ₁ :Ni ₁	18.63 μm
2 (c)	Fe ₁ :Ni ₃	22.94 μm
3 (a)	Co ₃ :Ni ₁	38.87 μm
3 (b)	Co ₁ :Ni ₁	25.83 μm
3 (c)	Co ₁ :Ni ₃	24.47 μm

Figure 2.7 shows the SEM photographs of the Fe-Co binary oxalate system. What is immediately evident is the changing morphology of the crystals as the concentrations of the metal ions vary. The crystals in Figure 2.7(a) have morphology similar to that of the single oxalate in the greater concentration, namely the ferrous oxalate (refer back to Figure 2.1(a)). The crystals are block-like, with a length of ca. 10 μm and a width of 5 μm . There are also numerous smaller fragmented pieces. The crystals shown in Figure 2.7(c) have a similar morphology to that of cobalt oxalate (refer back to Figure 2.1(b)), with long needle-like crystals of the order of 10-20 μm in length. The morphology of the equimolar compound, Figure 2.7(b), shows a definite merging of the two crystal morphologies of ferrous and cobalt oxalates. Although the crystals are still needle-like, they are thicker and more robust, at about 15-30 μm in length and about 2 μm in width.

The same basic trend can be seen with the other two systems of Fe-Ni oxalate and Co-Ni binary oxalates. The morphologies change in such a way as to reflect the morphology of the single oxalate of the metal present in the highest proportion. The reasons for the increased mean particle size of these systems, as compared to those for the Fe-Co binary system, is that they tend to form conglomerates, a fact that is evident from Figures 2.8 and 2.9. We tentatively associate the conglomeration with the presence of nickel in the binary oxalate.

The *individual crystals* making up the conglomerates decrease in size with an increase in the nickel concentration. In the Fe-Ni system the crystals decrease in size from 5 μm in Figure 2.8(a) to 1 μm in Figure 2.8(c). The Co-Ni binary oxalate system is more difficult to size, as the groups of crystals are densely packed together. Figure 2.9(a), that applies to the molar ratio $\text{Co}_3\text{:Ni}_1$, shows the crystals to have a morphology resembling that of the needles obtained for the single cobalt oxalate (Figure 2.1(b)); however these are formed into large closely packed conglomerates. The equimolar Co-Ni binary oxalate (Figure 2.9(b)) has flake-like crystals, while the crystals in Figure 2.9(c) are more block-like in appearance, as is the single nickel oxalate (Figure 2.1(c)).

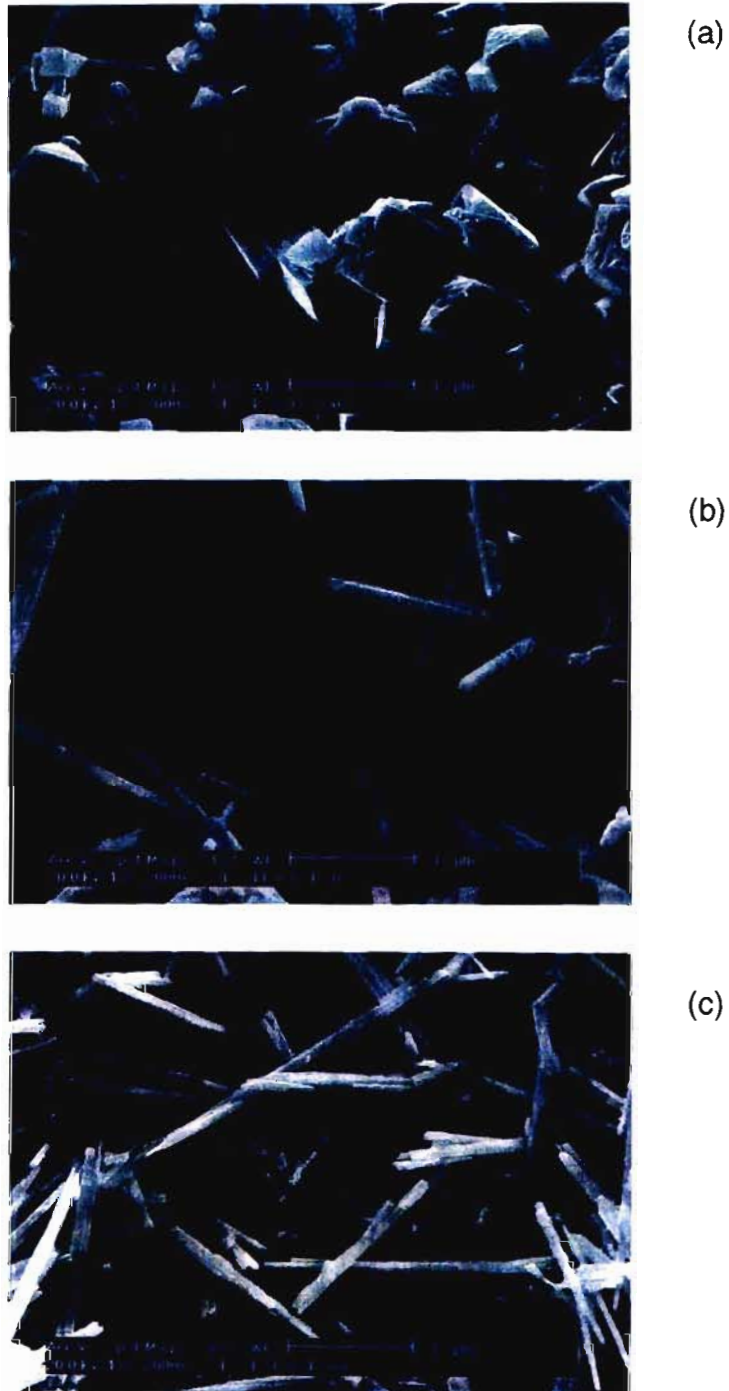


Figure 2.7: SEM photographs of the binary coprecipitated oxalates of Fe and Co in the ratios of (a) Fe₃:Co₁, (b) Fe₁:Co₁ and (c) Fe₁:Co₃

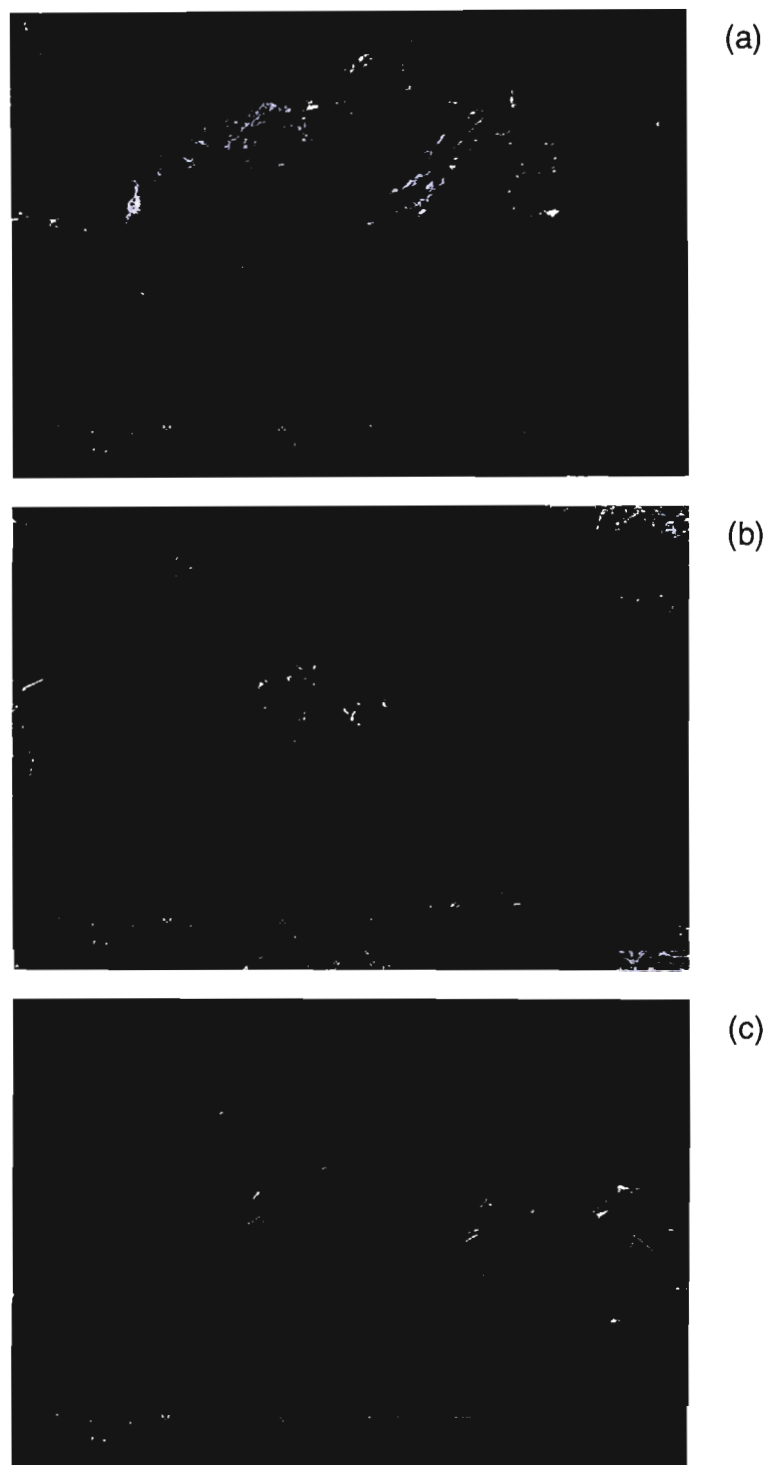


Figure 2.9: SEM photographs of binary coprecipitated oxalates of Co and Ni in the ratios of (a) Co₃:Ni₁, (b) Co₁:Ni₁ and (c) Co₁:Ni₃

The presence of a single morphology for each separate compound, instead of a mixture of the component morphologies for the individual single oxalates, indicates that solid solutions have been formed. This is in keeping with the findings of Schuele [90], Gao *et al.* [37] and Gallagher [91].

2.3.4 XRD

Although there is strong evidence that solid solutions were formed for all the binary oxalates under investigation, confirmation was obtained by X-ray diffraction. If any two metal oxalates did not form solid solutions, the X-ray patterns would consist of the two patterns for the individual single oxalates superimposed. If solid solutions were formed, the characteristic peaks on the patterns would be expected to lie between those of the pure components, assuming no phase change occurs and that the two parent oxalates have the same crystal structure.

2.3.4.1 Iron-Cobalt Binary Oxalate System

Figure 2.10 shows a comparison of the X-ray patterns for the physical mixtures with those recorded for the solid solutions obtained by coprecipitation of iron and cobalt oxalates. Whatever the Fe:Co mole ratio, the patterns of the physical mixtures are very different from those of the coprecipitates. As stated above, the X-ray patterns of the physical mixtures are composed of the two separate spectra superimposed. In the case of the Fe-Co system, the two patterns would be for iron(II) oxalate and cobalt(II) oxalate. This superimposition is most evident in the peaks at $21.54^\circ 2\theta$ and $22.04^\circ 2\theta$. The intensity of the peak at $21.54^\circ 2\theta$ decreases with the decrease in concentration of the ferrous oxalate. Other peaks that clearly show the presence of the ferrous oxalate are those at 28.96° and $32.92^\circ 2\theta$. These peaks are distinctive of the α -form of ferrous oxalate dihydrate (Figure 2.2), and decreased in intensity as the percentage concentration of ferrous oxalate was decreased.

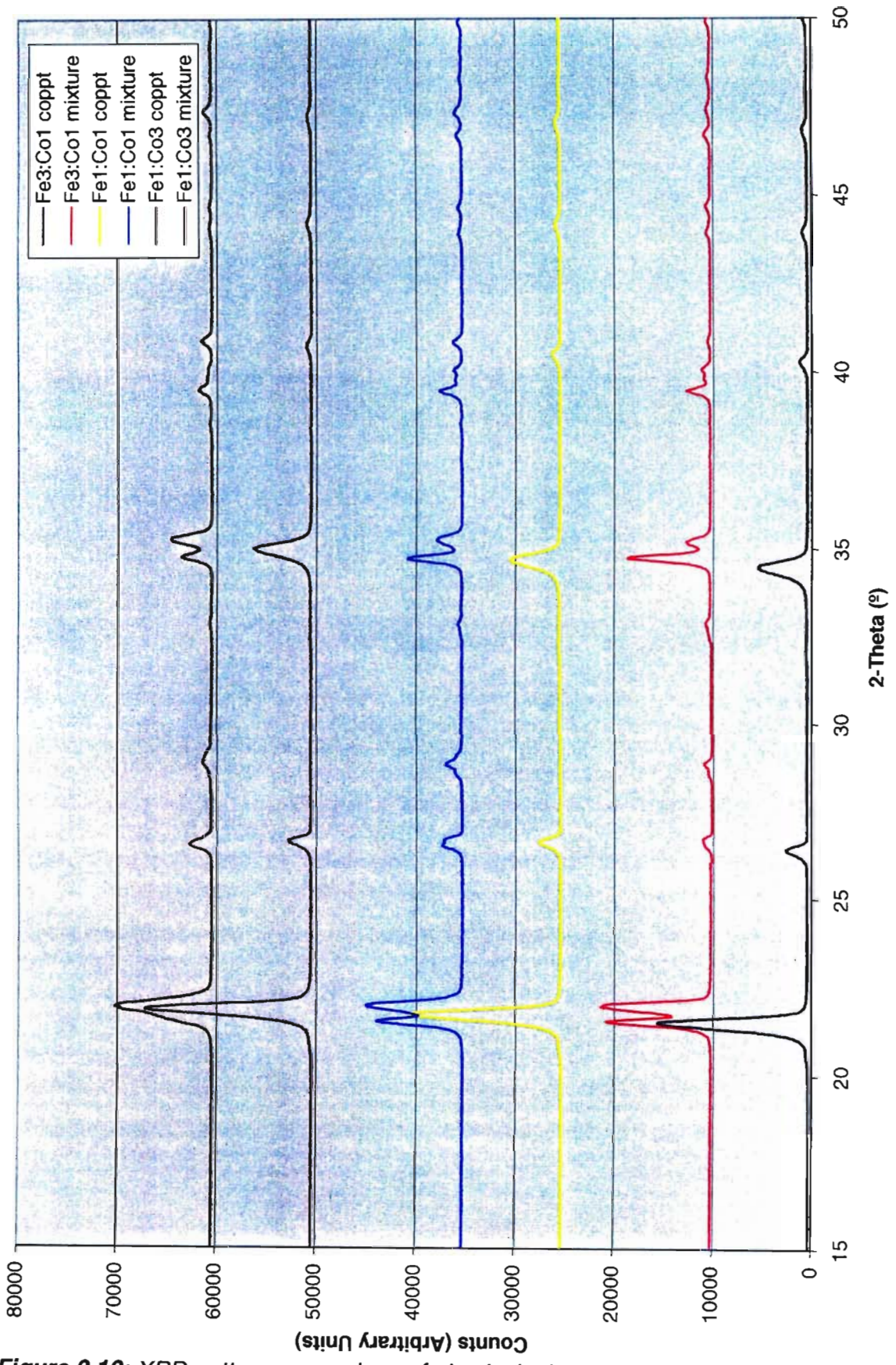


Figure 2.10: XRD pattern comparison of physical mixtures and coprecipitated Iron-Cobalt binary system

Table 2.9: Principal d^a -values (Å) for the Fe-Co oxalate system^b

CoC₂O₄	4.718	3.901	2.965	2.563	2.088	1.918	1.879
Fe_{0.25}Co_{0.75}C₂O₄	4.727	3.889	2.978	2.575	2.091	1.929	1.881
Fe_{0.50}Co_{0.50}C₂O₄	4.757	3.887	3.003	2.588	2.101	1.943	1.886
Fe_{0.75}Co_{0.25}C₂O₄	4.810	3.892	3.038	2.604	2.113	1.957	1.891

^aInterplanar spacing.

^bThe structures include two water molecules of crystallisation per formula unit.

As can be seen in the XRD patterns for the coprecipitated binary oxalates (Figure 2.10), there is a unique set of peaks for each of them. This indicates the formation of solid solutions, as expected with this system [90]. These peaks are consistent with that observed in the XRD spectra recorded for the α -form of cobalt (and nickel) oxalate dihydrate (Figure 2.2). Clearly, these binary solid solutions have the same crystal structure as the parent cobalt oxalate.

The principal d -values for the iron-cobalt system are given in Table 2.9. Significantly, there is a systematic shift in the peak positions to higher 2θ values (lower d values) as the concentration of the cobalt increased. This is consistent with a decrease in unit cell size as the larger Fe²⁺ ions are replaced by the slightly smaller Co²⁺ ions [$r(\text{Fe}^{2+}) = 0.76 \text{ \AA}$; $r(\text{Co}^{2+}) = 0.74 \text{ \AA}$] [95].

2.3.4.2 Iron-Nickel Binary Oxalate System

Figure 2.11 shows the XRD patterns for the solid solutions of the Fe-Ni system as well as those of physical mixtures prepared in the same mole ratio. For each composition there is a unique set of peaks for the solid solution, but two sets of peaks in the mixtures, corresponding to those of the single oxalates (Figure 2.2). The XRD patterns of the solid solutions confirm that they are isomorphous with the parent nickel oxalate dihydrate.

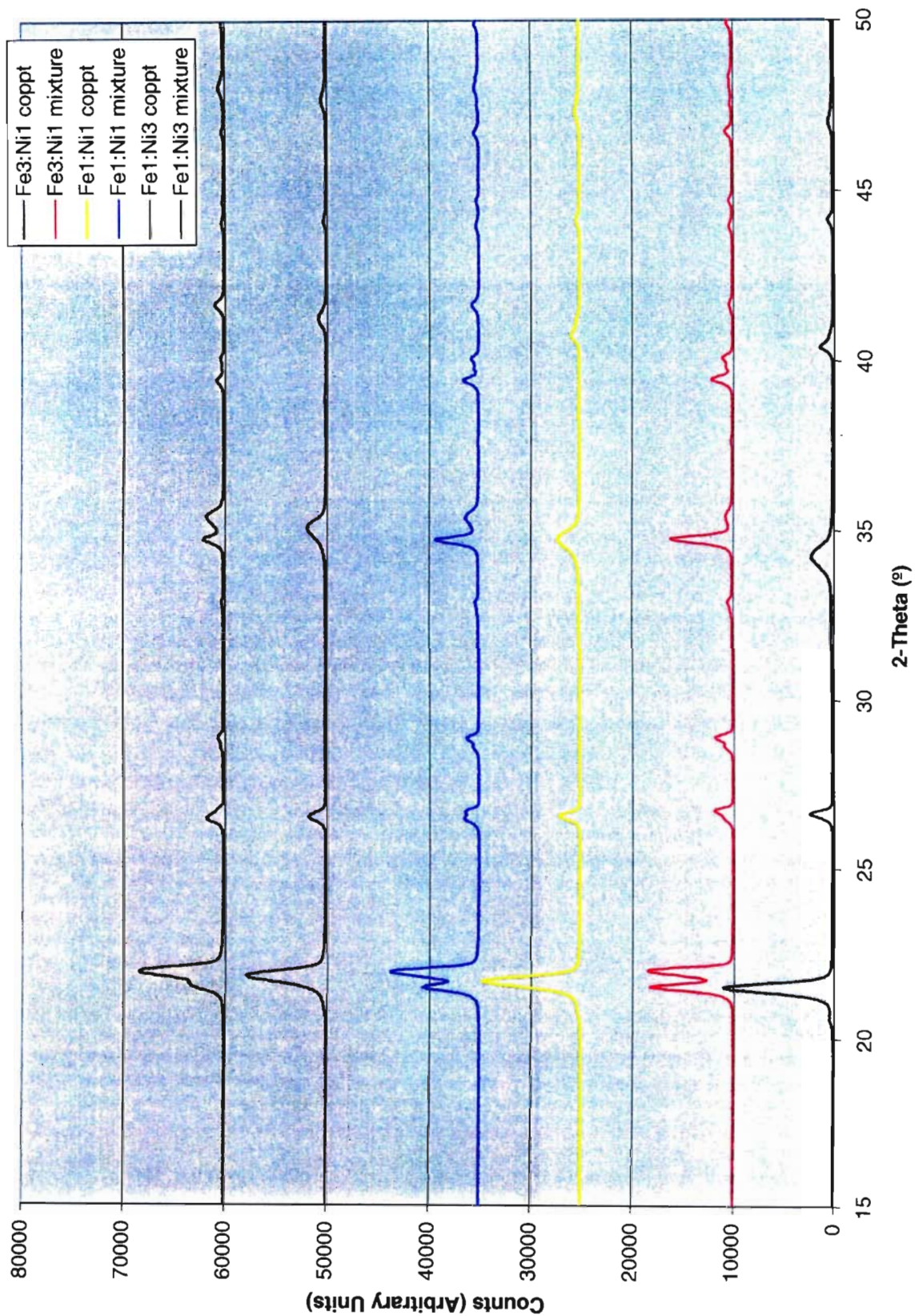


Figure 2.11: XRD pattern comparison of physical mixtures and coprecipitated Iron-Nickel binary system

As can be seen in Table 2.10, there was a shift to higher d -values as the ferrous concentration was increased. This is explained by the increased size of the Fe^{2+} ion relative to that of Ni^{2+} , [$r(\text{Fe}^{2+}) = 0.76 \text{ \AA}$; $r(\text{Ni}^{2+}) = 0.72 \text{ \AA}$] [95], thus the higher the concentration of the ferrous ion, the larger the unit cell edge length becomes.

Table 2.10: Principal d^a -values (\AA) for the Fe-Ni binary oxalate system^b

NiC₂O₄	4.693	3.904	2.937	2.517	2.060	1.901	1.862
Fe_{0.25}Ni_{0.75}C₂O₄	4.723	3.898	2.966	2.544	2.089	1.964	1.872
Fe_{0.50}Ni_{0.50}C₂O₄	4.757	3.898	2.998	2.574	2.094	1.987	1.888
Fe_{0.75}Ni_{0.25}C₂O₄	4.792	3.887	3.006	2.594	2.099	2.005	1.891

^aInterlayer spacing.

^bThe structures include two water molecules of crystallisation per formula unit.

2.3.4.3 Cobalt-Nickel Binary Oxalate System

The coprecipitates of this binary system again show a single X-ray pattern unique to each compound (Figure 2.12). These compounds are clearly isomorphous, and have the same crystal structure as the α -form of the parent cobalt and nickel oxalates. It is because cobalt and nickel oxalates are isomorphous that it is difficult to discern the differences in the X-ray patterns for the physical mixtures and coprecipitates of the Co-Ni system (Figure 2.12). However, the X-ray patterns for the physical mixtures of the Co-Ni system, are differentiated from each other by the relative heights of the two peaks at 26.5° and 35.3° 2θ . It seems that the relative height of the 35.3° 2θ peak increases as the percentage of nickel oxalate increases. This trend is not observed for the coprecipitated compounds, as expected for a solid solution.

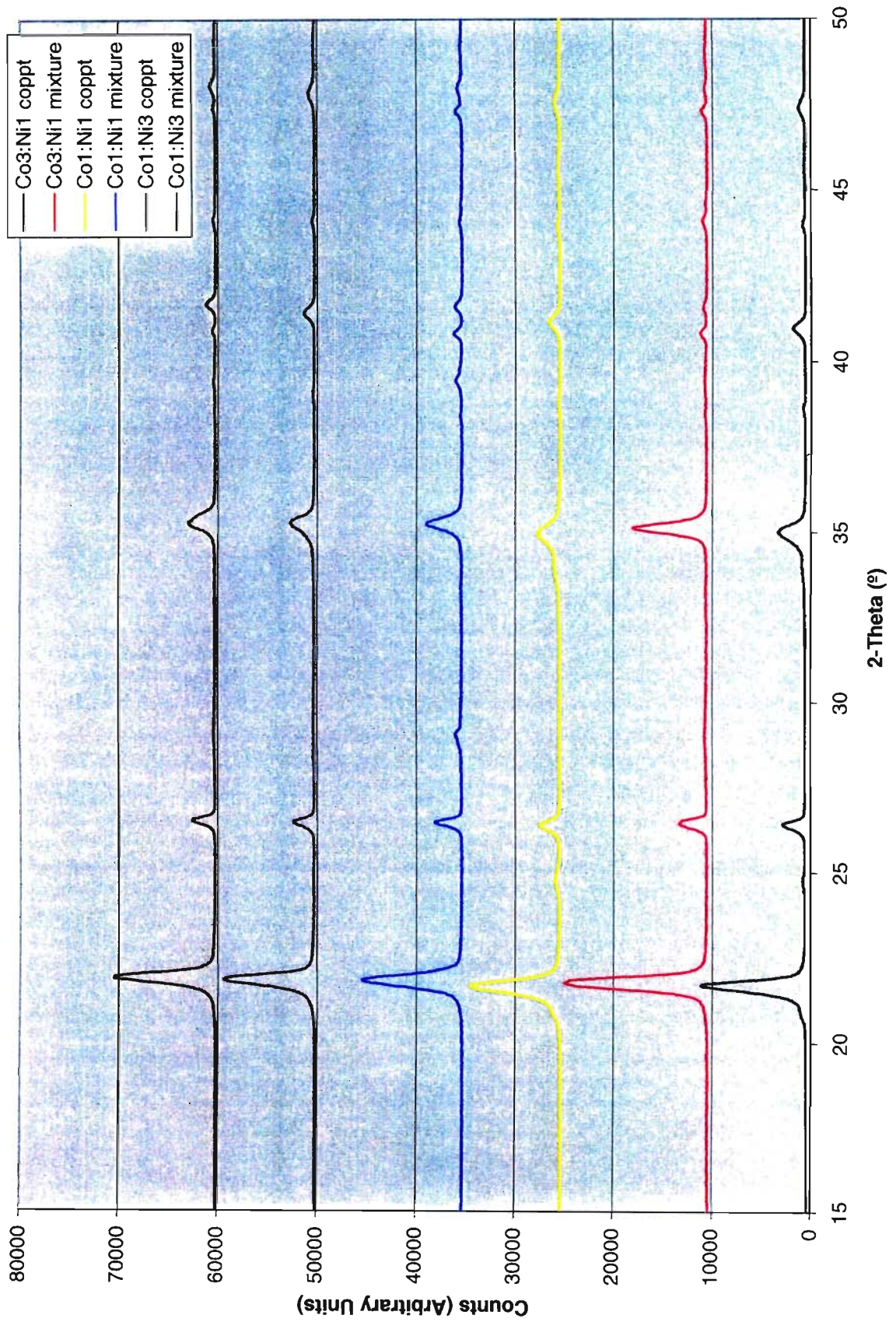


Figure 2.12: XRD pattern comparison of physical mixtures and coprecipitated Cobalt- Nickel binary system

In Section 2.1, it was established that cobalt oxalate has a peak at $35.16^\circ 2\theta$, and nickel oxalate has a peak at $35.50^\circ 2\theta$. Therefore when these compounds are mixed together, the peak at $35.3^\circ 2\theta$ is the result of the overlap of their respective peaks. By closer analysis of this peak, (using PeakFit version 4), in the sample containing an equimolar proportion of cobalt and nickel oxalate, it was found that there was indeed overlap, and that the two separated peaks corresponded exactly with the 2θ values of the single oxalates in question. It can therefore be concluded, that the physical mixing of two single oxalates did not cause any change in their crystal structures. These results are consistent with those of Gao [37] and Schuele [90].

Table 2.11 gives the principal d -values of the single oxalates of cobalt and nickel, and those of the coprecipitated Co-Ni binary oxalates. As with the other two systems under investigation, there is an decrease in unit cell size, and corresponding decrease in the d values, as the concentration of the smaller nickel ion increases, [$r(\text{Co}^{2+}) = 0.74 \text{ \AA}$; $r(\text{Ni}^{2+}) = 0.72 \text{ \AA}$] [95].

Table 2.11: Principal d^a -values (\AA) for the Co-Ni binary oxalate system^b

CoC₂O₄	4.718	3.901	2.965	2.563	2.088	1.918	1.879
Co_{0.75}Ni_{0.25}C₂O₄	4.761	3.921	2.986	2.559	2.086	1.915	1.876
Co_{0.50}Ni_{0.50}C₂O₄	4.753	3.916	2.978	2.546	2.081	1.911	1.871
Co_{0.25}Ni_{0.75}C₂O₄	4.718	3.913	2.955	2.531	2.075	1.909	1.869
NiC₂O₄	4.693	3.904	2.937	2.517	2.060	1.901	1.862

^aInterlayer spacing.

^bThe structures include two water molecules of crystallisation per formula unit.

The X-ray patterns of the coprecipitated oxalates of all three systems showed the symmetrical peaks of a single pattern, confirming the formation of solid solutions. These results agree with those from the SEM, and are confirmed by the results obtained from the TGA (Section 2.2.2).

2.4 PYROLYSIS STUDIES OF BINARY OXALATES

Since each of the systems under investigation is different, their results are reported and discussed separately.

2.4.1 *Thermogravimetric Analysis*

2.4.1.1 *Iron-Cobalt System*

The TGA traces of the Fe-Co system are shown in Figure 2.13. Table 2.12 gives the temperatures of dehydration and decomposition and the weight losses obtained from these curves.

It is apparent that each of the coprecipitated binary oxalates has a different dehydration and decomposition temperature. All the coprecipitated binary oxalates exhibited a two step curve i.e., a single step dehydration followed by the decomposition step. This behaviour is typical of solid solutions, as was found by Schuele [90].

The traces of the coprecipitated oxalates are contrasted in Figure 2.13, with the TGA curves obtained from the physical mixtures of the single oxalates in the same molar ratios. The multi-step profile is indicative of the individual single oxalates dehydrating and decomposing at their individual temperatures. Also apparent from Figure 2.13, is the difference in final weight loss between the coprecipitates and the physical mixtures. The final weight loss of the coprecipitated binary oxalates corresponds to the formation of the metal or the alloy. On the other hand, as reported earlier (Section 2.1.2), $\text{FeC}_2\text{O}_4 \cdot 2\text{H}_2\text{O}$ decomposes to Fe_3O_4 . This suggests that the presence of cobalt in the binary mixture changes the thermodynamics sufficiently to cause metal rather than oxide formation. This occurs even when the ferrous ion is in 3:1 excess.

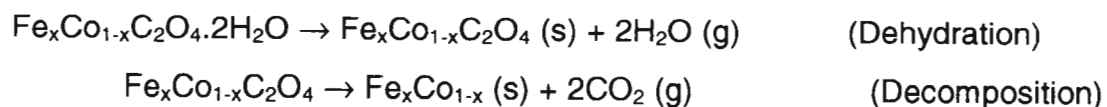
Table 2.12 Temperatures of dehydration, decomposition and weight losses for binary coprecipitated iron-cobalt oxalate system under N_2 at ramp rate of $5^\circ/\text{min}$

Iron-Cobalt Oxalate	Dehydration ($^\circ\text{C}$)	% Weight Loss	Decomposition ($^\circ\text{C}$)	% Weight Loss
(a) Fe3:Co1	165	19.02 (19.94)	270	68.02 (68.66)
(b) Fe1:Co1	160	19.42 (19.86)	280	68.22 (68.37)
(c) Fe1:Co3	155	18.21 (19.77)	300	67.79 (68.08)

The figures in parentheses are the calculated, theoretical values.

The weight loss of 18.21% at 155°C for $\text{Fe}_{0.25}\text{Co}_{0.75}\text{C}_2\text{O}_4 \cdot 2\text{H}_2\text{O}$ [Figure 2.13(c)] was less than expected for the loss of two waters of crystallisation. This phenomenon has been observed by Gao *et al.* [37], who postulated that the crystallised water had already been partially lost before the compound was placed in the thermogravimetric analyser. This is especially likely, when the synthesised oxalate powder has a very small particle size, and therefore a greater surface area from which water can be lost. Decomposition at 300°C corresponded to the formation of the metal or alloy, with a weight loss of 67.79%.

The weight loss data for all the Fe-Co binary compounds correspond to the reaction:



2.4.1.2 Iron-Nickel Binary Oxalate System

As with the Fe-Co system, the Fe-Ni system was studied by Schuele [90]. The findings of this study were in agreement with Schuele [90]. The coprecipitated binary oxalates again showed a well-defined two step decomposition profile, corresponding to (i) the dehydration followed by (ii) the decomposition of the oxalates in question (Table 2.13 and Figure 2.14).

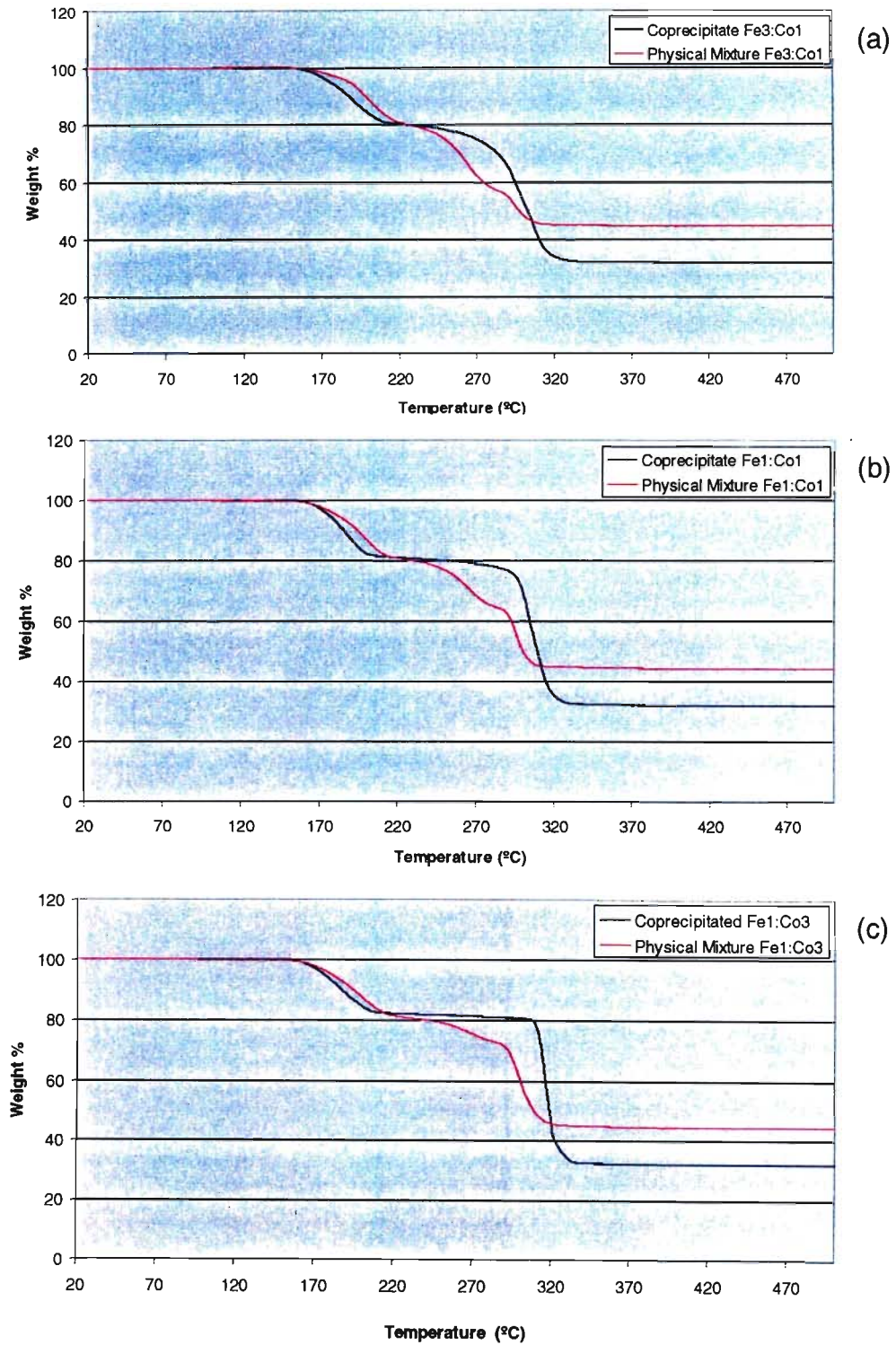


Figure 2.13: TGA traces of iron-cobalt system, at 5°C/min under N₂

Table 2.13: Temperatures of dehydration, decomposition and weight losses for binary coprecipitated iron-nickel oxalate system under N_2 at ramp rate of $5^\circ/\text{min}$

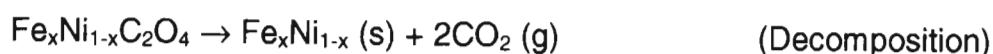
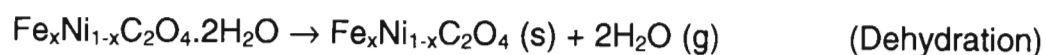
Iron-Nickel Oxalate	Dehydration ($^\circ\text{C}$)	% Weight Loss	Decomposition ($^\circ\text{C}$)	% Weight Loss
(a) Fe3:Ni1	165	19.68 (19.95)	250	68.35 (68.68)
(b) Fe1:Ni1	170	20.27 (19.81)	270	68.13 (68.41)
(c) Fe1:Ni3	175	19.81 (19.79)	300	67.83 (68.15)

The figures in parentheses are the calculated, theoretical values.

The two step profile of the coprecipitated oxalates is strongly contrasted by the TGA traces of the physical mixtures. These traces show a multi-step decomposition, which indicates the different dehydration and decomposition temperatures of the single oxalates of iron and nickel. As with the Fe-Co system, the final weight loss for the physical mixtures is consistent with the formation of the iron oxide, as expected from the results obtained for ferrous oxalate.

The equimolar Fe-Ni compound [Figure 2.14(b)] lost more weight (20.27 %) than expected for the dehydration process. As with the compound in the cobalt ferrous system that had previously lost some water, the difference between theory and experiment may be associated with an especially large surface area. However, in this case it appears that the large surface area makes the compound vulnerable to the absorption of water in humid environments.

As with the Fe-Co binary system, the weight loss data for all the Fe-Ni binary compounds corresponded to the reactions:



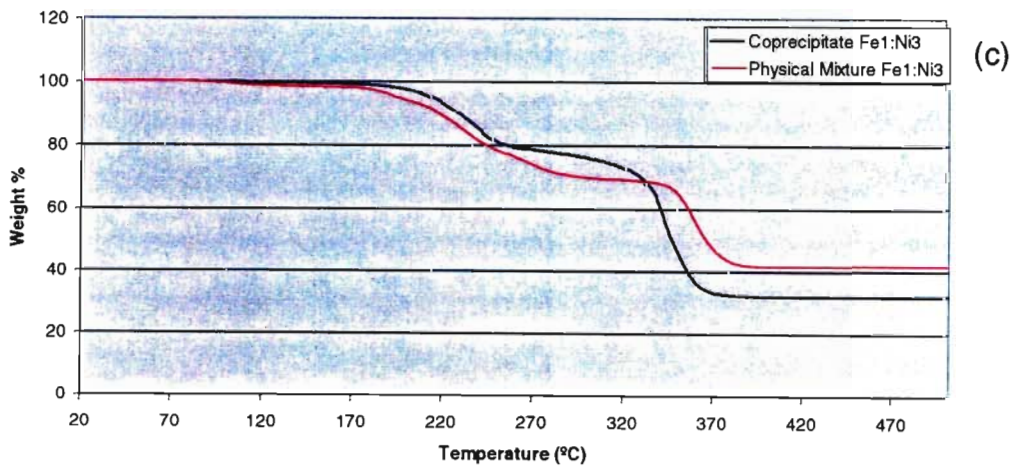
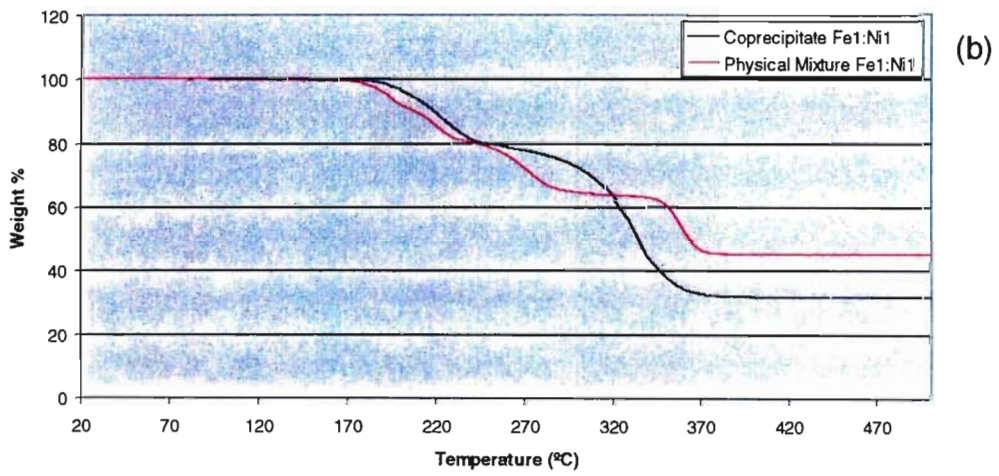
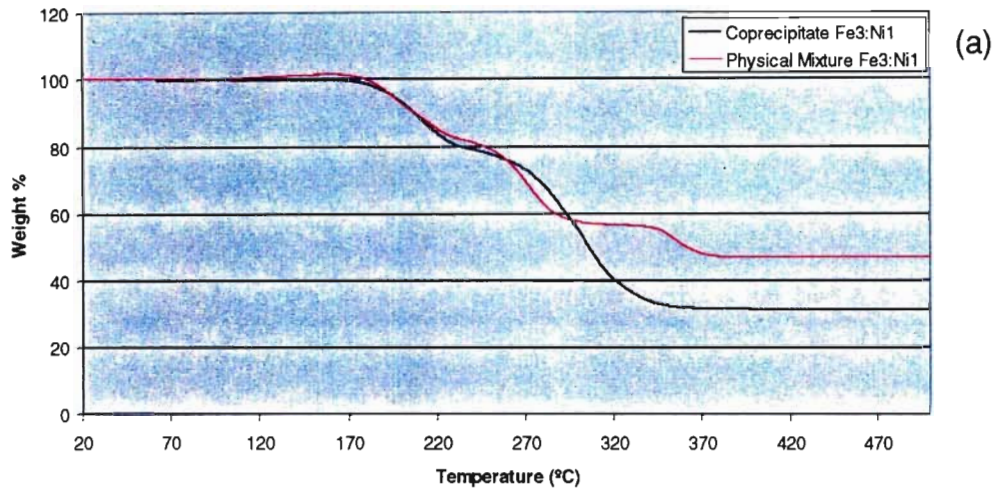


Figure 2.14: TGA traces of iron-nickel system, at 5°C/min under N₂

2.4.1.3 Cobalt-Nickel Binary Oxalate System

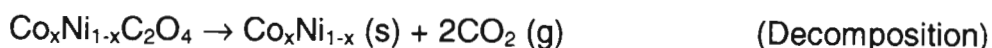
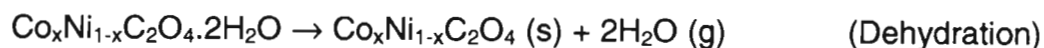
Again there was a marked difference in the TGA traces of the coprecipitated oxalates and the physical mixtures (Figure 2.15). There was the well-defined two step decomposition of the coprecipitates versus the multi-step dehydration and decomposition profiles of the physical mixtures (Table 2.14). Both the physical mixtures and the coprecipitates of the Co-Ni system decomposed to the metal, the products showing no sign of oxidation. For the physical mixtures, this is due to the fact that the two single oxalates of cobalt and nickel decomposed to the metal, as discussed previously, and physical mixing does not alter the crystal structure in any way, as seen by the XRD data (Figure 2.12).

Table 2.14: Temperatures of dehydration, decomposition and weight losses for binary coprecipitated cobalt-nickel oxalate system under N_2 at ramp-rate $5^\circ/\text{min}$

Cobalt-Nickel Oxalate	Dehydration ($^\circ\text{C}$)	% Weight Loss	Decomposition ($^\circ\text{C}$)	% Weight Loss
(a) Co3:Ni1	170	19.19 (19.71)	360	67.53 (67.86)
(b) Co1:Ni1	170	19.53 (19.69)	350	67.28 (67.84)
(c) Co1:Ni3	190	19.93 (19.68)	345	67.54 (67.82)

The figures in parentheses are the calculated, theoretical values

As with the other two binary systems, the weight loss data for all the Co-Ni binary compounds corresponded to the reactions:



All three of the systems under investigation exhibited extreme sensitivity to air. When the nitrogen was switched off and air allowed back into the system, all the residues without exception gained weight and changed colour from grey to black, indicating oxidation of the metals. In the case of the samples containing iron, the compounds exhibited pyrophoric behaviour. This would indicate that very reactive, high surface area metal powders were produced, and that even at room temperature were rapidly oxidised by air. This is in accordance with the results of Gao *et al.* [37] and Broadbent *et al.* [55].

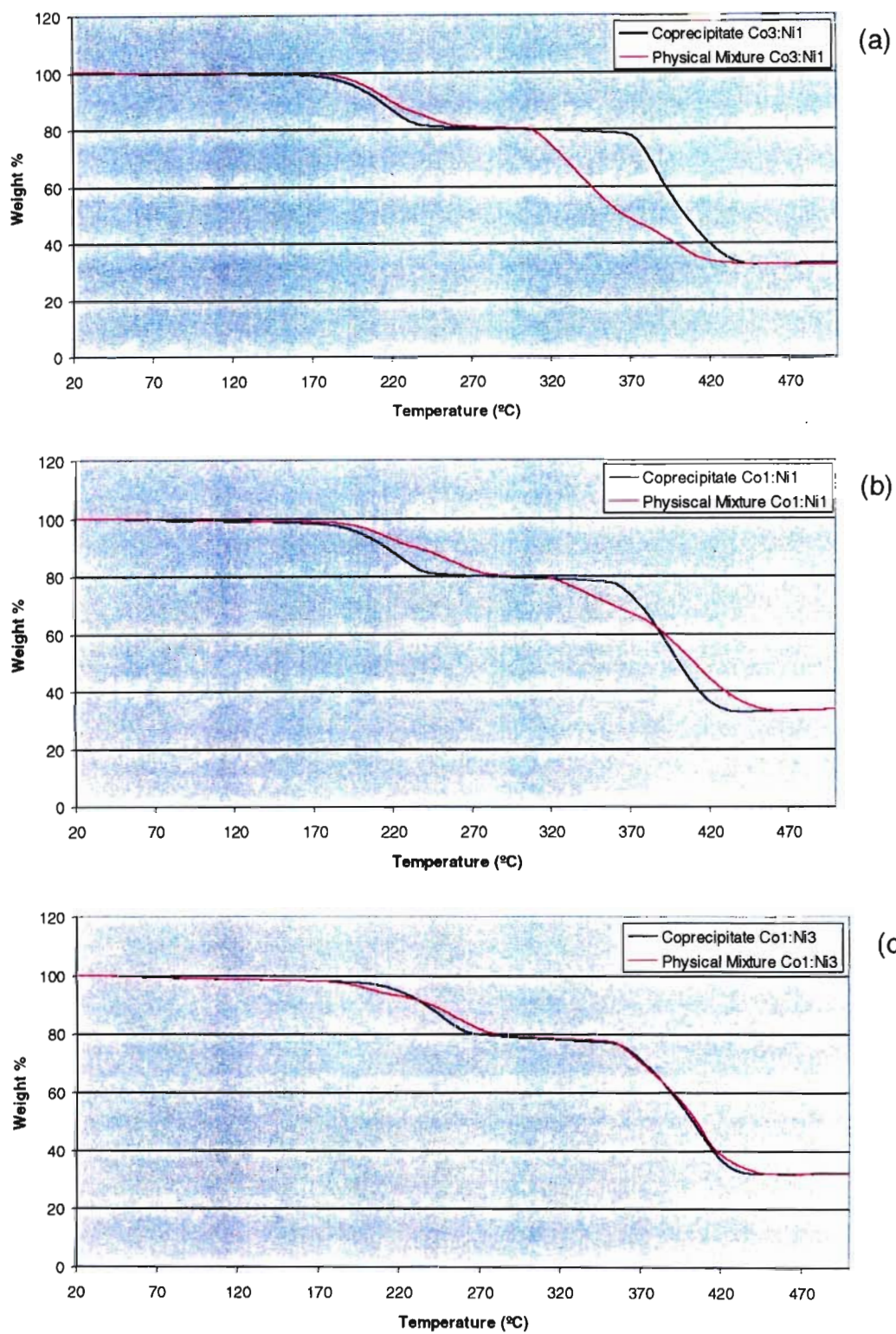


Figure 2.15: TGA traces of cobalt-nickel system, at 5°C/min under N₂

2.4.2 Characterisation of Furnace Products

Scale up of the experiment was carried out using sample masses of ca. 2 g, that were pyrolysed in a tube furnace, under a nitrogen atmosphere (Chapter 4). The resultant products were then characterised by XRD and SEM.

XRD

In all cases the pyrolysis products were found to be extremely oxygen sensitive, and so, precautions were taken to prevent contact with air (see Chapter 4 for experimental details). Given the weight losses calculated from the TGA, the resultant products of decomposition of all the coprecipitated binary oxalate systems under investigation were expected to be the metals or the alloys.

2.4.2.1 Iron-Cobalt Binary Oxalate System

As predicted, the coprecipitated oxalates of the iron-cobalt system pyrolysed to the alloy, as evidenced by the XRD patterns (Figure 2.16). Table 2.15 gives the d -values of the peaks in Figure 2.16. As found by Schuele [90], a single, body-centred cubic (bcc) alloy phase was found for the pyrolysis products from the Fe₃:Co₁ and Fe₁:Co₁ samples. This phase is analogous to the low temperature α -Fe bcc phase. The pyrolysis product from the Fe₁:Co₃ sample exhibited a face-centred cubic (fcc) phase which is in agreement with the phase diagram for the bulk iron-cobalt alloy [140].

Table 2.15: Principal d -values (Å) for the pyrolysis products of the Fe-Co oxalate system

Alloy	d -values (Å)			
Fe _{0.75} Co _{0.25}	2.025	1.434	1.171	
Fe _{0.50} Co _{0.50}	2.010	1.429	1.169	
Fe _{0.25} Co _{0.75}	2.046	1.770	1.252	1.067

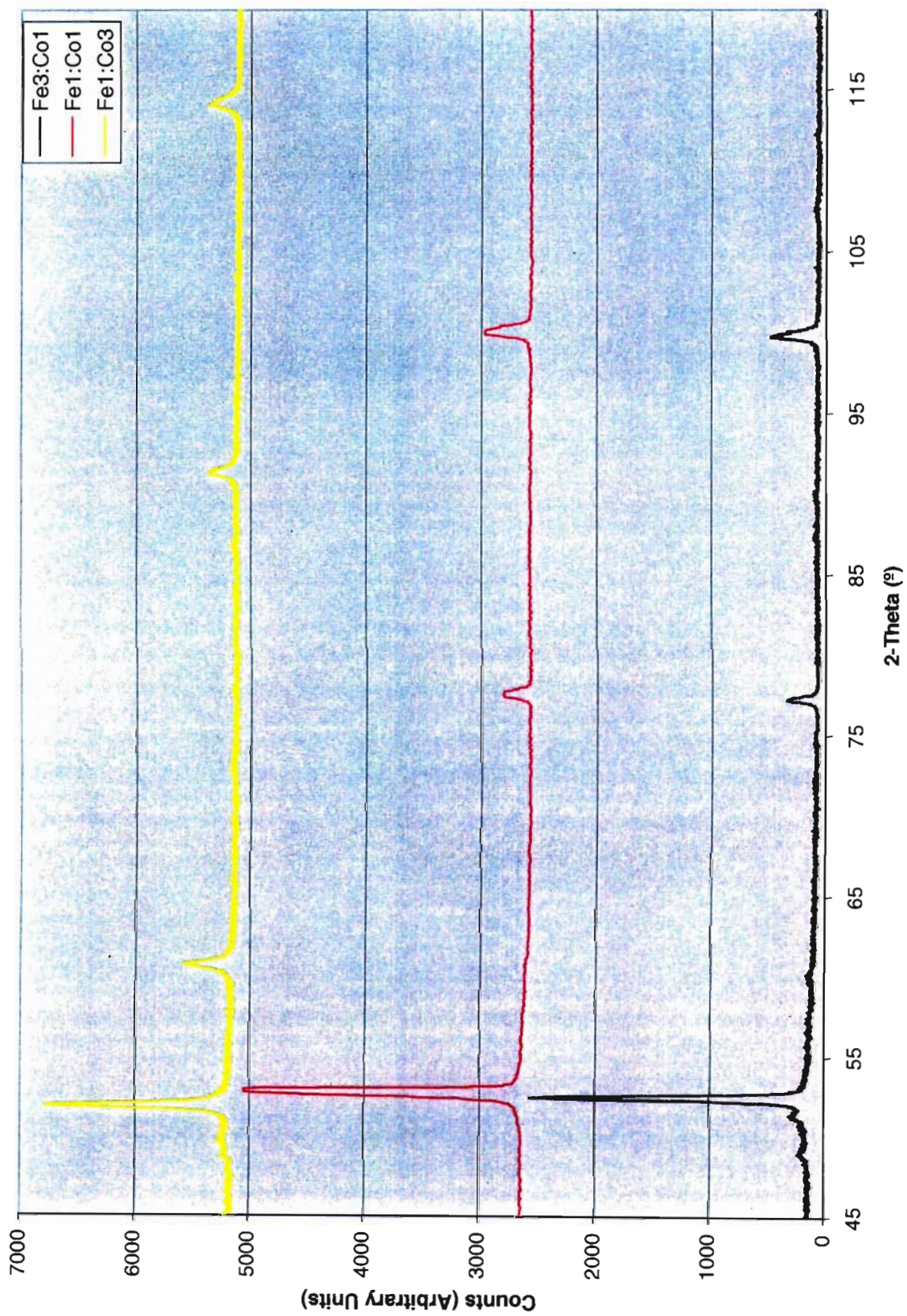


Figure 2.16: XRD pattern of Fe-Co oxalate system pyrolysis products

2.4.2.2 Iron-Nickel Binary Oxalate System

The iron-nickel system also produced alloys, again in accordance to Schueles' [90] findings. The XRD results (Figure 2.17) clearly show the single patterns characteristic of alloys. As with the iron-cobalt system the Fe₃:Ni₁ and Fe₁:Ni₁ compounds pyrolysed to a bcc, low temperature (α -Fe) solid solution. On the other hand, the Fe₁:Ni₃ sample decomposed to the fcc phase of the iron-nickel alloy. This is in accordance with the binary phase diagram of iron-nickel [140]. Table 2.16 gives the principal d values of the peaks shown in Figure 2.17 for each alloy.

Table 2.16: Principal d -values (Å) for the pyrolysis products of the Fe-Ni oxalate system

Alloy	d values (Å)			
Fe _{0.75} Ni _{0.25}	2.015	1.433	1.171	
Fe _{0.50} Ni _{0.50}	2.010	1.430	1.170	
Fe _{0.25} Ni _{0.75}	2.046	1.772	1.251	1.067

2.4.2.3 Cobalt-Nickel Binary Oxalate System

The XRD patterns confirmed the production of the alloy, as discrete patterns of peaks are seen (Figure 2.18). For all three alloy compositions the pattern is that of the face-centred cubic (fcc) system. Table 2.17 gives the d -values of the different alloys of the Co-Ni binary system. Since nickel has a smaller atomic radius than cobalt, the observed trend of decreasing d values as the concentration of nickel is increased, was expected.

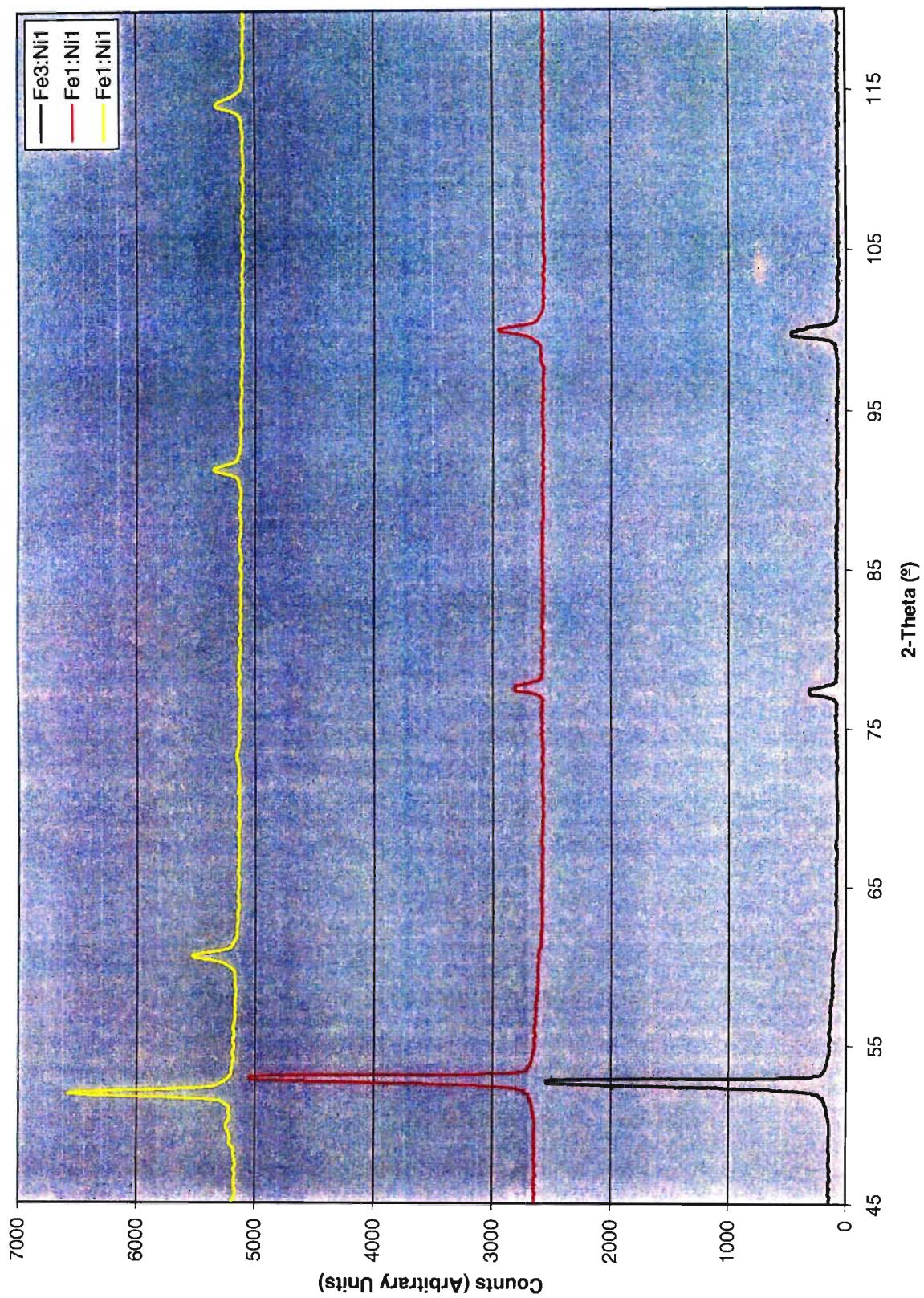


Figure 2.17: XRD pattern of Fe-Ni oxalate system pyrolysis products

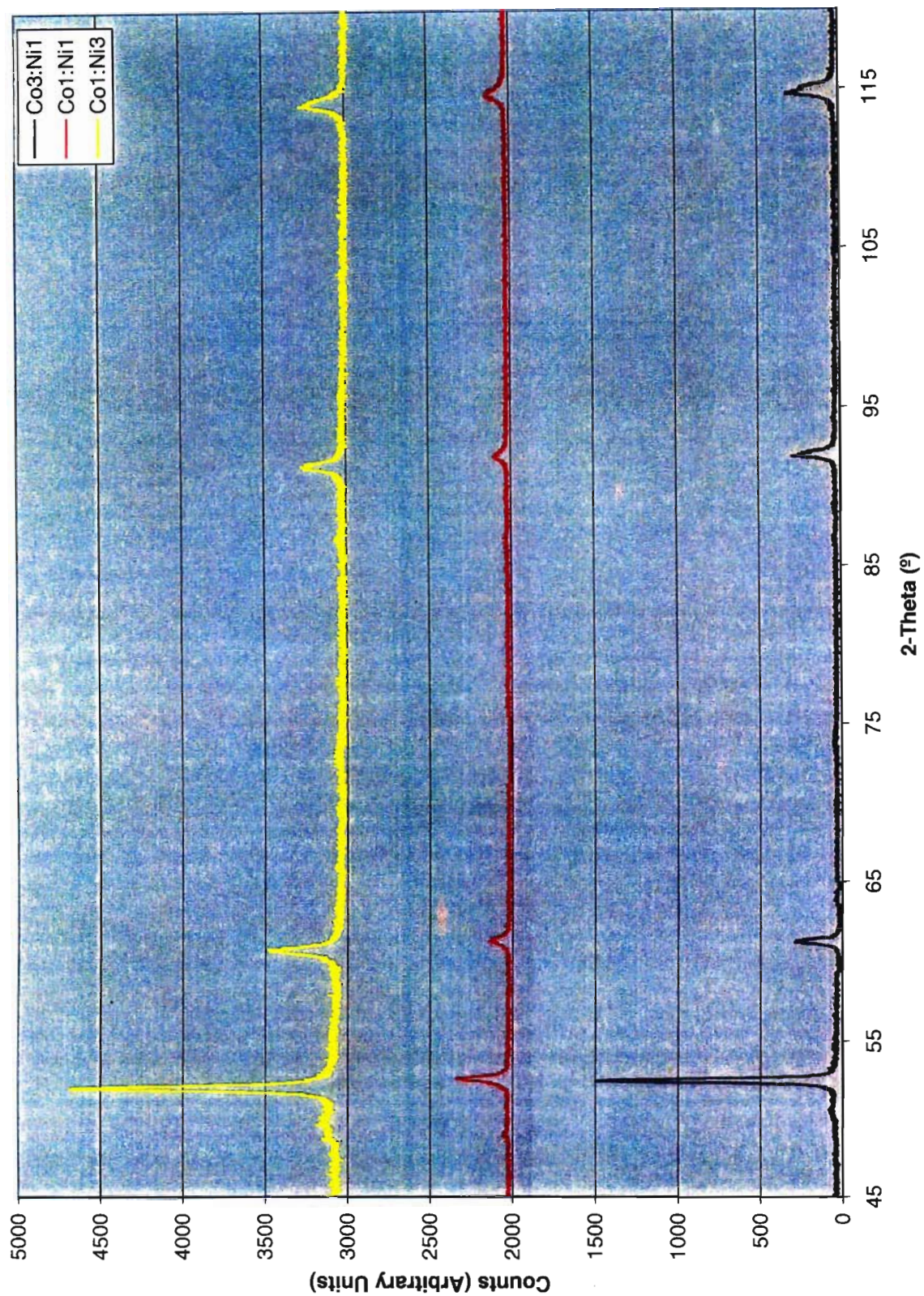


Figure 2.18: XRD pattern of Co-Ni oxalate system pyrolysis products

Table 2.17: Principal *d*-values (Å) for the pyrolysis products of the Co-Ni oxalate system

Alloy	<i>hkl</i>			
	111	200	220	311
Co	2.047	1.772	1.253	1.069
Co_{0.75}Ni_{0.25}	2.046	1.770	1.252	1.067
Co_{0.50}Ni_{0.50}	2.040	1.766	1.247	1.065
Co_{0.25}Ni_{0.75}	2.034	1.763	1.246	1.064
Ni	2.034	1.762	1.246	1.062

SEM

The SEM photographs shown in Figure 2.19, for the Fe-Co system, clearly show fissures and cracks caused by the loss of H₂O and CO₂. This is most evident in the compound with block-like crystals and with the highest iron content (Figure 2.19(a)). The morphologies exhibited by the other two Fe-Co systems are more needle-like, and thus it is more difficult to see the fissures. What is immediately evident, as with the single oxalates discussed earlier (Section 2.1), is that there has been very little change in size or volume of the pyrolysis product, although there has been a weight loss of nearly 70%.

The other two systems, shown in Figures 2.20 and 2.21 for Fe-Ni and Co-Ni, respectively, show the same trend as discussed above i.e., a visible deterioration of the crystals, indicated by cracks and fissures, but no decrease in size or volume from the starting material.

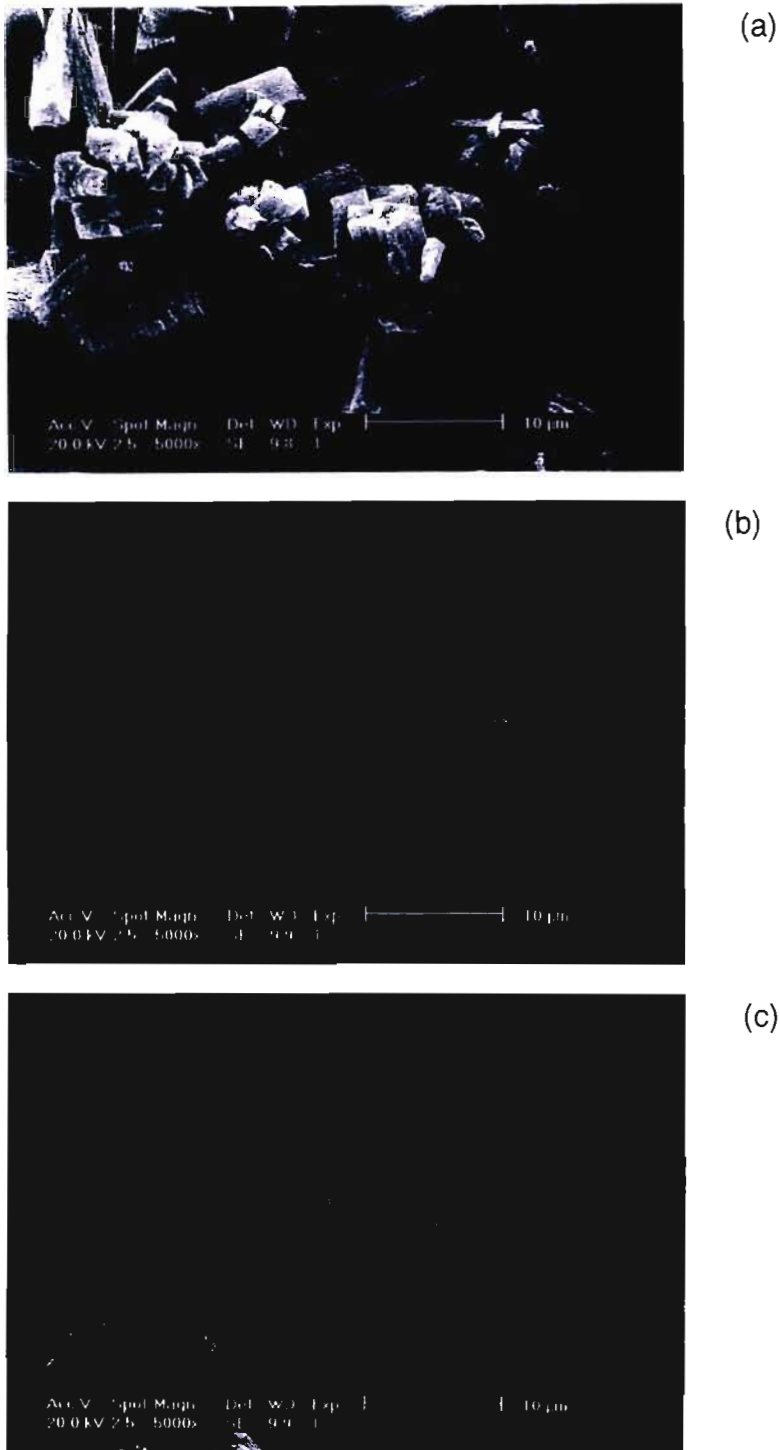


Figure 2.19: SEM photographs of binary coprecipitated oxalates of Fe and Co in the ratios of (a) Fe₃:Co₁, (b) Fe₁:Co₁ and (c) Fe₁:Co₃ pyrolysed under N₂ atmosphere at 390°C for 1hour

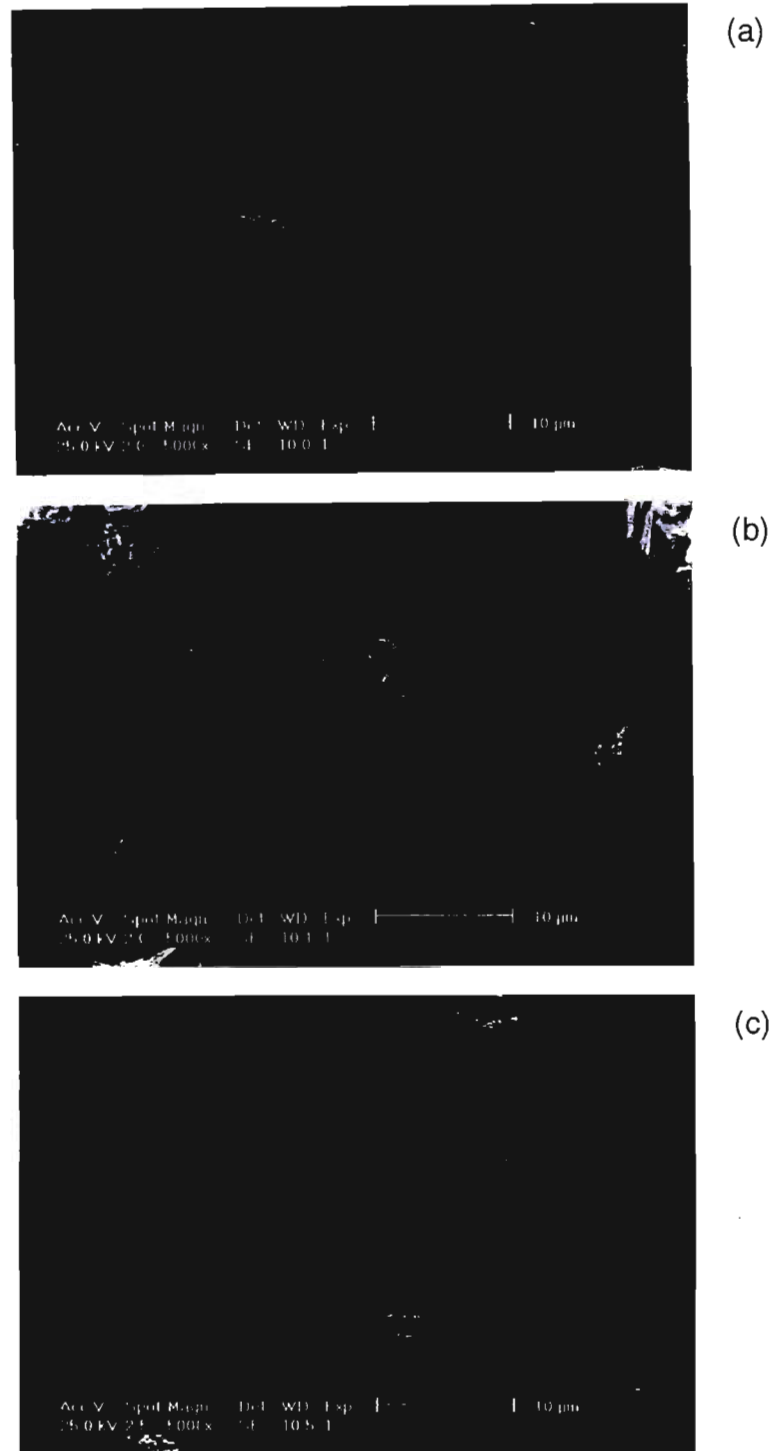


Figure 2.20: SEM photographs of binary coprecipitated oxalates of Fe and Ni in the ratios of (a) Fe₃:Ni₁, (b) Fe₁:Ni₁ and (c) Fe₁:Ni₃ pyrolysed under N₂ atmosphere at 390°C for 1 hour

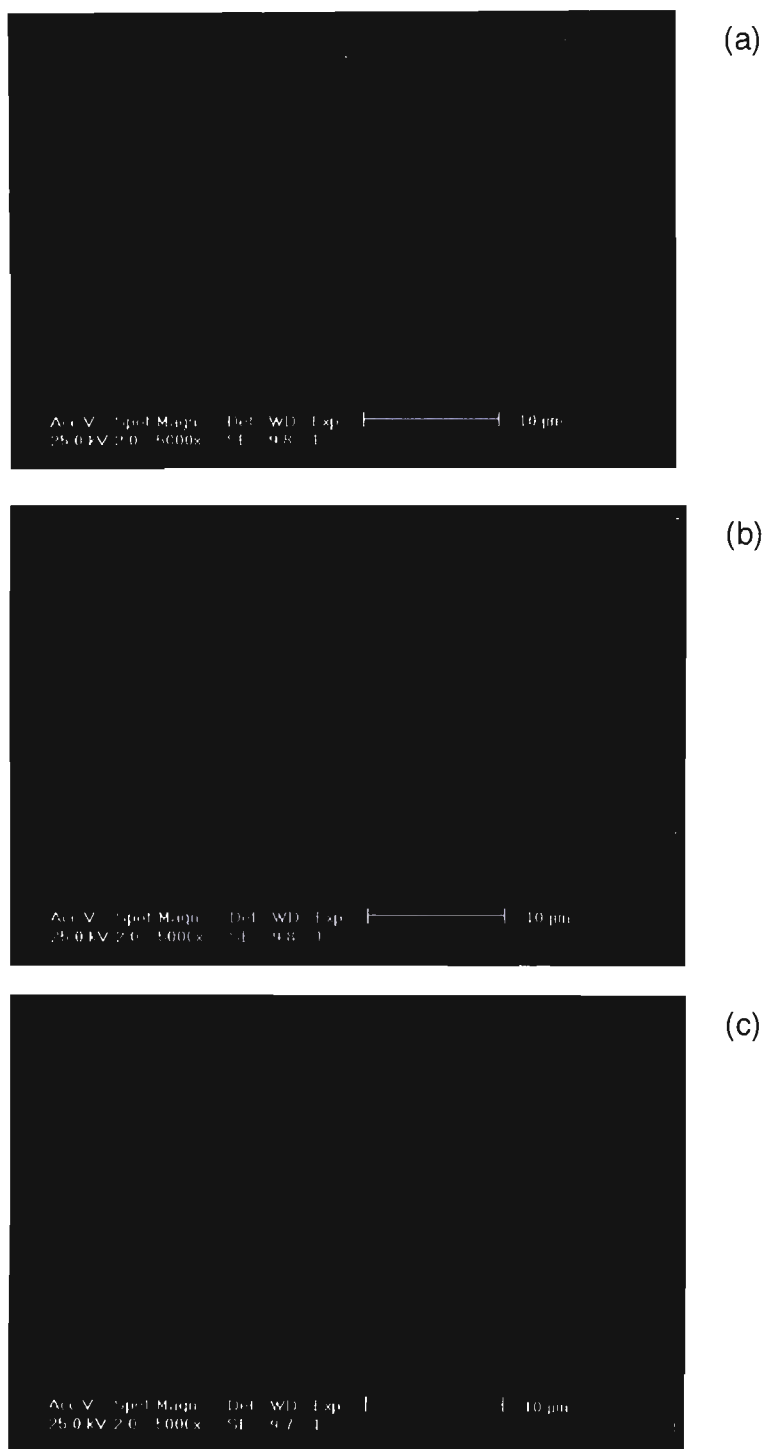


Figure 2.21: SEM photographs of binary coprecipitated oxalates of Co and Ni in the ratios of (a) Co₃:Ni₁, (b) Co₁:Ni₁ and (c) Co₁:Ni₃ pyrolysed under N₂ atmosphere at 390°C for 1 hour

2.5 SYNTHESIS AND CHARACTERISATION OF TERNARY OXALATES

The next step after the synthesis and study of the binary oxalate solid solutions was to attempt to synthesise ternary oxalate solid solutions and to investigate their pyrolysis reaction products. It was expected that since the ionic radii of the three bivalent metals under investigation are so similar, solid solutions would be formed throughout the full percentage range of molar ratios. The radii of the bivalent transition metals in question are, as stated in Section 1.1.2; $r(\text{Fe}^{2+}) = 0.76 \text{ \AA}$, $r(\text{Co}^{2+}) = 0.74 \text{ \AA}$, and $r(\text{Ni}^{2+}) = 0.72 \text{ \AA}$, respectively [95].

The method of preparation was the same as for the binary oxalates (Section 2.6), with the sulfate salts of iron, cobalt and nickel being mixed in the required molar ratio in order to form the ternary coprecipitates in the correct stoichiometry. The mole ratios used and the percentage yields are given in Table 2.18.

Table 2.18: Mole ratios and percentage yields used in the ternary coprecipitation reactions

Exp. #	$\text{FeSO}_4 \cdot 7\text{H}_2\text{O}$	$\text{CoSO}_4 \cdot 7\text{H}_2\text{O}$	$\text{NiSO}_4 \cdot 7\text{H}_2\text{O}$	% Yields
1	1	1	1	98.1
2	8	1	1	96.6
3	1	8	1	96.5
4	1	1	8	97.5

Since the percentage yields for all the ternary compounds were above 96%, it was assumed that the coprecipitates consisted of the metals in the molar ratios that were intended.

2.5.1 C and H Microanalysis

The results of the microanalysis for %C and %H (Table 2.19) are in good agreement with those calculated for the ternary coprecipitates prepared using differing ratios of the sulfate salts (Table 2.18). However, as previously noted, the microanalytical results cannot distinguish between the different metal ratios since Fe, Co and Ni have very similar atomic weights.

Table 2.19: Elemental Analysis of Coprecipitated Ternary Oxalates

Exp. #	Formula	C (%)	H (%)
1	$\text{Fe}_{0.33}\text{Co}_{0.33}\text{Ni}_{0.33}(\text{C}_2\text{O}_4)$	13.05 (13.21)	1.97 (2.22)
2	$\text{Fe}_{0.8}\text{Co}_{0.1}\text{Ni}_{0.1}(\text{C}_2\text{O}_4)$	13.38 (13.31)	1.90 (2.23)
3	$\text{Fe}_{0.1}\text{Co}_{0.8}\text{Ni}_{0.1}(\text{C}_2\text{O}_4)$	12.96 (13.16)	2.22 (2.21)
4	$\text{Fe}_{0.1}\text{Co}_{0.1}\text{Ni}_{0.8}(\text{C}_2\text{O}_4)$	13.16 (13.15)	1.95 (2.21)

The figures in parentheses are the calculated values.

As with the single and binary oxalates, all the values were within the accepted 3% error range, and can thus be said to agree with the calculated values. The number of molecules of water of crystallisation was also confirmed by the weight loss incurred on heating the sample, as determined thermogravimetrically.

2.5.2 Infrared Spectroscopy

As with the single and binary oxalates, vibrational assignments were made by comparison with values reported in the literature [40, 43-48]. Table 2.20 gives the vibrational assignments for the ternary coprecipitated oxalates in their differing molar ratios.

Table 2.20: Infrared spectra and vibrational assignments for the coprecipitated ternary oxalates in different molar ratios.

Vibrational Assignment	Experiment #			
	1 (cm ⁻¹)	2 (cm ⁻¹)	3 (cm ⁻¹)	4 (cm ⁻¹)
$\nu(\text{OH}_2)$	3365 br/s	3352 br/s	3360 br/s	3394 br/s
$\nu(\text{OH}_2)$	3130 m/sh	3130 m/sh	3144 m/sh	3110 m/sh
$\nu_{\text{as}}(\text{C}=\text{O})$	1621 br/s	1625 br/s	1619 s	1624 s
$\nu_{\text{sym}}(\text{C}-\text{O}) + \nu(\text{C}-\text{C})$	1359 m	1360 m	1360 m	1360 m
$\nu_{\text{sym}}(\text{C}-\text{O}) + \delta(\text{O}-\text{C}=\text{O})$	1314 m	1315 m	1316 m	1316 m
$\nu(\text{O}-\text{M}-\text{O})$	824 m	822 m	825 m	830 m
$\delta(\text{O}-\text{C}=\text{O}) + \nu(\text{M}-\text{O})$	743 m	736 m	755 m	754 m
$\nu(\text{O}-\text{M}-\text{O})$	587 m	545 m	561 m	592 m
$\nu(\text{M}-\text{O}) + \nu(\text{C}-\text{C})$	490 m	492 m	493 m	489 m

*br (broad); sh (shoulder); s (strong); m (medium); w (weak)

As expected the features assigned to the waters of crystallisation, at 3360 and 3130 cm⁻¹ are same as those reported for the single and binary oxalate systems (Tables 2.2, 2.7, A1 and A2). The C-O stretching frequencies for the bonded oxalate ion at 1620, 1360 and 1316 cm⁻¹ are as also the same as for the other oxalates.

Where discrepancies could arise would be in the way the metal ions bond to the oxalate ion (Section 2.1). The IR spectra of the ternary coprecipitated oxalates show that the mode of bonding of the metal ions to the oxalate ion is very similar in all four compounds. This mode of bonding is similar to that found in the single oxalates of cobalt and nickel (Table 2.1), with stretching frequencies at ca. 825, 750, 560 and 490 cm⁻¹. The stretching frequencies at 587, 545, 561 and 592 cm⁻¹ assigned to $\nu(\text{O}-\text{M}-\text{O})$ for compounds 1-4, respectively, show a slight shift towards higher wavelengths with an increase in the nickel ion concentration. The tendency for the coprecipitated compounds to take on a crystal structure isomorphous with that of the cobalt and nickel oxalates is confirmed by the XRD results (see below).

2.5.3 Particle Size Analysis and SEM

As with the single and binary oxalates, the mean particle sizes of the ternary oxalates were established using the Malvern Particle Sizer (Table 2.21). Their morphologies can be seen in the SEM photographs (Figure 2.22), and they displayed no particles corresponding in morphology to those of the parent single oxalates, thereby indicating the formation of the solid solutions.

Table 2.21: Mean particle size of coprecipitated ternary oxalates

Exp. #	Compound	Mean Particle Size
(1)	Fe1:Co1:Ni1	10.14 μm
(2)	Fe8:Co1:Ni1	16.24 μm
(3)	Fe1:Co8:Ni1	11.06 μm
(4)	Fe1:Co1:Ni8	6.16 μm

In the photograph of the equimolar precipitate, [Figure 2.22(1)], tetrahedral particles are evident; a morphology entirely distinct from that of the parent, single oxalates. The crystal forms of the other coprecipitated oxalates are also distinct, but appear to have a bias towards the morphology of the single oxalate present in the mole ratio of 80%. Thus, the coprecipitate of Fe8:Co1:Ni1 [Figure 2.22(2)], contained small, uniform, block-like particles of about 5-10 μm in diameter, as well as a few fragments. These crystals tended to form clusters and aggregates, which accounts for the mean particle size of 16.24 μm measured for this coprecipitate (Table 2.22). Similarly, the coprecipitate of Fe1:Co8:Ni1 [Figure 2.22(3)], contained needle-like particles of the order of 12 μm in length and 1 μm in width. The coprecipitate with 80% nickel [Figure 2.22(4)] showed small block-like particles (about 6 μm in length and 2.5 μm in width) together with rounded fragments.

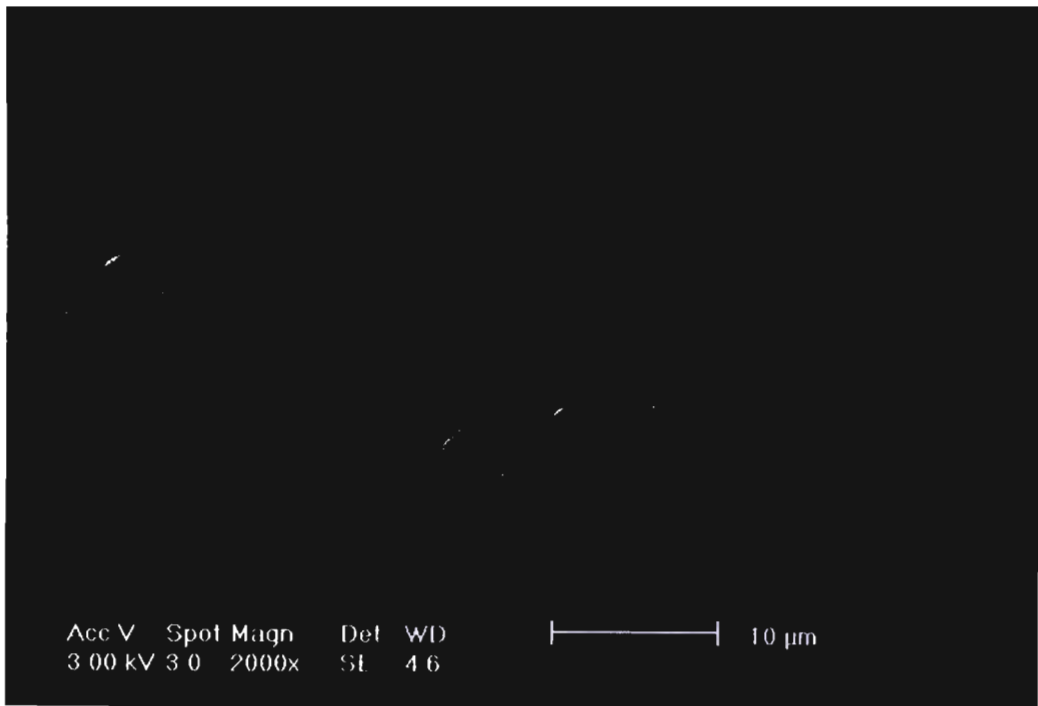
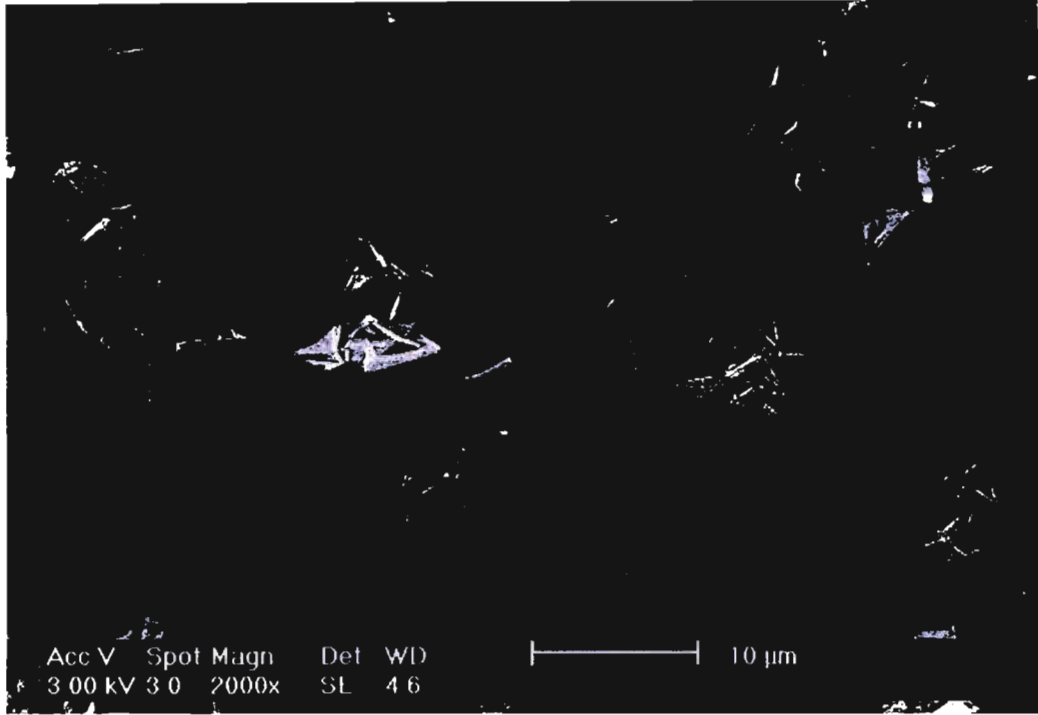


Figure 2.22: SEM photographs of ternary coprecipitated oxalates of Fe, Co and Ni in the ratios of (1) Fe1:Co1:Ni1 and (2) Fe8:Co1:Ni1

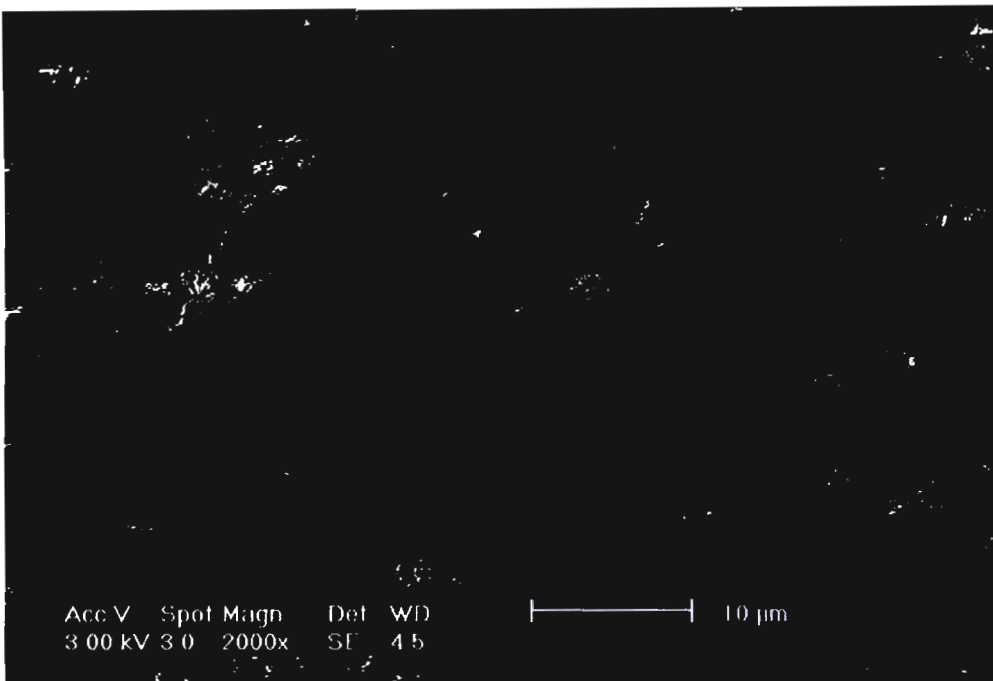
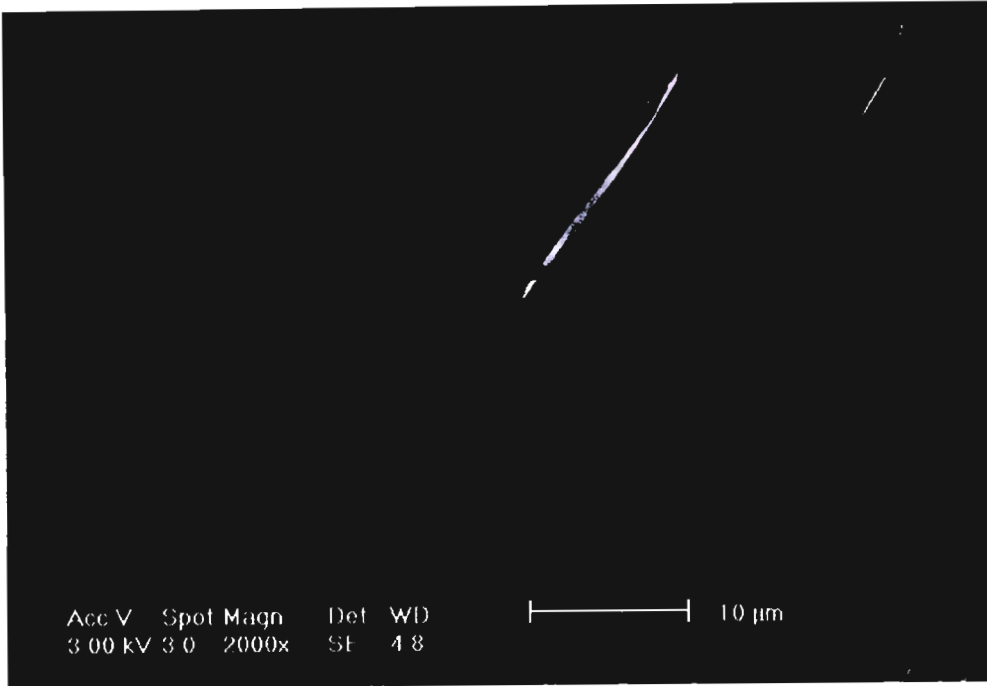


Figure 2.22 cont.: SEM photographs of ternary coprecipitated oxalates of Fe, Co and Ni in the ratios of (3) Fe₁:Co₈:Ni₁ and (4) Fe₁:Co₁:Ni₈

If these photographs of the coprecipitated oxalates are contrasted with a photograph (Figure 2.23) of the single oxalates simply mixed in the same proportions as that of the equimolar coprecipitated sample, [Figure 2.22(1)], the difference is very clear. The three typical morphologies of the single oxalates are clearly visible, in contrast to the unique morphology of a genuine solid solution. Thus these results confirmed the formation of solid solutions and, as such, are compatible with the data obtained from XRD (see below).

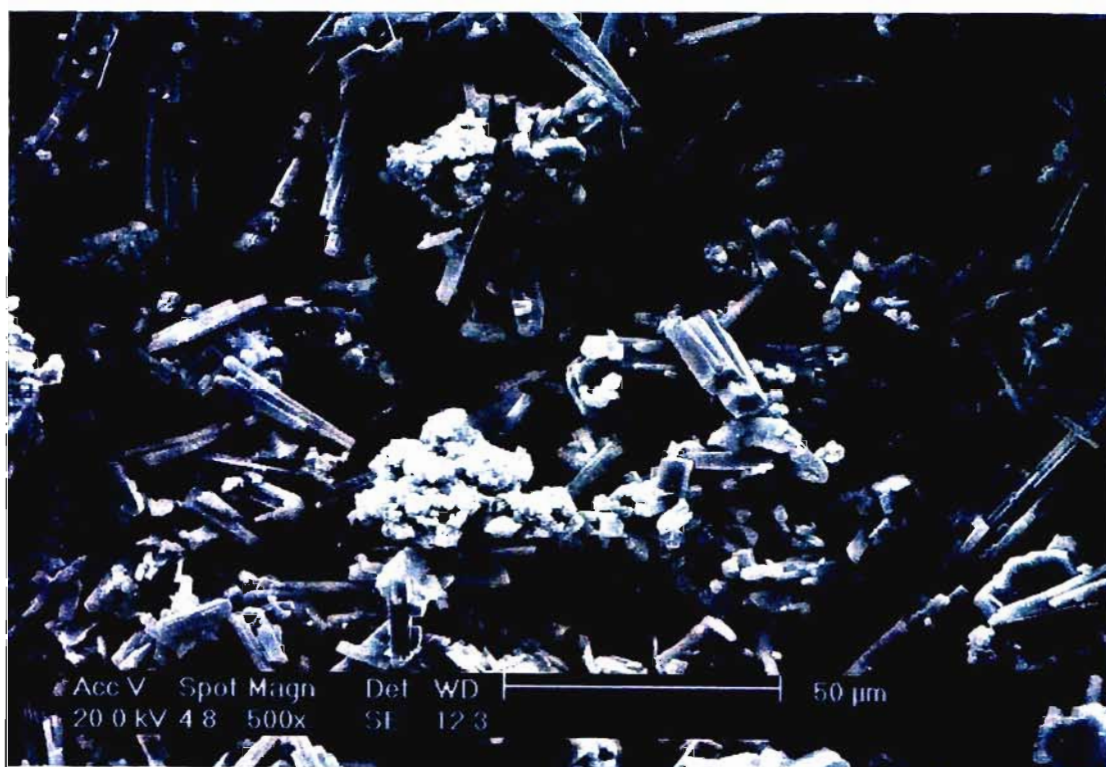


Figure 2.23 SEM photograph of the equimolar mixture of iron(II), cobalt and nickel oxalates

2.5.4 XRD

Figure 2.24 shows a comparison of the diffraction patterns of the coprecipitated oxalates in varying ratios with those of their corresponding physical mixtures. All the traces labelled 'a' are the coprecipitated products, while those labelled 'b' are the mechanical mixtures. The numbers 1-4 associated with each trace indicate the experiment numbers labelled according to the molar ratios of metal sulfates used to prepare the mixture (see Table 2.18).

These patterns appear very similar; but the peaks at 21.9 and $35.2^\circ 2\theta$ show differences which allow conclusions to be drawn. These peaks are invariably symmetrical for the coprecipitated samples. This means that the peaks are single peaks and not the result of overlap of several peaks. On the other hand, the peaks tend to be asymmetrical for the mechanical mixtures. This is due to overlap of peaks derived from the three single oxalates. In fact, in the case of samples 1 and 2 these peaks are actually split in the XRD traces of the mechanical mixtures. It may therefore be concluded that the coprecipitates are genuine substitutional solid solutions, each with a unique set of unit cell dimensions.

In Figure 2.24 (b) the physical mixtures of the three oxalates are shown in differing ratios of Fe:Co:Ni, namely (1) 1:1:1, (2) 8:1:1, (3) 1:8:1 and (4) 1:1:8 respectively. All the patterns are similar, but on closer scrutiny several differences become evident.

The differences are due mainly to the percentage of ferrous oxalate in the mixture. The patterns are differentiated by the relative heights and extent of splitting of the peaks at 22.5 and $34.9^\circ 2\theta$. It can be seen in Figure 2.2 that cobalt oxalate dihydrate has a peak at $35.23^\circ 2\theta$, nickel oxalate dihydrate $35.42^\circ 2\theta$ and ferrous oxalate dihydrate at $34.74^\circ 2\theta$. These three peaks overlap to give the peak observed at *ca.* $34.9^\circ 2\theta$ in the XRD patterns of the physical mixtures. The peak profile is dependent on the relative contributions from the individual oxalates. For example, when the metals are present in equimolar proportions the peak is split into two 34.79° and $35.30^\circ 2\theta$ [Figure 2.24 1(b)]. For the remaining proportions the systematic change in the overall shape of the peak, was confirmed by profile analysis to be the result of overlap of peaks due to each of the three oxalates. It was concluded that physical mixing of the single oxalates did not cause any changes to their respective crystal structures.

The d -values given in Table 2.22 for the various ternary coprecipitates reflect shifts in the positions of the lines due to the different proportions of the metal ions. Note that although the ionic radii of the metal ions are similar, they do differ slightly, the order of increasing size being $r(\text{Ni}^{2+})$ 0.72 \AA , $r(\text{Co}^{2+})$ 0.74 \AA and $r(\text{Fe}^{2+})$ 0.76 \AA [95].

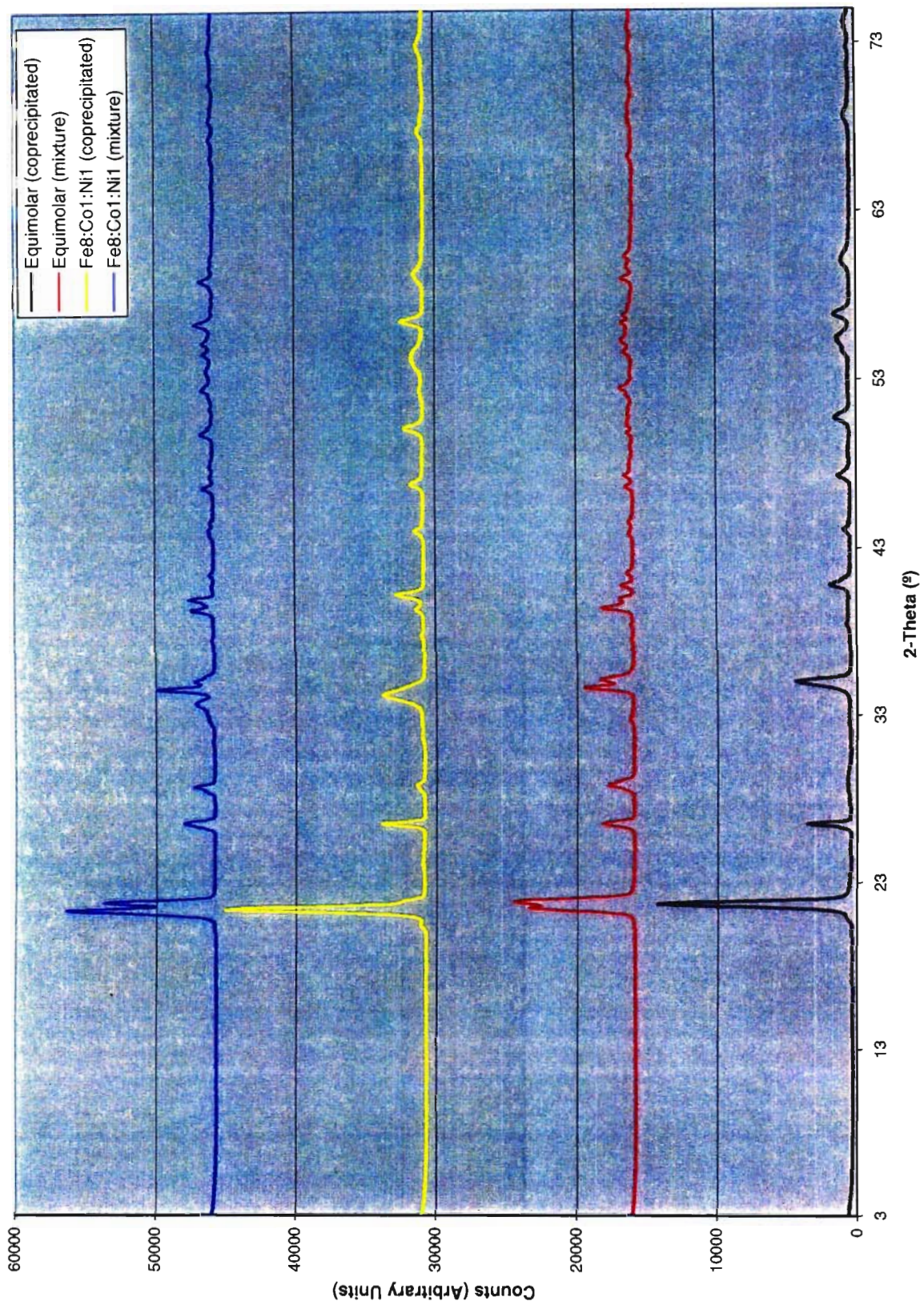


Figure 2.24: XRD patterns of ternary oxalates, coprecipitated and physical mixtures

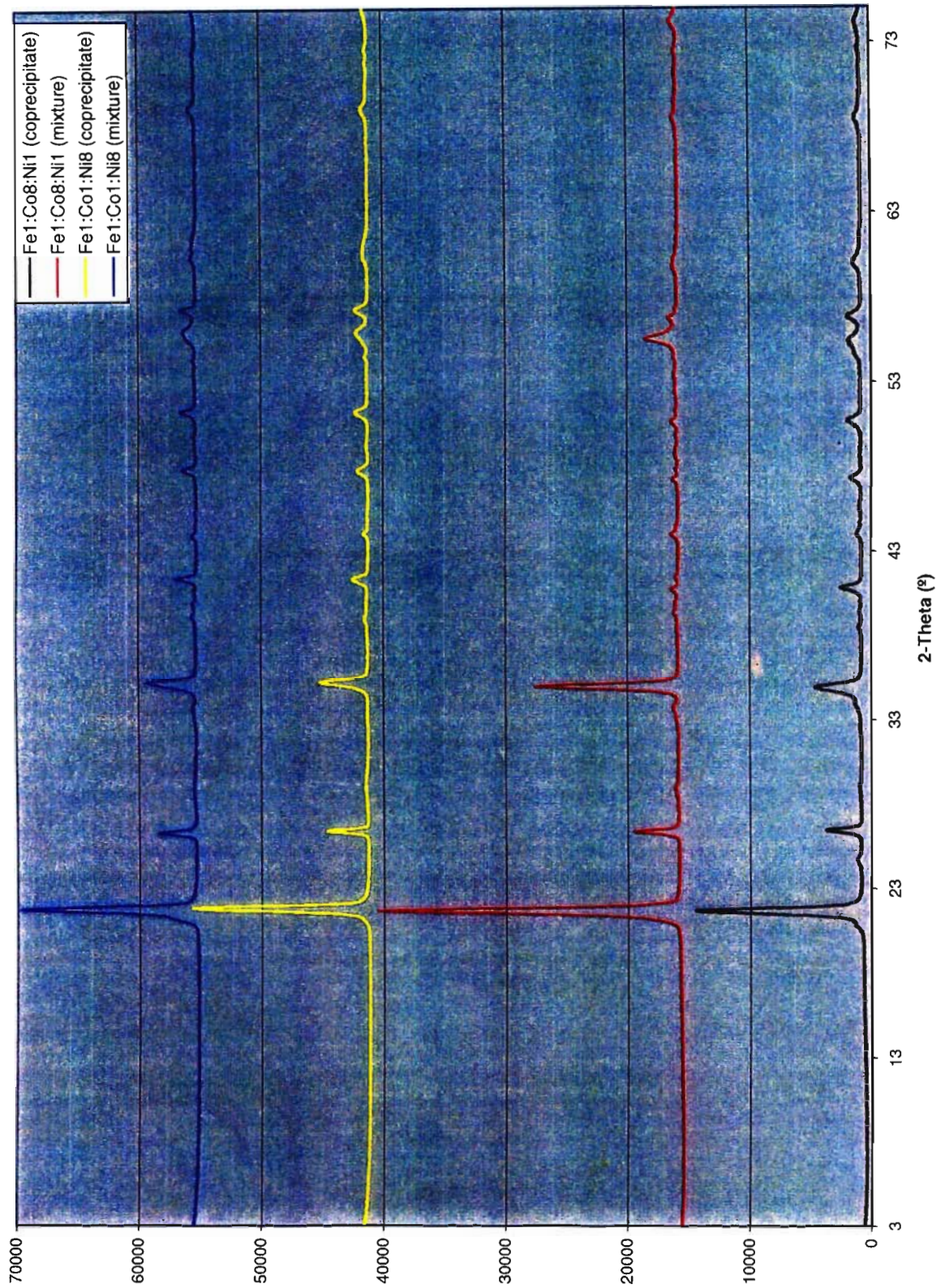


Figure 2.24 (cont.): XRD patterns of ternary oxalates, coprecipitated and physical mixtures

As the percentage of the different metal ion change in the lattice, there are shifts in the peak positions, due to changes in cell dimension. These shift is to be expected given that the coprecipitates are genuine substitutional solid solutions.

Table 2.22 Principal *d*-values (Å) for ternary coprecipitated oxalates

(1) $\text{Fe}_{0.33}\text{Co}_{0.33}\text{Ni}_{0.33}\text{C}_2\text{O}_4$	4.744	3.907	2.976	2.570	2.091	1.944	1.881
(2) $\text{Fe}_{0.8}\text{Co}_{0.1}\text{Ni}_{0.1}\text{C}_2\text{O}_4$	4.810	3.895	3.032	2.602	2.110	1.963	1.889
(3) $\text{Fe}_{0.1}\text{Co}_{0.8}\text{Ni}_{0.1}\text{C}_2\text{O}_4$	4.753	3.910	2.984	2.568	2.088	1.927	1.883
(4) $\text{Fe}_{0.1}\text{Co}_{0.1}\text{Ni}_{0.8}\text{C}_2\text{O}_4$	4.718	3.913	2.950	2.531	2.069	1.909	1.868

2.6 PYROLYSIS STUDIES OF TERNARY OXALATES

2.6.1 Thermogravimetric Analysis

The TG curves of the solid solutions (1), (2), (3) and (4) and their corresponding mixtures are shown in Figure 2.25. A nitrogen atmosphere was used with a heating rate of 5°C / min.

The TG curves of the coprecipitates were very similar to those of the single oxalates, showing a clear, well defined dehydration step followed by a single decomposition step (Figure 2.25). This is in contrast to the mechanical mixtures that showed several plateau in their TG curves, (Figure 2.25), as the three single oxalates dehydrate and decompose at their respective temperatures. This behaviour is most marked when the three single oxalates are in equimolar proportions [Figure 2.25(1)]. This agrees with the XRD data that also showed significant differences between the physical mixtures and the coprecipitates (Figure 2.24). It can thus be concluded that the coprecipitates have formed solid solutions.

As with the single oxalates, the waters of crystallisation were removed in the right stoichiometry (Table 2.23), with samples having a weight reduction of ca. 20% after dehydration for all the coprecipitates under investigation. The weight loss after decomposition suggested the formation of metals or alloys, rather than the oxides, even surprisingly for sample (2) that contained 80% ferrous ion.

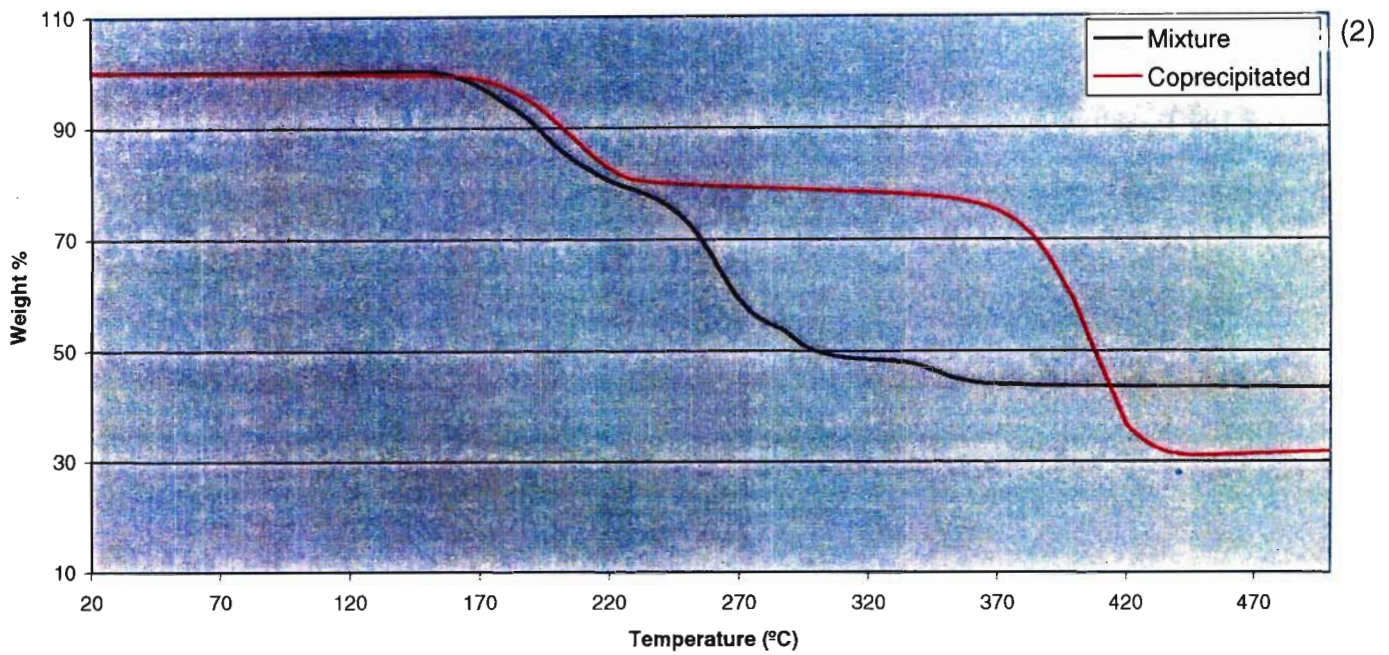
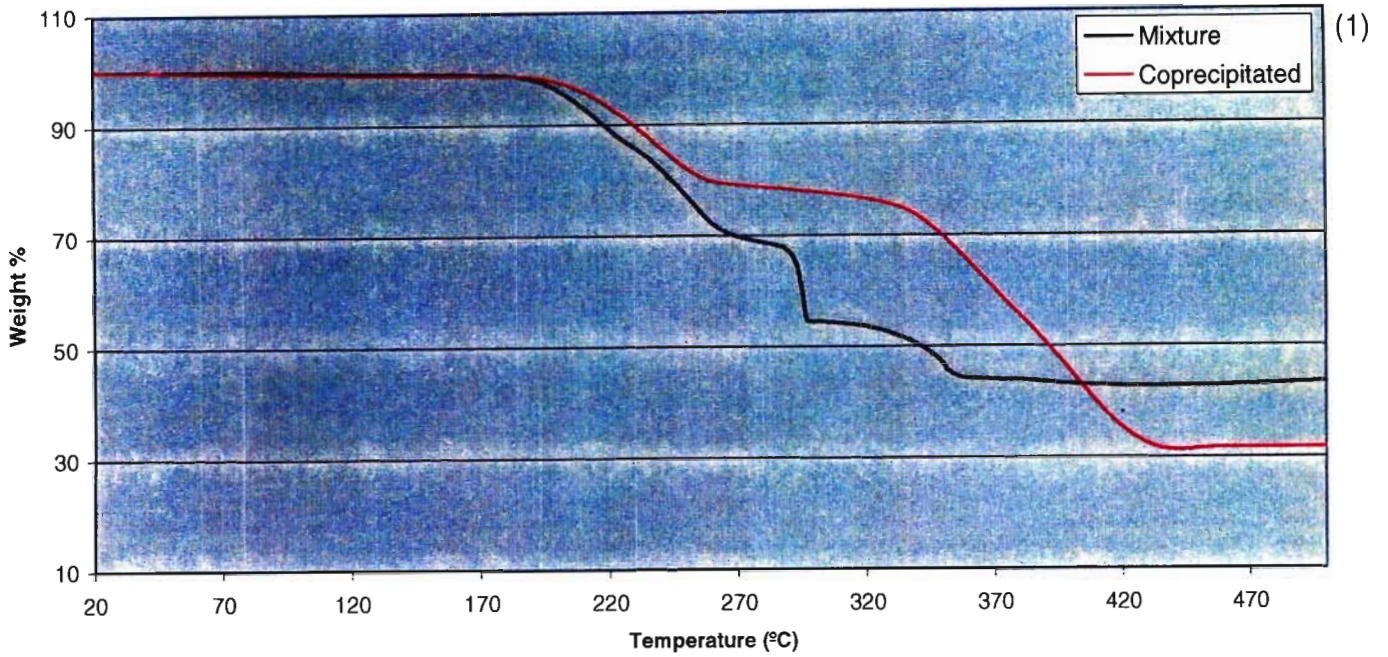


Figure 2.25: TGA traces showing a comparison between coprecipitated ternary oxalates and the corresponding mechanical mixtures. (1) Equimolar sample, (2) Fe8:Co1:Ni1

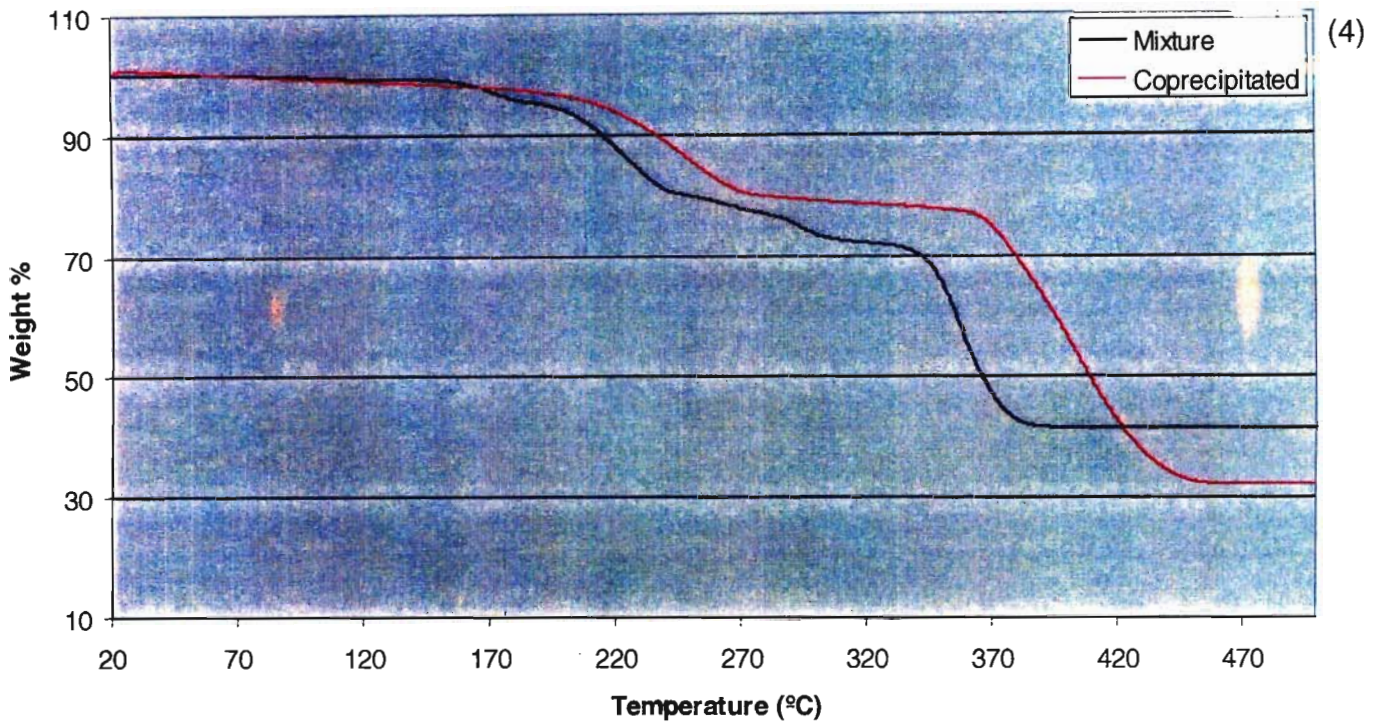
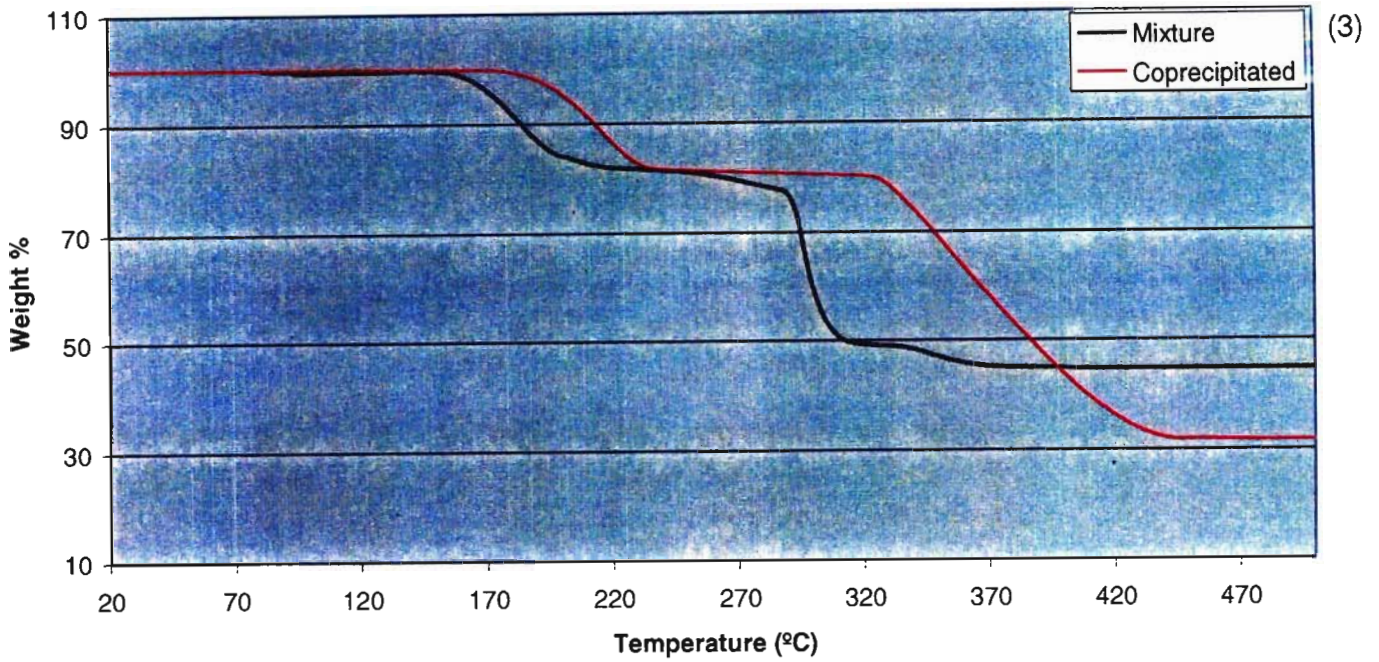


Figure 2.25 (cont.): TGA traces showing a comparison between coprecipitated ternary oxalates and the corresponding mechanical mixtures. (3) Fe1:Co8:Ni1, (4) Fe1:Co1:Ni8

This result also agrees with the XRD data that suggested that the mode of bonding in the ternary solid solutions is similar to that in the single cobalt and nickel oxalates, which decompose to form the respective metals.

The coprecipitated oxalates have unique temperatures of dehydration and decomposition, as would be expected for the solid solutions. The differences in temperatures from those recorded for the single oxalates (see Table 2.4) are probably due to lattice strain brought about by the presence of metal ions of differing size.

There was an increase in the dehydration temperature with an increase in the proportion of ions with smaller ionic radii. The temperature increased from 165°C in the compound containing mainly ferrous ion (80%) with a radius of 76 Å, to 200°C in the compound containing 80% of the nickel ion, ($r=72$ Å).

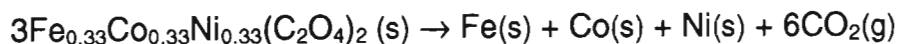
Table 2.23: Temperatures of dehydration, decomposition and weight losses for ternary coprecipitated oxalates under N_2 at ramp rate of 5°C/min

Ternary Oxalate	Dehydration (°C)	% Weight Loss	Decomposition (°C)	% Weight Loss
(1)	190	20.93 (19.81)	325	68.66 (68.21)
(2)	165	19.89 (19.96)	350	68.82 (68.73)
(3)	180	18.63 (19.73)	320	68.25 (67.92)
(4)	200	20.46 (19.74)	360	67.89 (67.98)

The figures in parentheses are the calculated values.

Compound (1), $Fe_{0.33}Co_{0.33}Ni_{0.33}(C_2O_4)_2 \cdot 2H_2O$, showed a well defined dehydration step at 190°C with a weight loss of 20.93%. This weight loss is slightly higher than the calculated value of 19.81% for two moles of water, but is within the 3% error range. The dehydration step was followed by the decomposition of the compound, commencing at 325°C and ending at 450°C. The decomposition resulted in a

further mass loss of 47.73%. The mass percentage of 31.34% for the residue is closest to that calculated (31.79%) according to the following equation:



Thus the final products of the decomposition are the metals and CO_2 . The same is true for all three ternary compounds as evidenced by the data in Table 2.24.

2.6.2 Characterisation of Furnace Products

As stated in Sections 2.1.2 and 2.2.2, the thermal decomposition by TGA was done on a very small scale, with sample sizes being between 5 and 10 mg. The next step of the investigation was to scale up the size of the experiment to use samples of about 2 g in mass, and to pyrolyse them in a tube furnace, again under a nitrogen atmosphere (Chapter 4). The resultant products were then characterised by way of XRD and SEM.

2.6.2.1 XRD

In all cases the products were found to be extremely oxygen sensitive, and as such, precautions were taken to prevent contact with air (Chapter 4). Given the weight losses found by TGA, the final products of the thermal decomposition of all the coprecipitated ternary oxalate systems were expected to be the metals or their alloys. As shown below, this turned out to be the case with the complication that these metal powders tended to be pyrophoric when contact with air occurred.

As can be seen from the X-ray patterns for the pyrolysis products (Figure 2.26) obtained from the ternary oxalates with 80% cobalt and 80% nickel, the lattice is fcc i.e., characteristic of cobalt and nickel metal. The d -values are not exactly the same as a *pure* cobalt or nickel system, however. There is a change in the unit cell dimensions due to the fact that a substitutional solid solution (or alloy) has formed, comprising three metals with different radii. This shift in d values is shown in the data presented in Table 2.24.

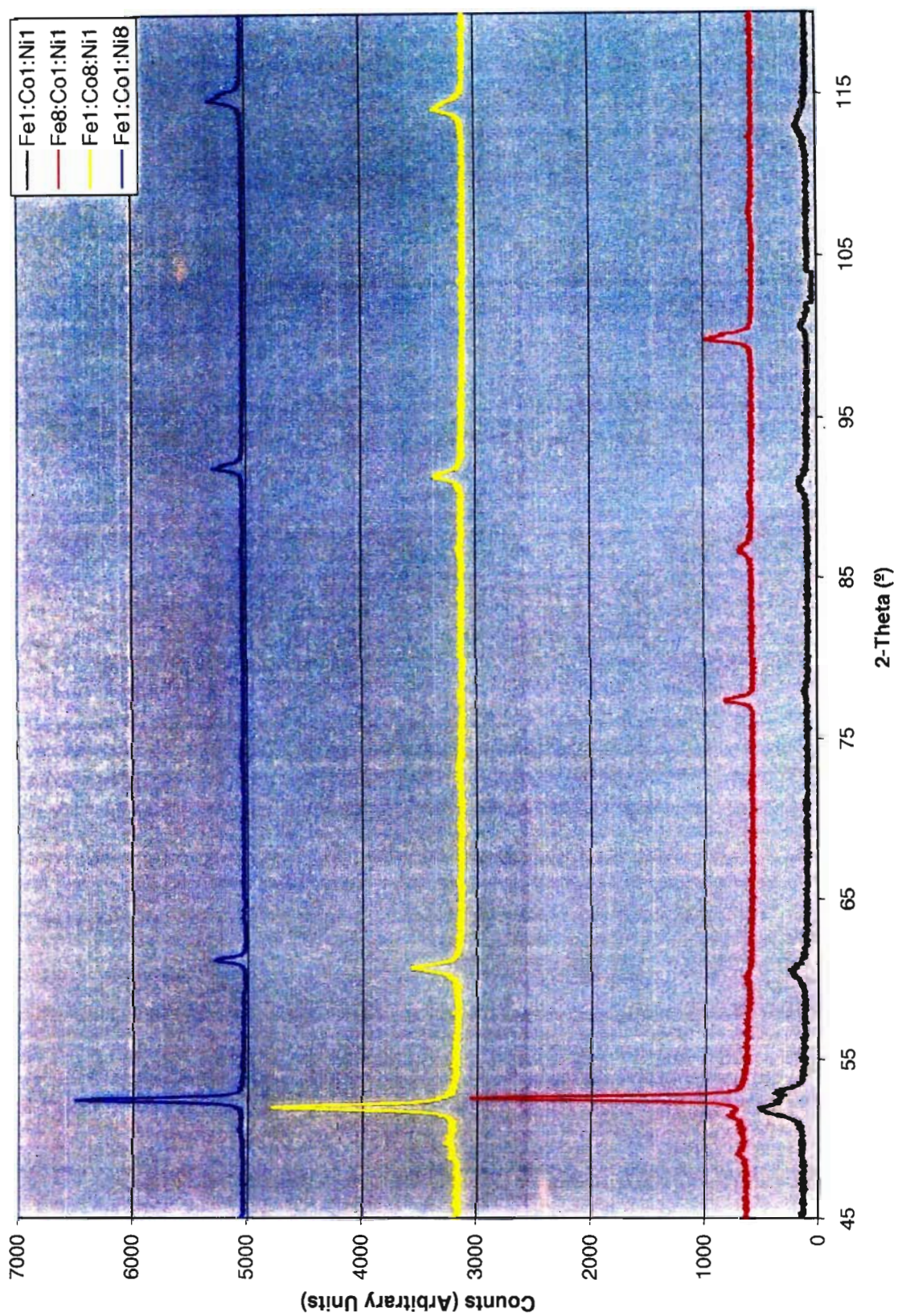


Figure 2.26: Thermal Decomposition Products of Ternary Coprecipitated Oxalates

Table 2.24: Principal d -values (Å) for the pyrolysis products of the ternary oxalate system Fe1:Co8:Ni1 and Fe1:Co1:Ni8, and those for the pure metals of cobalt and nickel [51].

Compound	hkl			
	111	200	220	311
Ni	2.034	1.762	1.246	1.062
Fe _{0.1} Co _{0.1} Ni _{0.8}	2.035	1.762	1.246	1.064
Fe _{0.1} Co _{0.8} Ni _{0.1}	2.046	1.770	1.250	1.067
Co	2.047	1.772	1.253	1.069

As anticipated the d values of the ternary alloys fall between those of the pure metals of cobalt and nickel.

The ternary compound with the highest percent of iron (experiment 2, Fe8:Co1:Ni1), gave a product with a bcc lattice characteristic of α -iron (Figure 2.26). Again there is a shift in d values from those for *pure* iron, confirming the formation of a substitutional solid solution, though this is less marked than for the fcc alloys (see Table 2.25). As with the fcc alloys, the bcc alloy has slightly lower d -values than that for pure α -iron (at least for the 110 reflection), due to the inclusion of the smaller atoms of cobalt and nickel into the crystal lattice.

Table 2.25: Principal d values (Å) for the pyrolysis product of the ternary oxalate system Fe8:Co1:Ni1 and for pure metallic iron [51].

Compound	hkl		
	110	200	211
Fe _{0.8} Co _{0.1} Ni _{0.1}	2.025	1.433	1.170
Fe	2.027	1.433	1.170

The peak at $86.46^\circ 2\theta$ (d value = 1.307 Å) (Fe8:Co1:Ni1 in Figure 2.26) is due to oxide contamination. Although stringent precautions were taken to prevent

oxidation, due to the extreme reactivity of the metal powders produced, resulted in some contamination being unavoidable.

The pyrolysis products from the equimolar system gave an XRD pattern of low intensity, possibly due to small crystallite size. However, the pattern still clearly shows a mixture of phases. Predominant is the fcc phase with peaks at 52.86, 60.88, 90.90 and 113.04° 2 θ (d values = 2.048, 1.767, 1.257 and 1.074 Å, respectively). This pattern is overlaid with the pattern of a less intense bcc phase, with peaks at 52.90, 78.38 and 101.08 2 θ (d values = 2.010, 1.417 and 1.160 Å, respectively). This could mean that a homogenous alloy has not formed, but rather an intimate mixture of the pure metals of iron, cobalt and nickel. This would account for the increased intensity of the lines for the fcc phase, as both cobalt and nickel have very similar patterns. Mixing is achieved that is superior to that obtained from any mechanical mixing method.

2.6.2.2 SEM

In all four of the SEM photographs of the thermal decomposition products shown in Figure 2.27, fissures and cracks, caused by the loss of H₂O and CO₂, can be clearly seen. As with the single and binary oxalate pyrolysis products, there was no dramatic change in the size or shape of the crystals in comparison to those of the starting material. This would suggest that considerable lattice strain exists in these materials, given the ~70% mass loss, with no corresponding loss in volume.

2.7 MORPHOLOGY VARIANCE

As discussed in Section 2.1, the needle morphology of the cobalt oxalate, and cobalt containing binary and ternary oxalates, is the least desirable for packing and mixing. Langbein and Fischer [94] determined that grain size distribution was strongly influenced by reaction conditions during the precipitation process. Thus an attempt was made to try and modify the morphology of first the cobalt oxalate dihydrate, and, secondly, the equimolar cobalt ferrous coprecipitated oxalate, in order to improve their packing and mixing ability.

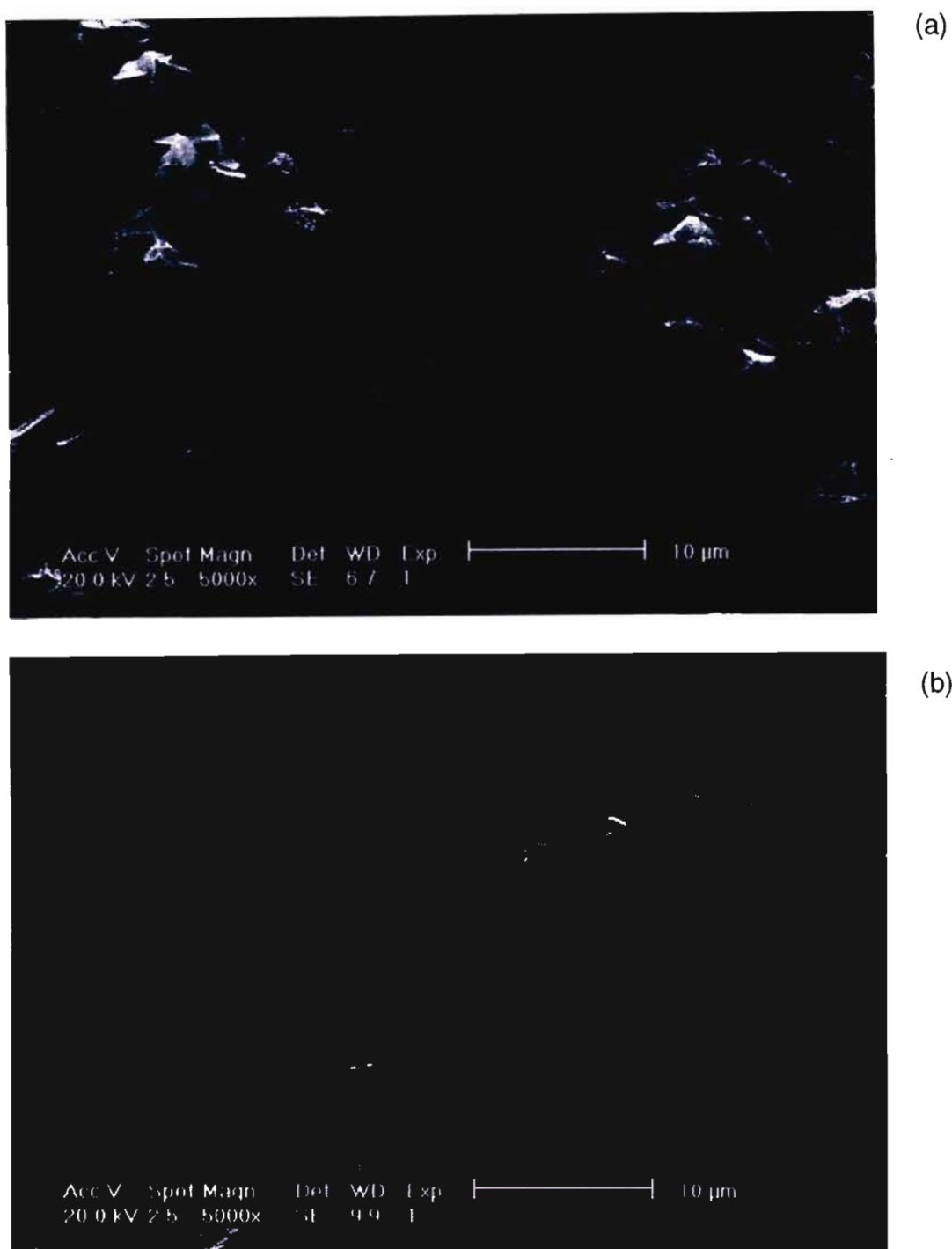


Figure 2.27: SEM photographs of ternary coprecipitated oxalates of Fe, Co and Ni in the ratios of (a) Fe1:Co1:Ni1 and (b) Fe8:Co1:Ni1 pyrolysed under N₂ atmosphere at 390°C for 1 hour

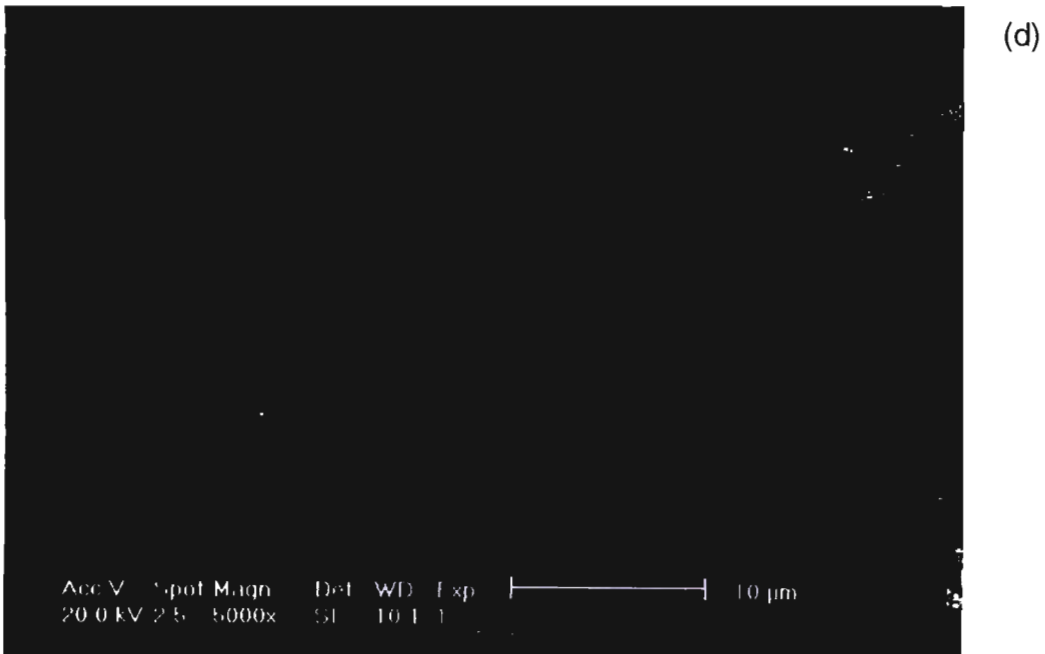
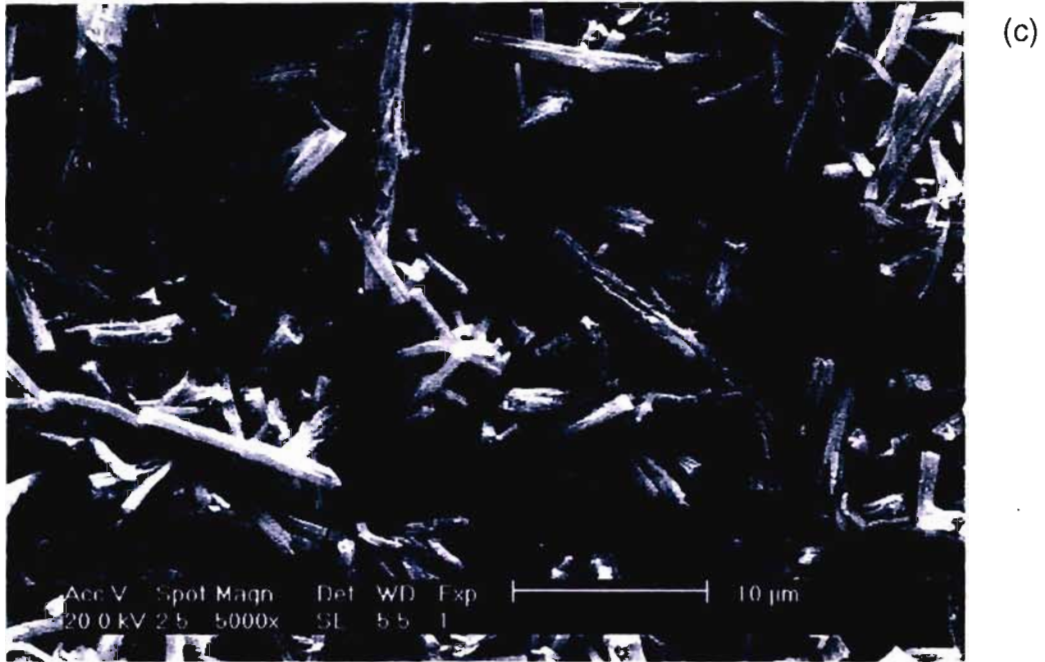


Figure 2.27: SEM photographs of ternary coprecipitated oxalates of Fe, Co and Ni in the ratios of (c) Fe1:Co8:Ni1 and (d) Fe1:Co1:Ni8 pyrolysed under N₂ atmosphere at 390°C for 1 hour

2.7.1 Synthesis and Characterisation of Cobalt Oxalate Dihydrate

The method of synthesis was changed in order to try and change the morphology of the cobalt oxalate powder. The changes to the original synthesis method (Section 4.2) included raising the temperature from 60 to 90°C and increasing the rate at which the sulfate salt was added to the oxalic acid solution. The latter was achieved by adding the salt over a period of one rather than twenty hours. These changes were introduced to speed up the rate at which the cobalt oxalate precipitated and so disrupt the growing of the needles.

The C and H microanalysis for the modified cobalt oxalate was the same as for the original (Table 2.1) as was the IR spectra (Table 2.2). The two compounds, however, differed in their particle sizes (Table 2.26).

Table 2.26: Mean particle size of the original cobalt oxalate dehydrate (1) and the modified form (2).

Compound	Mean Particle Size
(1) $\text{CoC}_2\text{O}_4 \cdot 2\text{H}_2\text{O}$	10.18 μm
(2) $\text{CoC}_2\text{O}_4 \cdot 2\text{H}_2\text{O}$	3.61 μm

As can be seen from the results of the Malvern particle size analysis (Table 2.27.), the mean particle size of the modified cobalt oxalate has decreased significantly. The particle size data are also more unimodal (Figure 2.28), suggesting that a more uniform product has been formed. The narrower distribution of values obtained for the modified cobalt oxalate also shows that the particles are more "spherical".

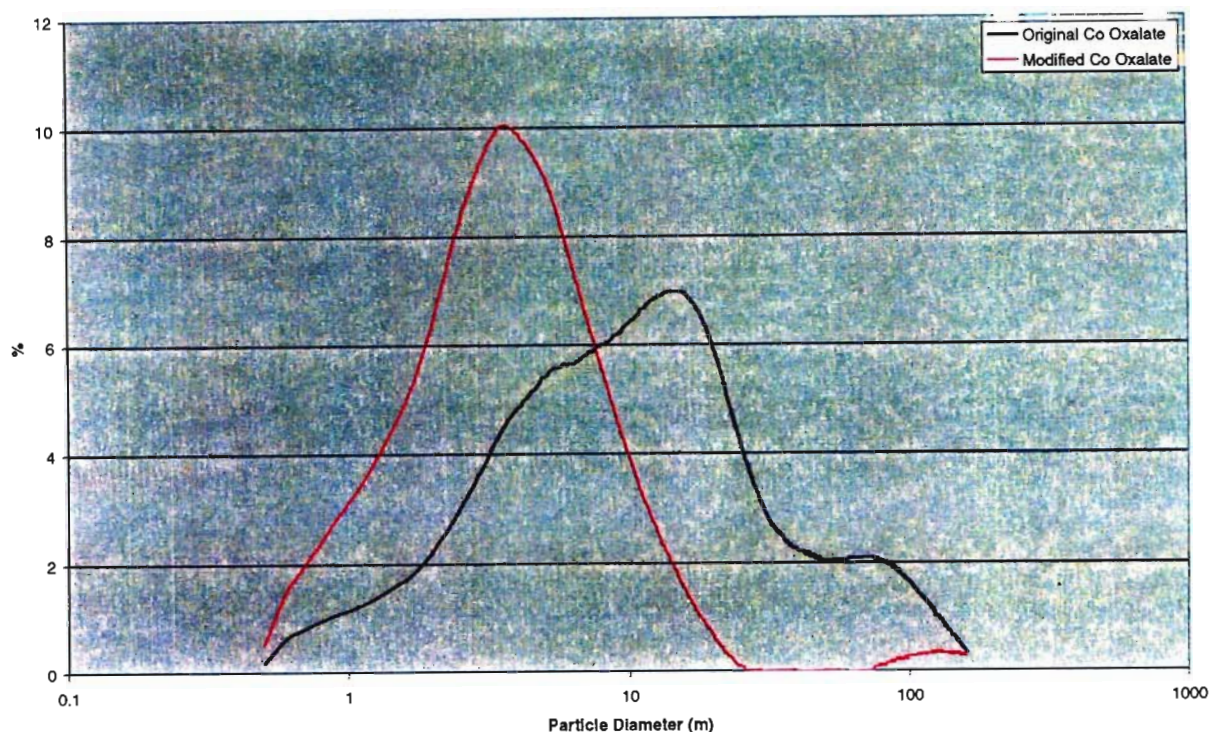


Figure 2.28: Malvern particle size distribution of original $\text{CoC}_2\text{O}_4 \cdot 2\text{H}_2\text{O}$ and modified $\text{CoC}_2\text{O}_4 \cdot 2\text{H}_2\text{O}$ (μm)

When looking at the SEM photograph of the modified cobalt oxalate (Figure 2.29(2)), it becomes apparent why there was such a decrease in the mean particle size, as well as in the spread of data. Small crystal fragments have replaced the original needles. The majority of the crystals are almost spherical with a diameter of about $3.5 \mu\text{m}$. Fissures can be seen in the crystals. This was presumably due to the extreme conditions during precipitation.

X-ray diffraction patterns of the modified $\text{CoC}_2\text{O}_4 \cdot 2\text{H}_2\text{O}$ in comparison to the original $\text{CoC}_2\text{O}_4 \cdot 2\text{H}_2\text{O}$ (Figure 2.30), show that although the pattern is the same for both compounds, indicating that they do indeed have the same crystal structure, the intensity of the peaks differ greatly. In the XRD pattern of the modified $\text{CoC}_2\text{O}_4 \cdot 2\text{H}_2\text{O}$, the peaks are both much less intense, and more diffuse. This could be due to poorer crystallinity or a lower long range order induced by the modified experimental. The smaller crystallite size of the modified cobalt oxalate also seemed to have another effect in that it decomposed at a lower temperature than the original sample. The original sample dehydrated at 175°C whereas the modified cobalt oxalate dehydrated at 162°C .

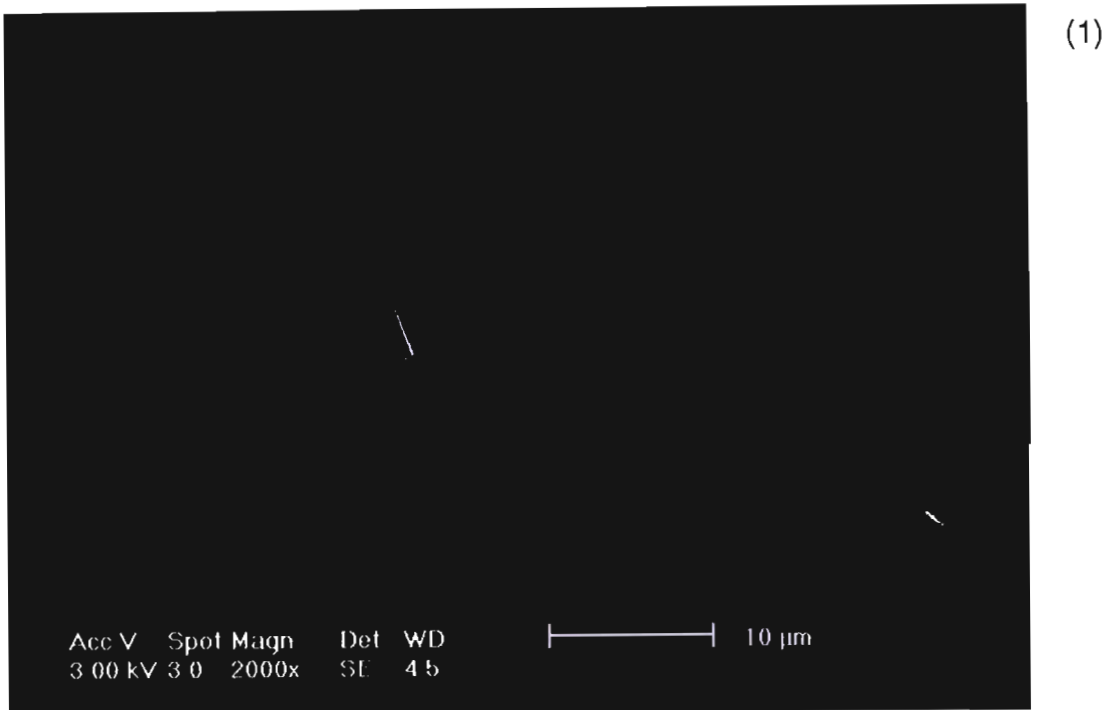


Figure 2.29: SEM photographs showing the crystal morphologies of the two different methods of preparation of cobalt oxalate dihydrate. (1) conventional treatment, (2) modified treatment

Although this difference in dehydration temperature of 13°C is significant, it is relatively small compared to the difference in the temperatures at which decomposition was initiated. For the original cobalt oxalate (Section 2.1), this was 355°C; for the modified cobalt oxalate it was 255°C, even though the experimental conditions were kept the same (Figure 2.31.).

The rate of the onset of the reaction was also more gradual in the original sample, as compared to the modified oxalate. This observation is in accordance with results obtained by Dollimore [39], who found that the pre-treatment of the oxalate is very important to the subsequent thermal decomposition. A reason for this change could be that the larger surface area of the modified cobalt oxalate leads to an increase in the reaction rate. The increased reaction rate at a lower temperature could also be derived from the strain the crystals were subjected to in the precipitation process. As seen by the SEM [Figure 29(2)], there are many stress fractures clearly visible on the crystals. This strain put on the crystals would possibly increase the energy of the system, and enable the decomposition to take place at a lower temperature.

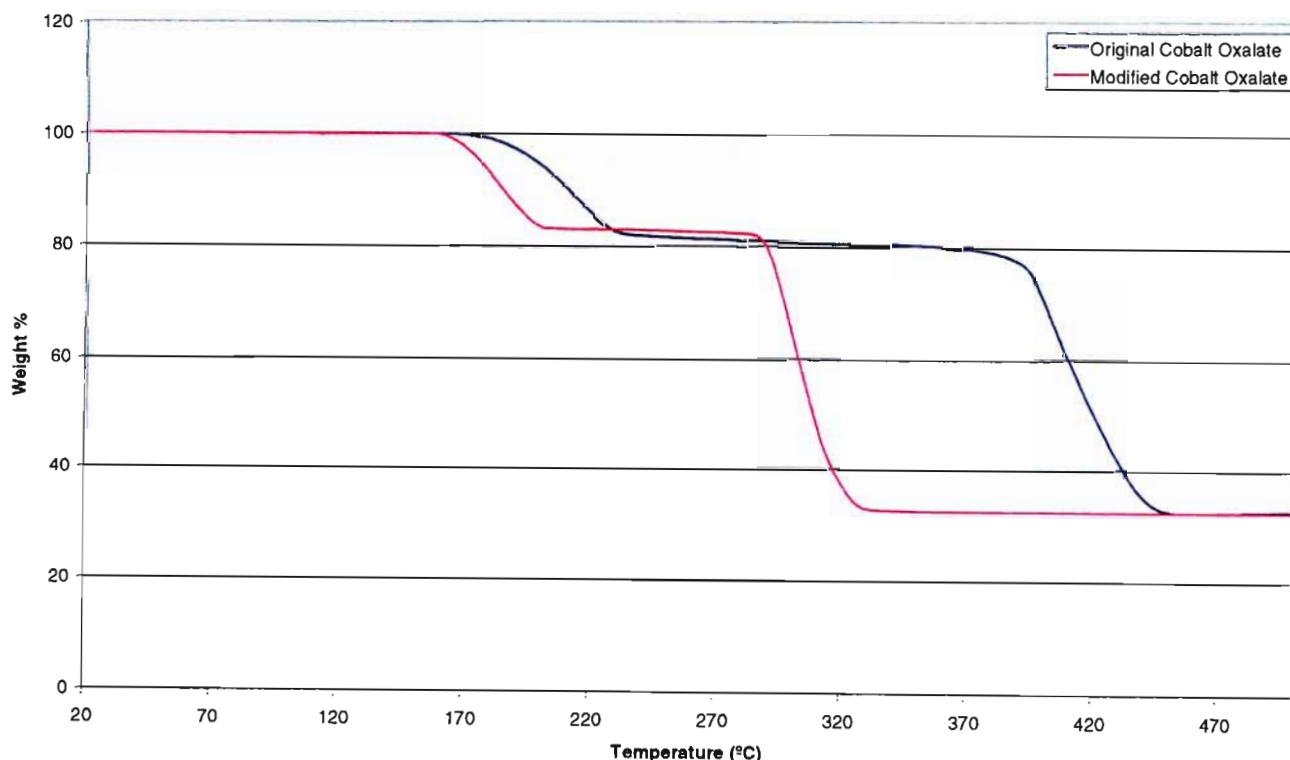


Figure 2.30: TGA curves showing comparison of two different samples of cobalt oxalate. (conditions: ramp rate of 5°C/min under N₂)

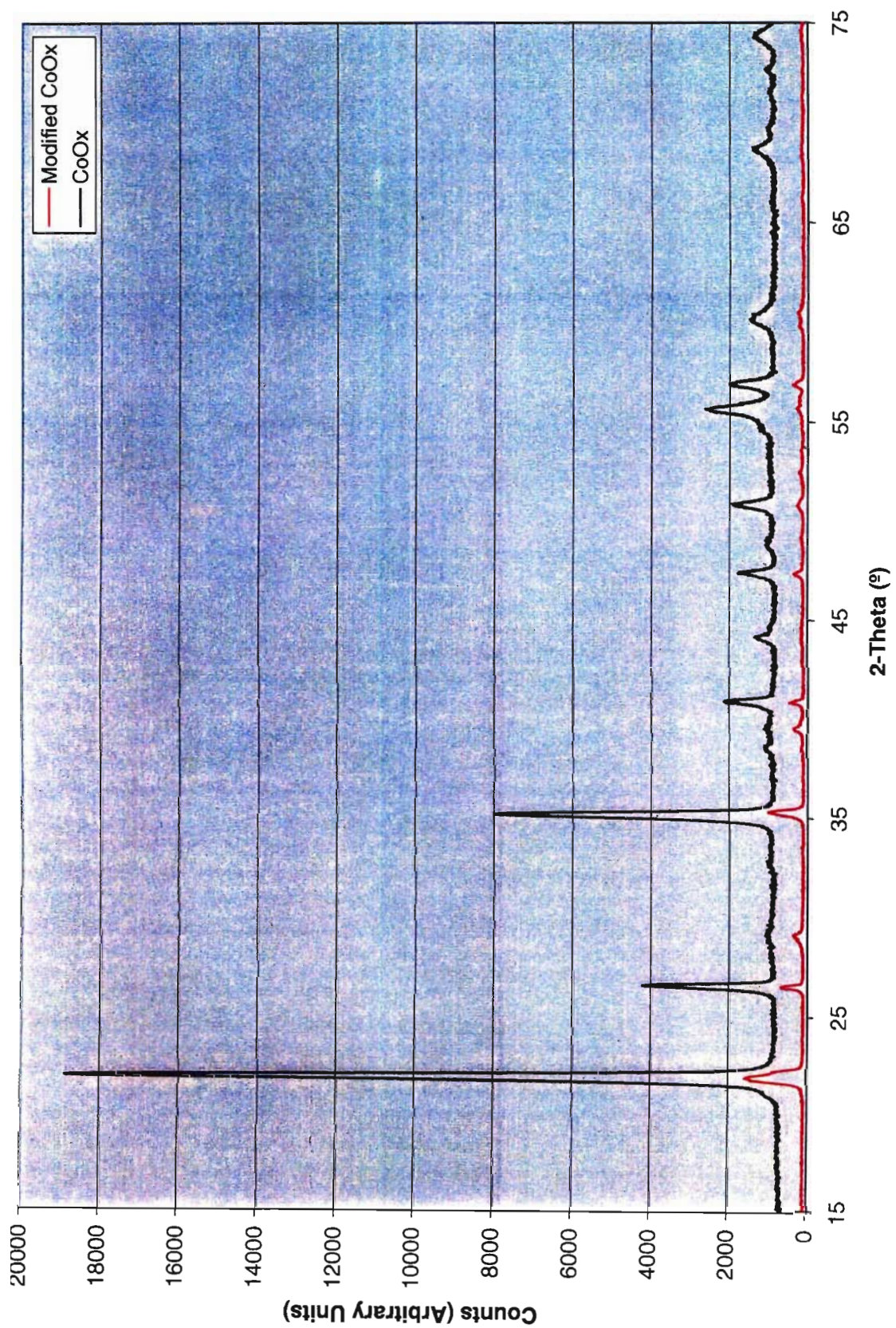


Figure 2.31: XRD comparison of differing synthetic routes of cobalt oxalate

2.7.2 Synthesis and Characterisation of Equimolar Binary Iron-Cobalt Oxalate

After modifying the morphology of $\text{CoC}_2\text{O}_4 \cdot 2\text{H}_2\text{O}$, the next step was to try to alter the morphology of the binary oxalates containing cobalt. The most problematic, with regard to morphology, was the iron-cobalt binary oxalate system (Section 2.2.). The coprecipitated compound chosen was the iron-cobalt oxalate in equimolar proportions. The synthesis procedure was modified as described in Section 2.4.1.

The C and H microanalysis was as expected for the binary iron-cobalt oxalate in the ratio of Fe1:Co1. The mean particle size decreased in the modified compound from the original 13.06 to 7.76 μm (Table 2.27). The morphology was also altered, from long needles to a block-like morphology with many smaller fragments (Figure 2.32). The modified compound looks as if it has been stressed, as many of the surfaces of the crystals are rough and not well formed. With these changes in morphology and size, the aim of the experiment appeared to have been achieved.

Table 2.27 Mean particle size of the original equimolar iron-cobalt oxalate (1) and the modified form (2).

Compound	Mean Particle Size
(1)Fe1:Co1 original	13.06 μm
(2)Fe1:Co1 modified	7.76 μm

Unfortunately it seems that as a consequence of the harsh conditions of synthesis, not only was the morphology altered, but the crystal system as well. As discussed in Section 2.2, there is not much difference in the stretching frequencies of the different oxalates, as shown by the IR data (Table 2.28).



Figure 2.32: SEM photographs showing a comparison between the (1) original and (2) modified equimolar Ferrous/Cobalt binary coprecipitated oxalates

Table 2.28: IR data comparing the two equimolar iron-cobalt binary oxalate with the single oxalates of iron(II) and cobalt(II)

Vibrational Assignment	(1) Fe1:Co1	(2) Fe1:Co1	Fe(II) Ox	Co(II) Ox
$\nu(\text{OH}_2)$	3351 br/s	3410 br/s	3339 br/s	3362 br/s
$\nu(\text{OH}_2)$	3160 m/sh	3156 m/sh	3166 m/sh	3154 m/sh
$\nu_{\text{as}}(\text{C}=\text{O})$	1620 s	1635 s	1622 s	1619 s
$\nu_{\text{sym}}(\text{C}-\text{O}) + \nu(\text{C}-\text{C})$	1360 m	1360 m	1361 m	1360 m
$\nu_{\text{sym}}(\text{C}-\text{O}) + \delta(\text{O}-\text{C}=\text{O})$	1316 m	1316 m	1316 m	1316 m
$\nu(\text{O}-\text{M}-\text{O})$	820 m	824 m	822 m	825 m
$\delta(\text{O}-\text{C}=\text{O}) + \nu(\text{M}-\text{O})$	769 m	780 m	765 m	746 m
$\nu(\text{O}-\text{M}-\text{O})$	739 m	735 m	722 m	607 m
$\nu(\text{M}-\text{O}) + \nu(\text{C}-\text{C})$	496 m	495 m	493 m	493 m

*br (broad); sh (shoulder); s (strong); m (medium); w (weak)

The XRD patterns give a clearer picture (Figure 2.33). The original compound (1) appears to be isomorphous with that of cobalt oxalate. This is clearly evident when comparing the XRD patterns of cobalt oxalate and that of the original Fe1:Co1 binary oxalate. As stated in Section 2.1, the crystal system is that of a centred monoclinic crystal and is designated the α -form. The peak at $21.70^\circ 2\theta$ (Figure 2.33) in the original binary compound, is shifted slightly compared to the peak at $21.88^\circ 2\theta$ for the pure cobalt oxalate dihydrate. This is due to the change in unit cell size with the inclusion of the Fe^{2+} ion.

The modified binary oxalate (2) turned out to have a crystal structure analogous to that of the ferrous oxalate dihydrate. This time there is a slight increase in degrees 2θ of the corresponding peaks due to the smaller unit cell size of the binary compound, with the inclusion of the cobalt ion. This accounts for the shift of the primary peaks of iron oxalate at 21.44 and $21.92^\circ 2\theta$, to 21.58 and $22.06^\circ 2\theta$ of the corresponding peaks in the binary oxalate.

In Sections 2.1 and 2.2, it was discussed that cobalt oxalate decomposes to the metal, and that the binary oxalate, when isomorphous to the cobalt oxalate, also

decomposes to the metal. The ferrous oxalate dihydrate decomposed to the oxide. It was thus postulated that the modified binary oxalate would decompose to the oxide.

The TGA data (Table 2.29), the modified binary oxalate (2) dehydrated and decomposed at higher temperatures than the original binary oxalate (1). The modified oxalate also decomposed to the oxide, rather than the metal as evidenced by the weight loss data.

Table 2.29: Temperatures of dehydration and decomposition for equimolar iron-cobalt coprecipitated oxalate systems under N_2 at a ramp rate of $5^\circ/\text{min}$

Iron-Cobalt Oxalate	Dehydration ($^\circ\text{C}$)	% Weight Loss	Decomposition ($^\circ\text{C}$)	% Weight Loss
(1) Fe1:Co1	160	19.42 (19.86)	280	68.22 (68.37)
(2) Fe1:Co1	170	20.05 (19.77)	350	62.48 (68.37)

Specifically, the original compound decomposed with a weight loss of 68.22%, corresponding to metal formation, whereas the modified compound decomposes to the metal oxide with a weight loss of only 62.48%. Decomposition of the modified binary oxalate to the oxide was expected given its isomorphism with the crystal structure of the iron oxalate dihydrate. The TGA curves are illustrated in Figure 2.34.

The conclusion was that for the oxalates it is the crystal structure (more accurately the space group) that determines the pyrolysis product. Specifically, if the binary oxalate takes on the crystal structure of pure cobalt oxalate, the product will be the metal or alloy. On the other hand, if it takes on the crystal structure of the iron oxalate it decomposes to the oxide.

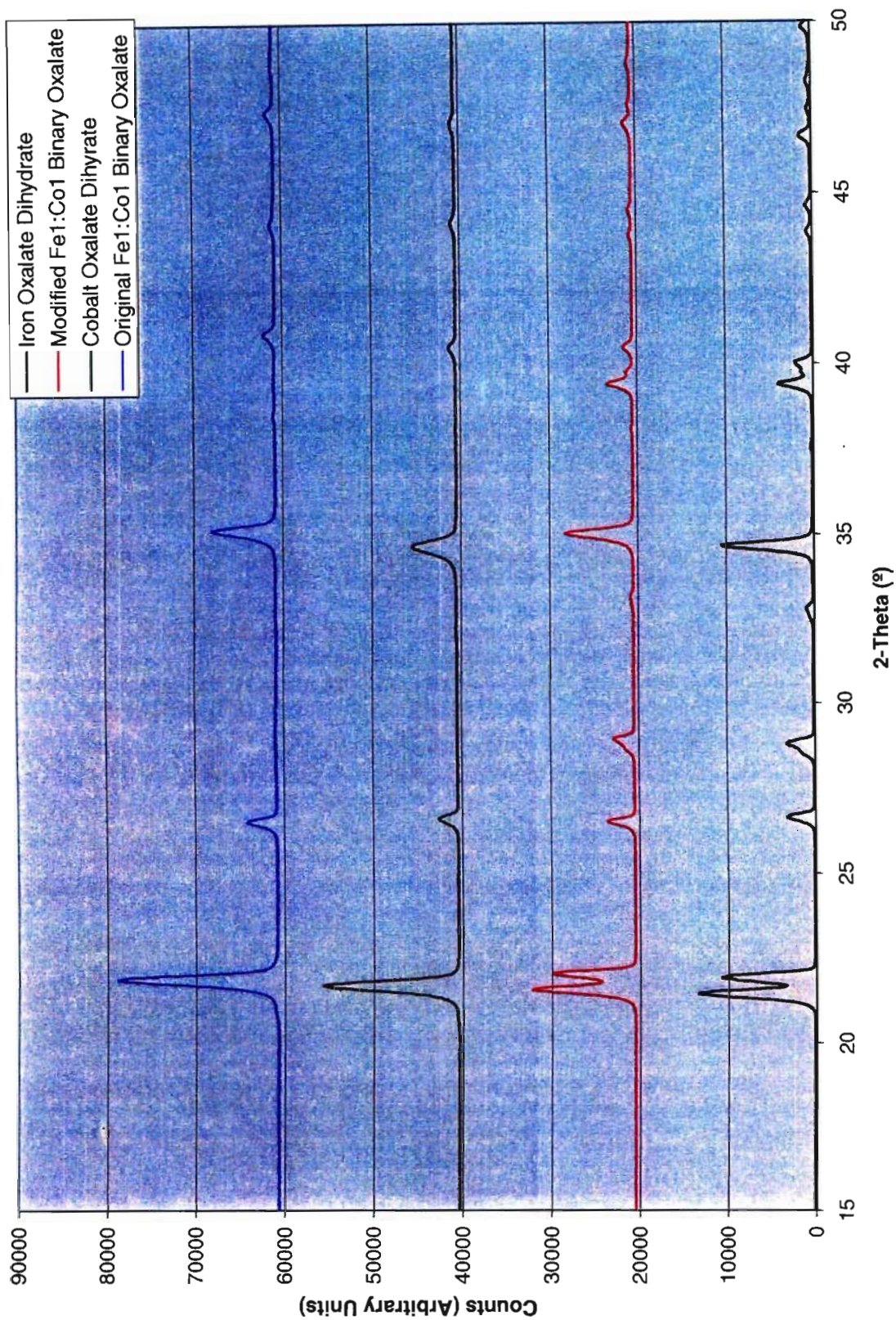


Figure 2.33: XRD patterns of the single oxalates of iron and cobalt with the different preparations of binary oxalate Fe1:Co1

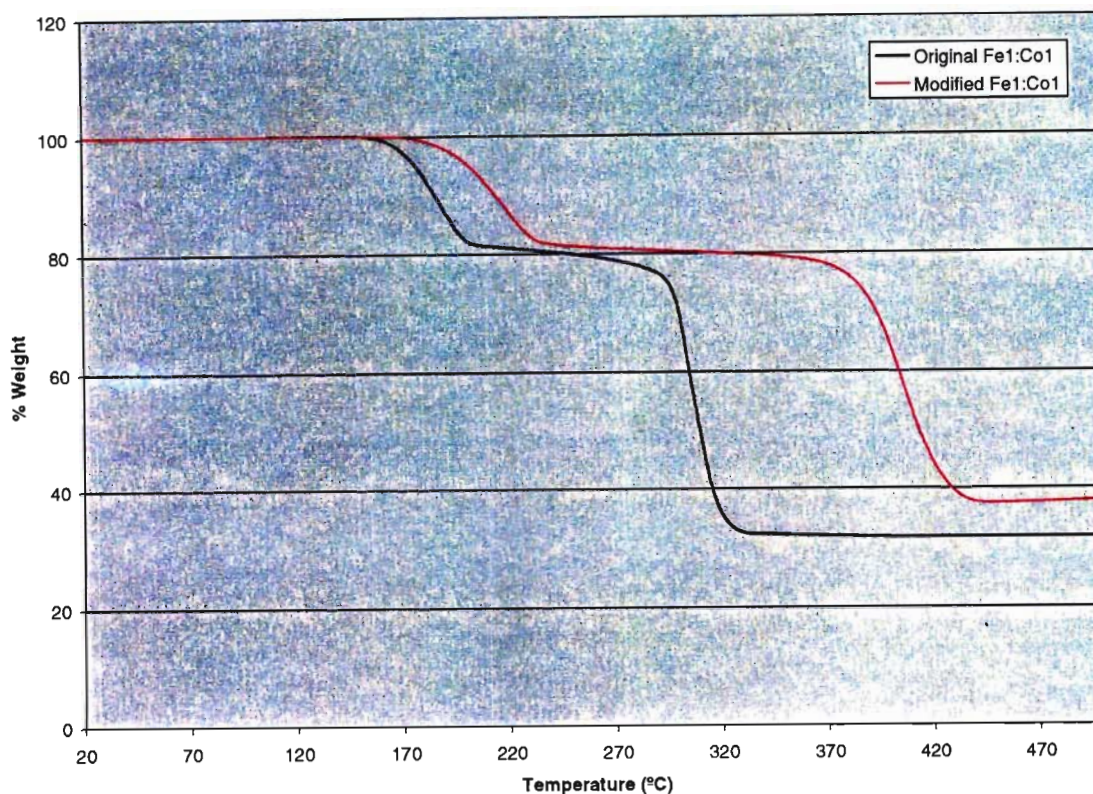


Figure 2.34: TGA curves showing the differing temperatures of dehydration and decomposition of the different equimolar iron-cobalt binary oxalates

2.8 CONCLUSIONS

Using the experimental procedures described, it is possible to produce certain metal powders via the pyrolysis of metal oxalates.

This method of metal powder production uses relatively moderate reaction conditions e.g., low temperatures during the pyrolysis stage. It is also considered a "clean" way to produce metal powders, as only the metal is left after pyrolysis, the carbon and oxygen associated with the oxalate precursor being removed as CO or CO₂. This leads to high yields of high purity metal powders.

One of the aims of this investigation was produce finely divided metal powders. Although the metal powders produced were between 3 and 20 μm in size which classifies them industrially as 'fines' [139], other techniques are available that produce much smaller nano-size particles. However, these techniques, such as

sol-gel and electrochemical reduction, are expensive to operate on a large scale. Because of the relatively undemanding reaction conditions of the oxalate route, larger scale production is possible.

It has also been shown that by mixing the starting sulfates in stoichiometric proportions it is possible to form oxalate solid solutions with pre-determined ratios of metal ions. These can then be pyrolysed to form mixed metal powders or alloys of known stoichiometry. This is true of the metals under investigation in this dissertation i.e., iron, cobalt and nickel. The oxalates of these three metals were shown to have a complete range of solubility when forming solid solutions due to similarity in size of the ionic radii. Other workers, such as Schuele [90], found that complete solubility is not possible if the ionic radii of the metals in the respective oxalates differ too widely. It was also evident from the results obtained for the binary and ternary compounds, that the morphology of the solid solutions was controlled and altered by differing proportions of metal ions in the compounds.

The morphology of the starting oxalate was retained through to that of the resultant metal powder. Since during pyrolysis about 70% weight loss occurs with no corresponding reduction in volume, it can be concluded that the resultant metal powders are highly strained and have large surface areas. This leaves the powders in a highly reactive state. This can be considered an advantage, depending on what the powder will be used for. A disadvantage is that the metal powders are difficult to handle and oxidize extremely easily. At worst they are pyrophoric, igniting in the presence of air. Special precautions need to be observed when handling these compounds to ensure safety.

Some of the morphologies produced during the course of this investigation were commercially undesirable. As stated in Section 2.4 the needle-like morphology of the oxalate compounds containing cobalt would cause problems in industry due to their packing and flowing characteristics. Changing the morphology of the cobalt oxalate dihydrate proved to be simple by the use of harsher conditions for synthesis. Although the morphology was altered to a more desirable 'spherical' one, none of the other characteristics associated with the cobalt oxalate changed, such as the crystal parameters. This was not the case for the binary oxalate of

stoichiometry $\text{Fe}_{0.5}\text{Co}_{0.5}\text{C}_2\text{O}_4 \cdot 2\text{H}_2\text{O}$. The morphology of this compound changed when harsher synthesis conditions were used, in a similar manner to that of the single cobalt oxalate. However, XRD showed that the crystal structure had changed to reflect that of the iron rather than the cobalt oxalate.

As stated in Chapter 1, the XRD pattern of iron(II) oxalate differs from those of cobalt(II) and nickel(II) oxalates, which are analogous. When these compounds form solid solutions, under mild reaction conditions (Chapter 4), in either binary or ternary compounds the crystal structure of the cobalt (or nickel) oxalate dominates (regardless of how much iron is present). This led to all the binary and ternary compounds under investigation decomposing to the metal/alloy. This was expected as it is well documented that both cobalt and nickel oxalate decompose to the metal. The binary equimolar Fe-Co oxalate compound that had been modified through use of harsher reaction conditions, gave an XRD pattern analogous to that of iron(II) oxalate, and decomposed to the oxide.

These results lead to the conclusion that it is the crystal structure, or more accurately the space group, of the compound that determines the pyrolysis product. Since the exact differences in structure between the iron(II) oxalate on the one hand, and the cobalt(II) and nickel(II) oxalates on the other, have not as yet been fully determined, it opens up an interesting area for future study. In addition the thermodynamics governing the decomposition of the oxalate to the metal or oxide during pyrolysis require further study.

INVESTIGATION OF METAL CARBONYL CLUSTERS

3. INTRODUCTION

Only limited thermal decomposition studies have been carried out on unsupported cluster carbonyls due to aggregation of the clusters that occurs during the decomposition process. For most catalytic functions this is undesirable, as particles must be as finely divided as possible. What was of interest to this preliminary study, however, was the possibility of decomposing these homonuclear cluster carbonyls to the metal. If this can be demonstrated, future work would be to synthesise heteronuclear cluster carbonyls, with a view to producing highly specific alloys of known stoichiometry.

To this end triiron dodecacarbonyl and tetracobalt dodecacarbonyl were thermally decomposed, the reaction conditions noted, and the decomposition products characterised.

3.1 TRIIRON DODECACARBONYL

As mentioned in Chapter 1, Section 1.2, the thermal decomposition of unsupported $\text{Fe}_3(\text{CO})_{12}$ has been studied by Fillman and Tang [133], and Psaro *et al.* [129]. Fillman and Tang decomposed the $\text{Fe}_3(\text{CO})_{12}$ under an argon atmosphere, and found that the CO was lost in a single peak, as shown by Quadrupole Mass Spectroscopy (QMS) thermal evolution profiles. Their results from TGA studies, however, suggested that metallic iron was not the final product, since the weight loss was less than expected theoretically for decomposition to the metal. They suggested that the formation of either iron carbide or iron oxide, due to CO dissociation, was more likely. Psaro *et al.* [129] on the other hand postulated that $\text{Fe}_3(\text{CO})_{12}$ does indeed decompose to the metal, but, because it is so finely divided, it is pyrophoric, and easily reacts with the very small amounts of oxygen impurity present in the helium stream under which the compound was pyrolysed.

3.1.1 Characterisation of Thermal Decomposition Products

The triiron dodecacarbonyl was bought from Strem Chemicals, and used without further purification. The thermal decomposition of the triiron dodecacarbonyl was first carried out via thermogravimetric analysis. After the decomposition conditions were established, the reaction was scaled up, and carried out in a tube furnace. In all cases the decomposition was carried out under an atmosphere of nitrogen.

3.1.1.1 Thermogravimetric Analysis

There was a large difference in the TGA traces obtained for the decomposition of the $\text{Fe}_3(\text{CO})_{12}$ at different ramp rates (Figure 3.1). The results are summarised in Table 3.1. When the temperature was increased at $5^\circ\text{C}/\text{min}$ a single decomposition step, initiated at $T_i = 78^\circ\text{C}$, was observed. The final temperature of decomposition, T_f , was at 84.5°C . The weight loss associated with the decomposition was 61.6%. The temperature increase was stopped at 200°C , a reason why the second step of the reaction was not observed.

Table 3.1: Comparison of TG analysis of $\text{Fe}_3(\text{CO})_{12}$ at differing heating rates

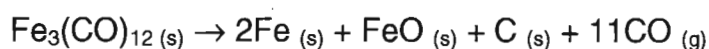
Heating Rate	T_i^a ($^\circ\text{C}$)	T_f^b ($^\circ\text{C}$)	Observed weight loss (%)
$5^\circ\text{C}/\text{min}$	78	84.5	61.6
$1^\circ\text{C}/\text{min}$	70 205	135 350	61.9 1.6

^a T_i , temperature at which the compound begins to decompose

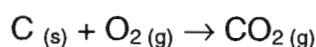
^b T_f , temperature at the end of decomposition

At the heating rate of $1^\circ\text{C}/\text{min}$, two decomposition steps became apparent. The first has an initial temperature of 70°C . This is 8°C lower than at the higher heating rate, but can be explained by the conduction of the heat through the bulk

sample. The decomposition takes longer than at the faster heating rate, finishing at 135°C, with a weight loss of 61.9%. The second step is initiated at 205°C, ending at 350°C with a further weight loss of 1.6%. This brings the total weight loss to 63.5%. The weight loss of the first decomposition step possibly corresponds to the reaction:



The theoretical weight loss for this decomposition route is 61.2%. The second step corresponds to the weight loss of one carbon atom. This is probably lost through reaction with oxygen impurities in the nitrogen flow.



This leaves Fe^0 and FeO as the solid pyrolysis products.

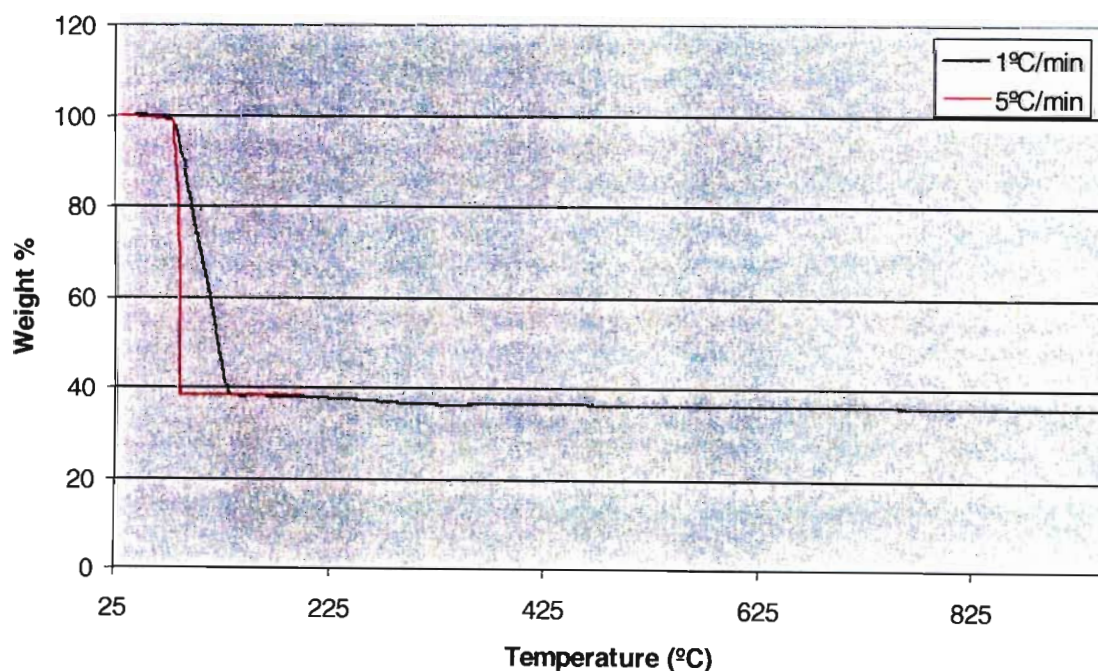


Figure 3.1: TGA curves of $\text{Fe}_3(\text{CO})_{12}$ at two different heating rates

These results differ quite markedly from those of Psaro *et al.* [129], who found a weight loss of only 37.5% when thermal decomposition took place under a helium atmosphere, and Fillman and Tang [133], who observed a weight loss of 41.0% with pyrolysis in argon.

Tube Furnace

Pyrolysis was carried out in a tube furnace, at 100°C under a nitrogen atmosphere. Samples were taken for characterisation after 24 hours. Another experiment was then carried out in which the furnace temperature was taken up to 900°C for 24 hours.

3.1.1.2 IR

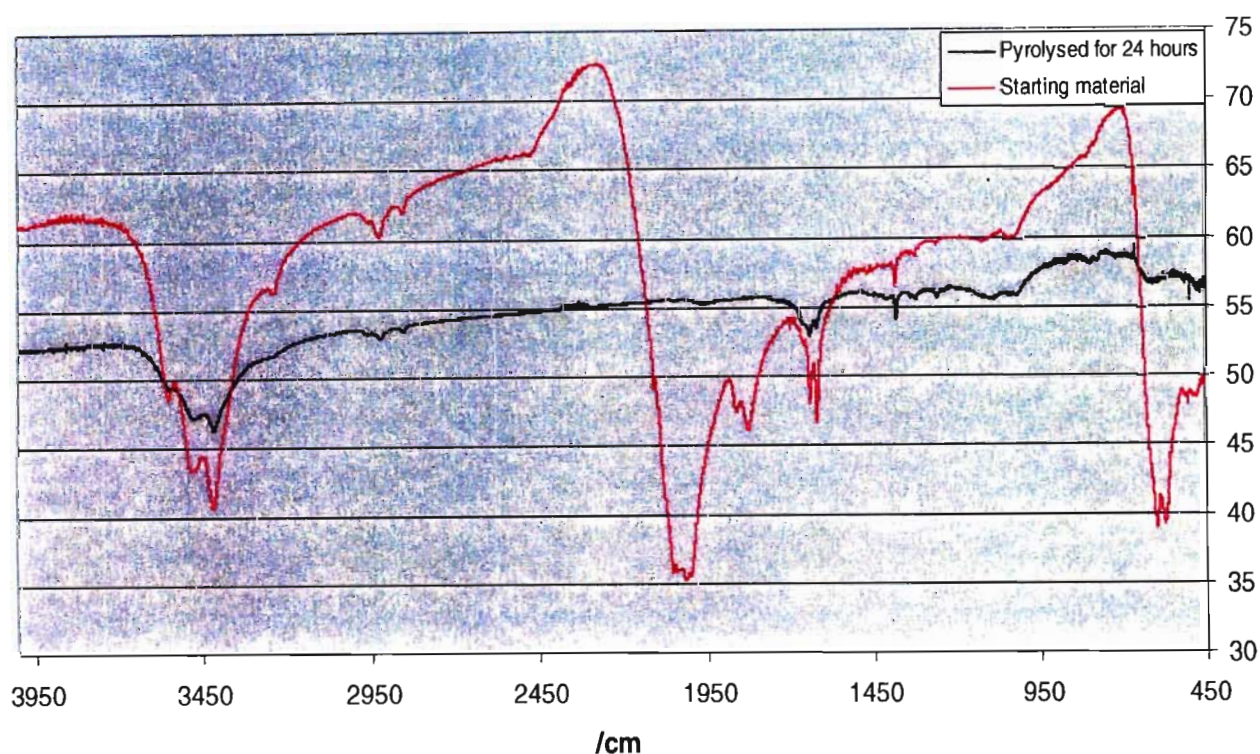


Figure 3.2: IR spectra of $\text{Fe}_3(\text{CO})_{12}$ and product after pyrolysis at 100°C for 24 hours under a nitrogen atmosphere.

The IR spectrum for $\text{Fe}_3(\text{CO})_{12}$ shows the prominent carbonyl stretching absorption bands at 2043, 2009 and 1993 cm^{-1} . After thermal decomposition in a tube furnace at a temperature of 100°C for 24 hours, these bands have disappeared, indicating the loss of all the terminal and bridging carbonyls. The stretching frequencies at the lower wave numbers, tentatively assigned to the bonding of the carbonyls to the metal at 595 and 572 cm^{-1} also disappear after pyrolysis (Figure 3.2).

3.1.1.3 XRD

The $\text{Fe}_3(\text{CO})_{12}$ pyrolysis products were considered to be air sensitive, and thus were coated with epoxy glue before being examined by XRD.

Figure 3.3 shows the XRD trace of the $\text{Fe}_3(\text{CO})_{12}$ pyrolysis product after it has been pyrolysed for 24 hours at 100°C and also the XRD pattern obtained for the $\text{Fe}_3(\text{CO})_{12}$ pyrolysis product after 24 hours at 900°C. Only the background pattern of the epoxy glue, used to coat the sample, was observed after 24 hours at 100°C, and it is assumed that the loss of CO gas from the crystal lattice would have left the resultant product strained, without any long-range order. What is observed is the pattern for the epoxy glue used to coat the product. This means either there is no long-range order in the product, or that the particle size is so small, that the peaks have become too broad and diffuse to determine. In order to try and induce some order, or increase the particle size by sintering, the tube furnace was taken up to 900°C for 24 hours, and allowed to cool down slowly with the product inside.

Table 3.2: *d-values (Å) of the pyrolysis products of $\text{Fe}_3(\text{CO})_{12}$*

Compound			
Fe	2.030	1.434	1.170
Fe_3O_4	2.962	2.526	

After the furnace had cooled, the product was removed into a glove box. There appeared to be three different products. On top of the porcelain boat, there was a fluffy, grey product that looked similar to cotton wool. Below this was a grey powder, and coating the boat was a shiny, mirror-like product that flaked off quite easily. These different morphology types turned out to be the same products, the XRD pattern of which can be seen in Figure 3.3. The resultant products were found to be magnetic. The main product appears to be that of body-centred cubic (bcc) metallic α -iron, with a very small amount of Fe_3O_4 . This result correlates well with the TGA results where it was postulated that the products of decomposition were Fe and FeO.

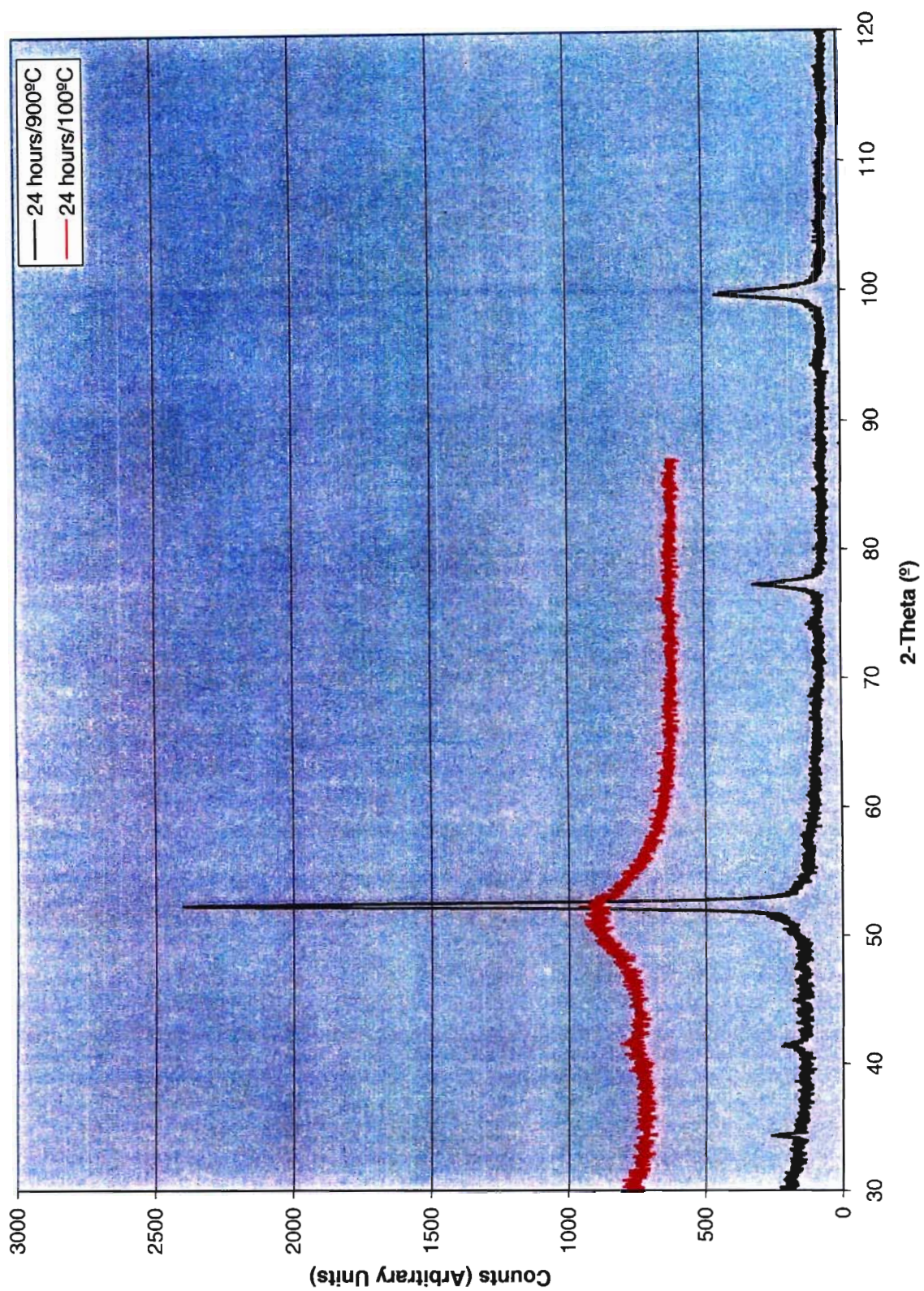


Figure 3.3: XRD patterns of Triiron Dodecacarbonyl pyrolysis products, after 24 hours at 100°C and 900°C respectively.

As mentioned in Chapter 2, Section 2.1, FeO is unstable below 573°C, and decomposes to:



This accounts for the presence of the Fe₃O₄ in the XRD patterns.

The *d*-values of the solid pyrolysis products of Fe₃(CO)₁₂, namely bcc Fe and Fe₃O₄, calculated from the peaks in Figure 3.3 are given in Table 3.2. The *d*-values found in this study for bcc iron and Fe₃O₄ correspond closely to those published in the JCPDS [51].

3.1.1.4 SEM

The micrographs of the starting material, Fe₃(CO)₁₂, show block-like particles of varying sizes. The particles do not look very crystalline, and exhibit cracks and fissures (refer to Figure 3.4).

After three hours of heating the Fe₃(CO)₁₂ sample at 100°C the appearance did not change markedly, although there has been an increase in fragmented pieces. There also seems to be an increase in the size of the fissures present on the surface of the crystals. This would be due to some loss of CO through the decomposition process (Figure 3.5)

After 24 hours at 100°C the block-like particles of the starting material have disappeared, and in their place are flakes of various sizes. As can be seen in Figure 3.6(a) the flakes are very smooth on the one side, and rough on the other. Figure 3.6(b) gives a clear indication as to why no XRD pattern was acquired for this compound. The pyrolysis product does not appear to be crystalline at all, and thus would show no evidence of any long-range order. Evidence of disruption from the release of the CO gas is clearly evident.

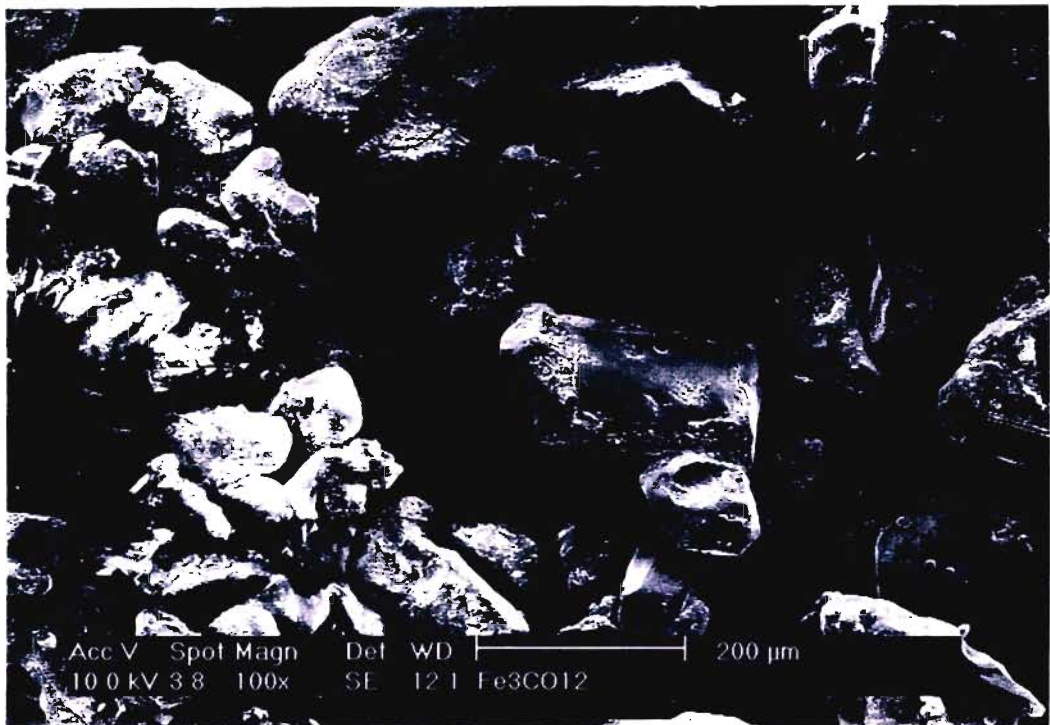


Figure 3.4: SEM photograph of $\text{Fe}_3(\text{CO})_{12}$

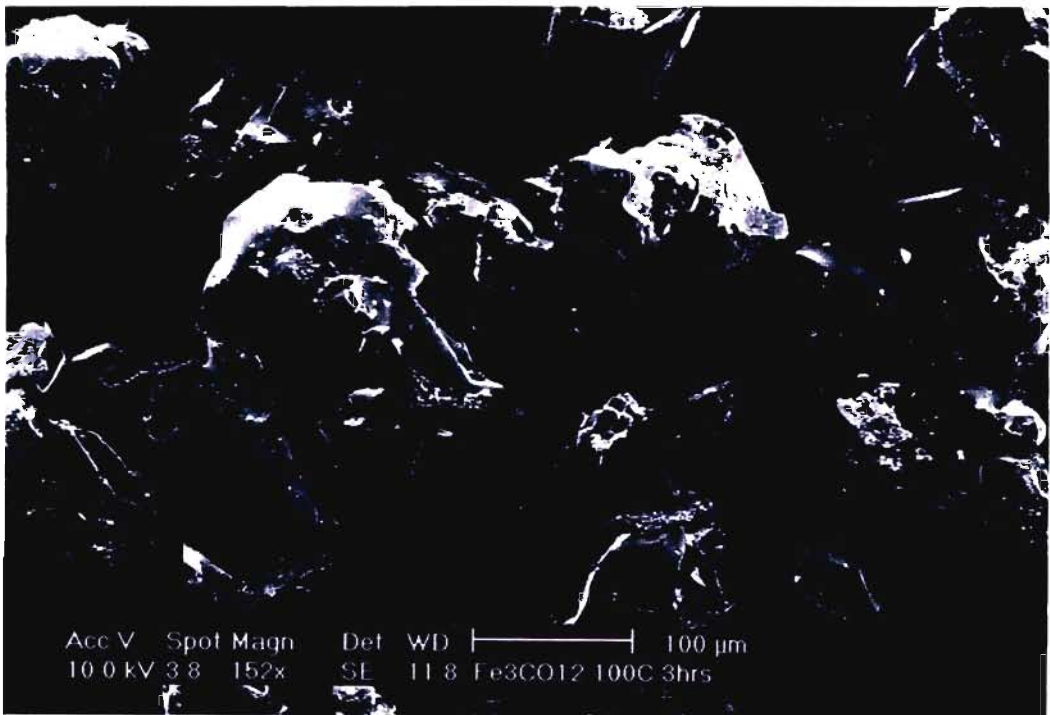


Figure 3.5: SEM photograph of $\text{Fe}_3(\text{CO})_{12}$ pyrolysed for 3 hours at 100°C

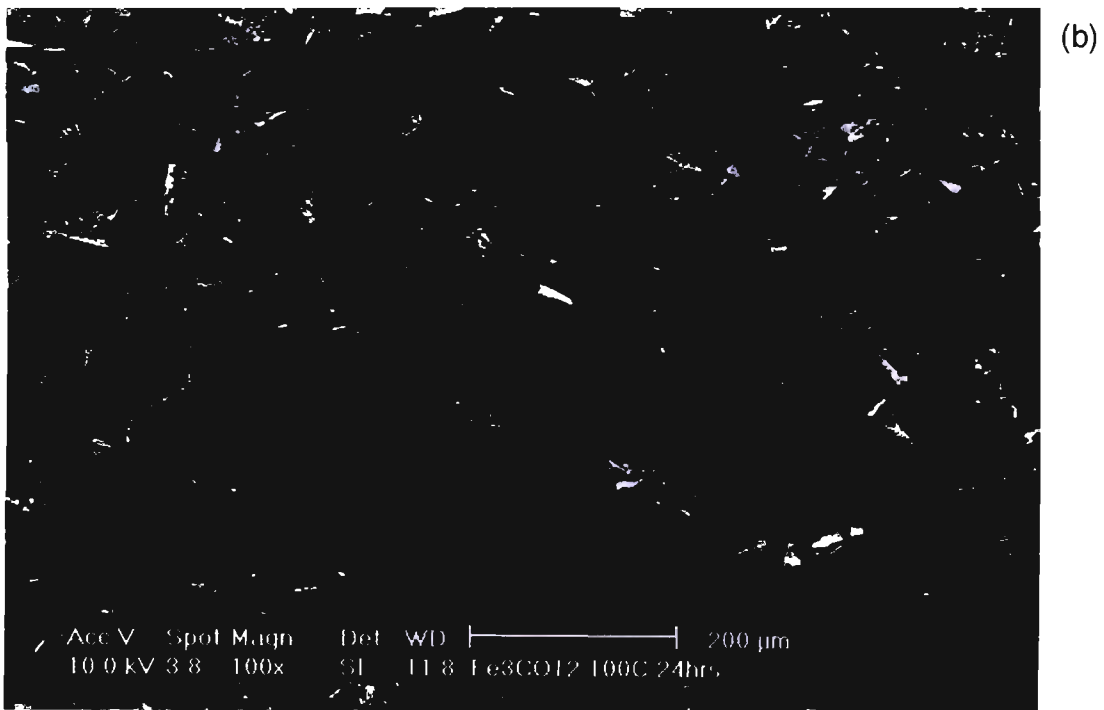
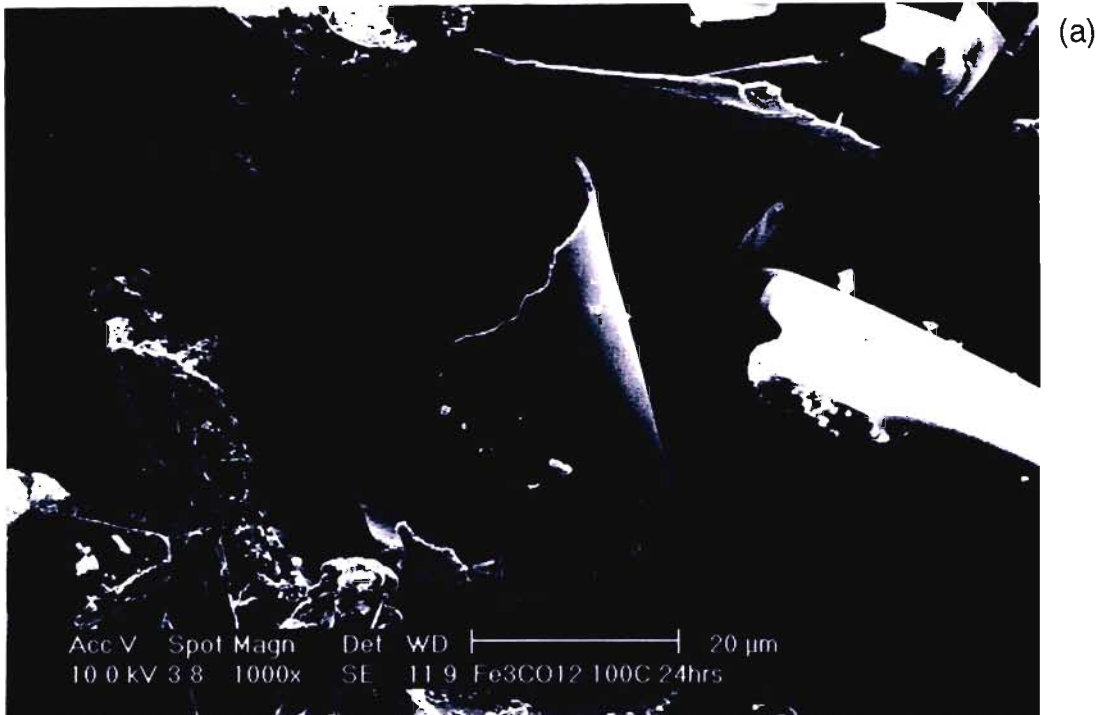


Figure 3.6: SEM photographs of $\text{Fe}_3(\text{CO})_{12}$ pyrolysed for 24 hours at 100°C
(a) 1 000 x and (b) 100 x

3.2 TETRACOBALT DODECACARBONYL

As with $\text{Fe}_3(\text{CO})_{12}$, the thermal decomposition of unsupported tetracobalt dodecacarbonyl has been studied by Fillman and Tang [133], and by Psaro *et al.* [129]. Fillman and Tang found that there was a multi-feature CO loss for the decomposition of $\text{Co}_4(\text{CO})_{12}$, as evidenced by the QMS carbonyl evolution profiles. They found that $\text{Co}_4(\text{CO})_{12}$ clearly decomposed to metallic cobalt [133]. They postulated that the loss of CO initially occurs one-by-one, followed by a major loss to arrive at the cluster $\text{Co}_4(\text{CO})_8$ or the dimer $\text{Co}_2(\text{CO})_4$, which subsequently decomposes completely to the metal.

Psaro *et al.* [129] on the other hand found that at slow heating rates oxides were produced in the thermal decomposition of $\text{Co}_4(\text{CO})_{12}$. They reasoned that, since at higher heating rates weight losses approximating the formation of the metal were achieved, cobalt metal was in fact formed at slow heating rates but that the metal, being pyrophoric, was oxidised by trace amounts of oxygen in the helium stream.

3.2.1 Characterisation of Thermal Decomposition Products

The tetracobalt dodecacarbonyl was bought from Strem Chemicals, and used without further purification or characterisation. Thermal decomposition conditions were established via thermogravimetric analysis, and the reaction then scaled up and carried out in a tube furnace. In all cases the decomposition was carried out under a nitrogen atmosphere.

3.2.1.1 Thermogravimetric Analysis

As with the TGA traces for $\text{Fe}_3(\text{CO})_{12}$, the TGA traces for $\text{Co}_4(\text{CO})_{12}$ differed markedly with differing ramp rates. The results are summarised in Table 3.3.

Table 3.3: Comparison of TGA curves of $\text{Co}_4(\text{CO})_{12}$ at differing heating rates

Heating Rate	T_i^a (°C)	T_f^b (°C)	Observed weight loss (%)
5°C/min	47.5	52.5	39.0
1°C/min	50	130	33.9
	215	292	5.3
	292	870	8.1
	870	960	3.4

^a T_i , temperature at which the compound begins to decompose

^b T_f , temperature at the end of decomposition

When the temperature was increased at a rate of 5°C per minute, a single decomposition step was observed, although it was not smooth. The weight loss was recorded as 39% which corresponds to the equation:



The theoretical weight loss for this decomposition is 39.2%. The decomposition occurred at 47.5°C and was complete by 52.5°C (Figure 3.7). This result is contrary to those of Fillman and Tang [133], and by Psaro *et al.* [129] as discussed in Section 3.2.

Both sets of workers found the decomposition of $\text{Co}_4(\text{CO})_{12}$ was to metallic cobalt, although Psaro *et al.* [129] found that this was dependent on the heating rate used. They postulated that the longer the $\text{Co}_4(\text{CO})_{12}$ was in the gas stream (in their case helium) the more likely it was to oxidise, due to oxygen impurities in the gas stream.

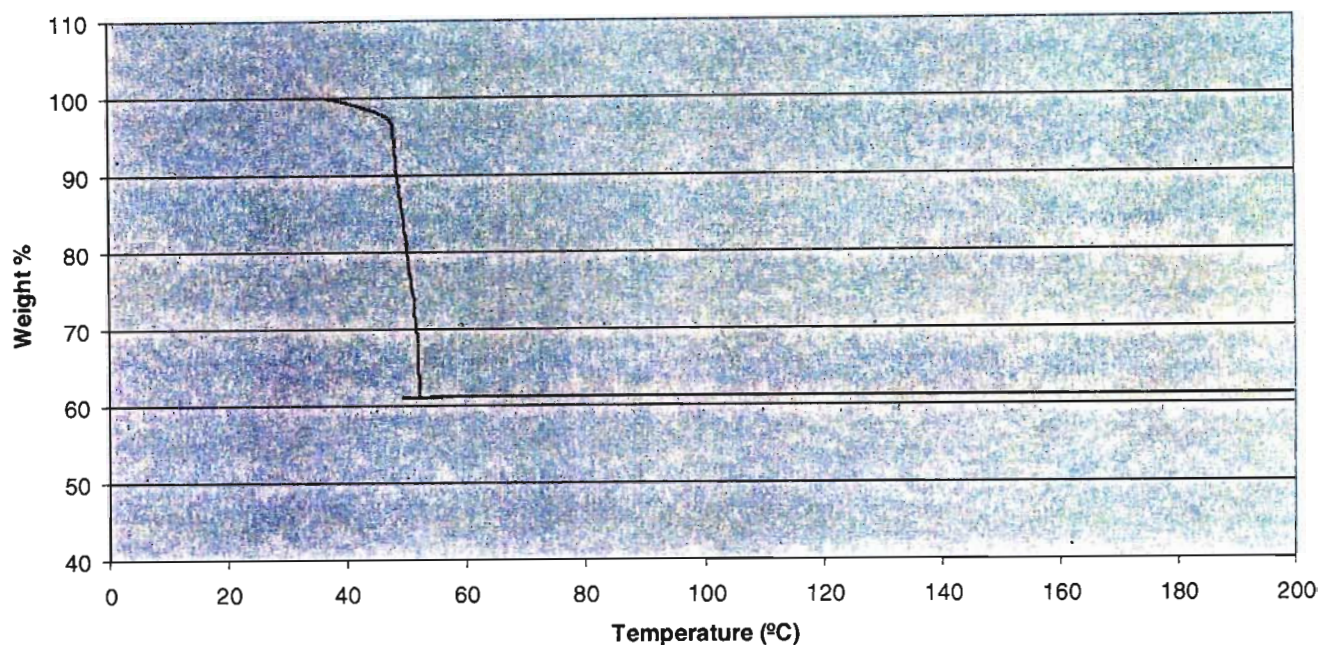


Figure 3.7: TGA curve of $\text{Co}_4(\text{CO})_{12}$ at a heating rate of $5^\circ\text{C}/\text{min}$ under N_2

Fillman and Tang [133] reported a multifaceted CO loss in the thermal decomposition of $\text{Co}_4(\text{CO})_{12}$, as evidenced by the QMS carbonyl evolution profiles but a single thermogravimetry step to metallic cobalt at a heating rate of $10^\circ\text{C}/\text{min}$.

In this study, the heating rate was reduced in order to determine if there was a multi-step decomposition of $\text{Co}_4(\text{CO})_{12}$. The heating rate was therefore decreased to 1°C per minute (Figure 3.8). The results in Table 3.3 show that a multi-step decomposition occurred.

There was an initial decomposition between 50 and 130°C with an associated weight loss of 33.9% , which corresponds to a loss of 7CO (theoretical loss is 34.3%). This would appear to be the formation of a stable intermediate, or group of products, although none were able to be isolated in this study.

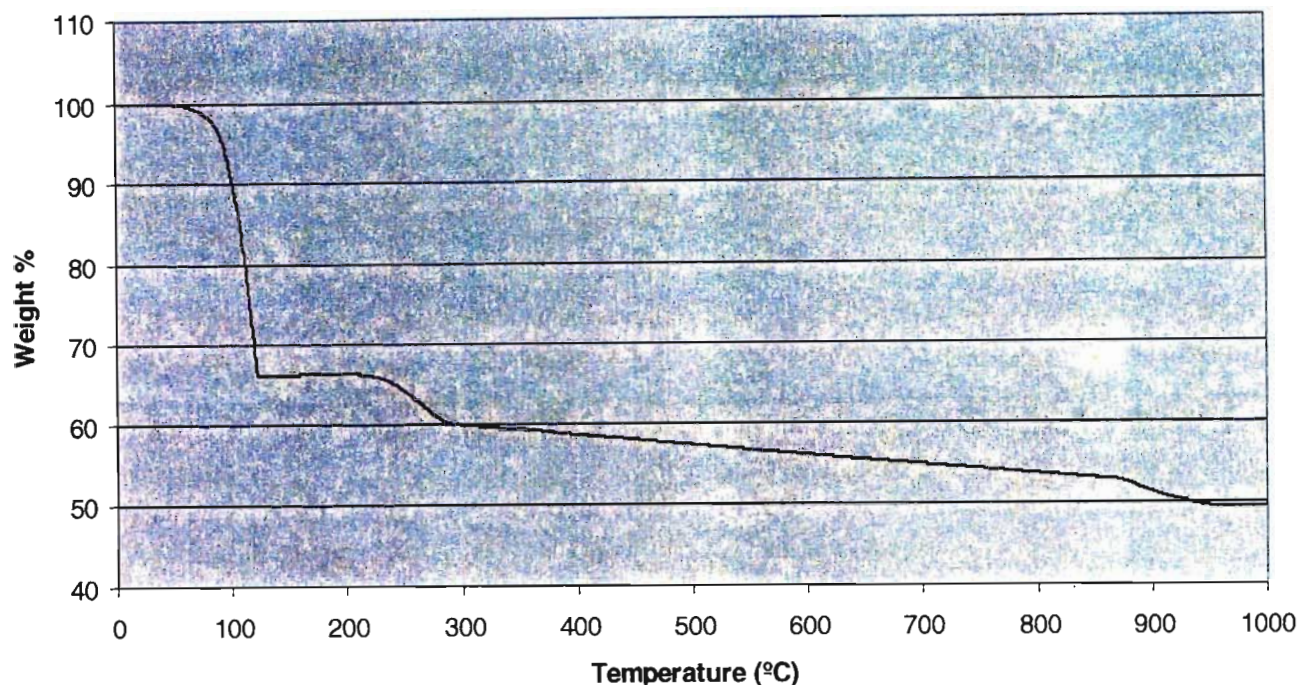
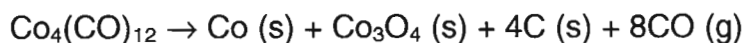


Figure 3.8: TGA curve of $\text{Co}_4(\text{CO})_{12}$ at a heating rate of $1^\circ\text{C}/\text{min}$ under N_2

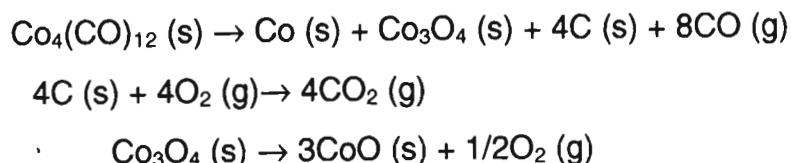
The next step was initiated at 215°C and finished at 292°C . This brings the weight loss up to that observed in the TGA curve at $5^\circ\text{C}/\text{min}$ (Figure 3.7), i.e., a weight loss of 39.2%. As mentioned above this decomposition corresponds to the reaction:



As with the triiron dodecacarbonyl, the carbon produced in the decomposition reaction is slowly oxidised by oxygen impurities in the nitrogen gas stream, and this is evidenced by the slope of the TGA curve from 292°C to 870°C . The decrease amounts to a further 8.1% (theoretical value 8.4%). In order to check for the formation of Co_3O_4 , the furnace was taken to a temperature of 1000°C . The decomposition of Co_3O_4 to CoO is expected at 950°C by the reaction:



As can be seen in Figure 3.8, at 870°C there is another weight loss, resulting in a total weight loss of 50.7%. The theoretical value for the reaction series:



is 50.4%, and is thus in very good agreement with the experimental results. The presence of Co_3O_4 is also established by the weight loss from 870 to 960°C.

3.2.1.2 Tube Furnace

As with the triiron dodecacarbonyl, pyrolysis of the $\text{Co}_4(\text{CO})_{12}$ was carried out in a tube furnace, at 100°C under a nitrogen atmosphere. Samples were taken for characterisation after 24 hours. Another experiment was then carried out where the furnace temperature was taken up to 900°C for 24 hours.

3.2.1.3 IR

The C-O stretching frequencies associated with carbonyl bonding were found at 2054 and 2024 cm^{-1} . After 24 hours at 100°C these bands had completely disappeared. The bands at 546 and 526 cm^{-1} associated with the M-C bonding of the carbonyls also disappeared.

3.2.1.4 XRD

The $\text{Co}_4(\text{CO})_{12}$ pyrolysis products were considered to be air sensitive, and thus were coated with an epoxy glue in order to exclude oxygen while being X-rayed.

The results of the TGA suggested that an XRD pattern of cobalt metal and the oxide Co_3O_4 would be found for the pyrolysis product of $\text{Co}_4(\text{CO})_{12}$ after 24 hours at 100°C. In fact, no pattern was observed. This was a similar problem to that encountered for the triiron carbonyl. Again, the pyrolysis product was either too disordered or too highly dispersed to give any diffraction pattern.

Sintering was thus induced by taking the furnace up to 900°C for 24 hours in order to force some long-range order into the product. This experiment was successful, and the XRD pattern measured is shown in Figure 3.9. The presence of metallic cobalt is evident from the peaks at 52.28°, 61.06°, 91.40° and 114.54° 2 θ . The d -values for this cobalt pattern are given in Table 3.4.

The XRD pattern for the cobalt metal is found with the more intense pattern of CoO. This was expected after taking the furnace to 900°C. The peaks at 43.08°, 50.10°, 73.20°, 88.60°, 93.66° and 114.38° 2 θ are the peaks associated with the XRD pattern of CoO (refer to Table 3.4 for the d values).

Table 3.4: d values (Å) for the solid pyrolysis products of $Co_4(CO)_{12}$

Compound						
Co ⁰	2.032	1.763	1.251	1.064		
CoO	2.439	2.115	1.512	1.282	1.228	1.066

3.2.1.5 SEM

The SEM photograph shown in Figure 3.10, gives a clear indication of the disruption to the crystal caused by the thermal decomposition. The loss of CO has almost shattered the crystal, leaving tiny fragments. The remaining larger pieces of crystal after pyrolysis appear to have suffered large internal disruption, and is a likely reason for the lack of an XRD pattern.

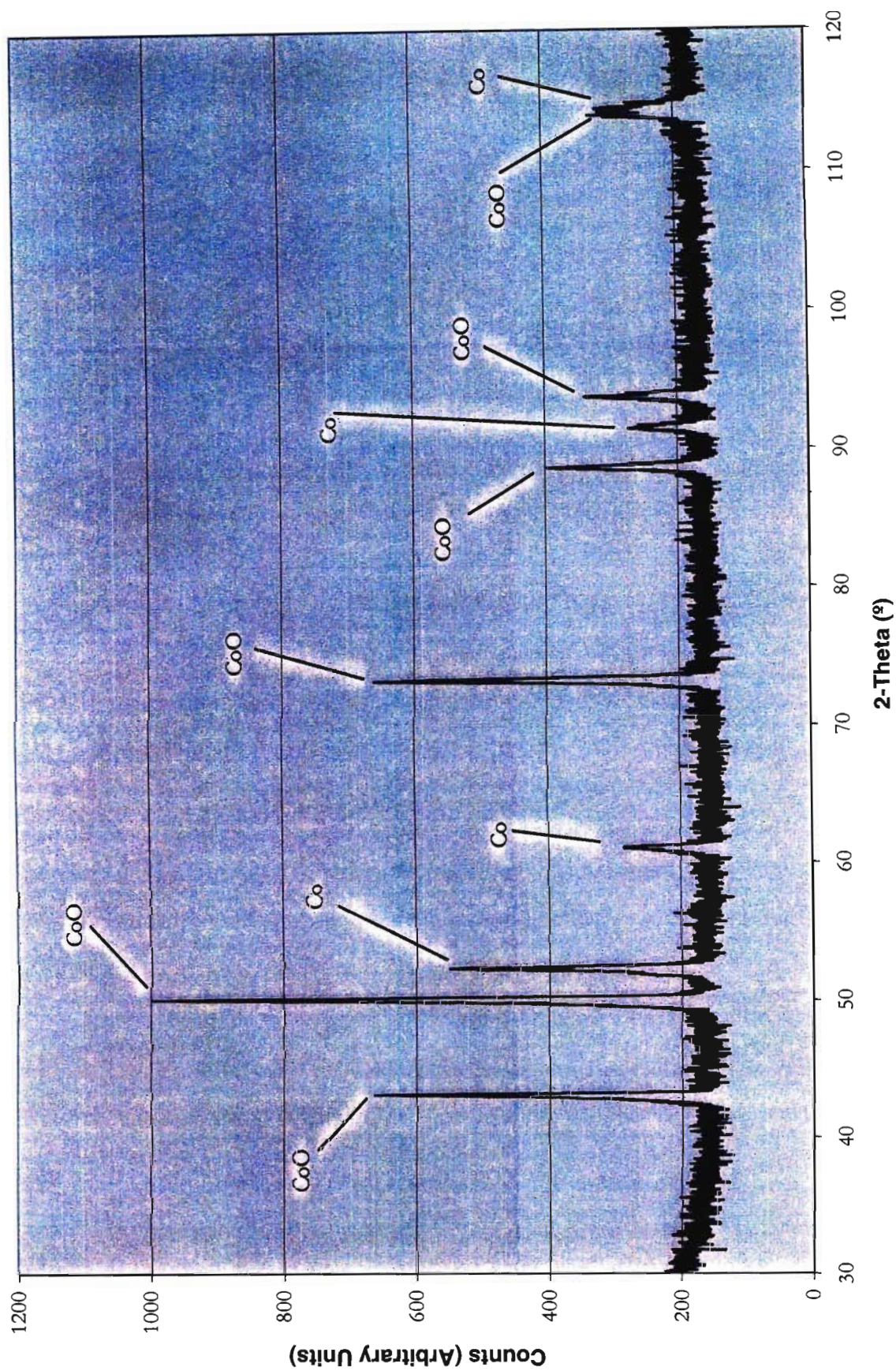


Figure 3.9: Pyrolysis products of Tetracobalt Dodecacarbonyl, showing patterns of Co and CoO

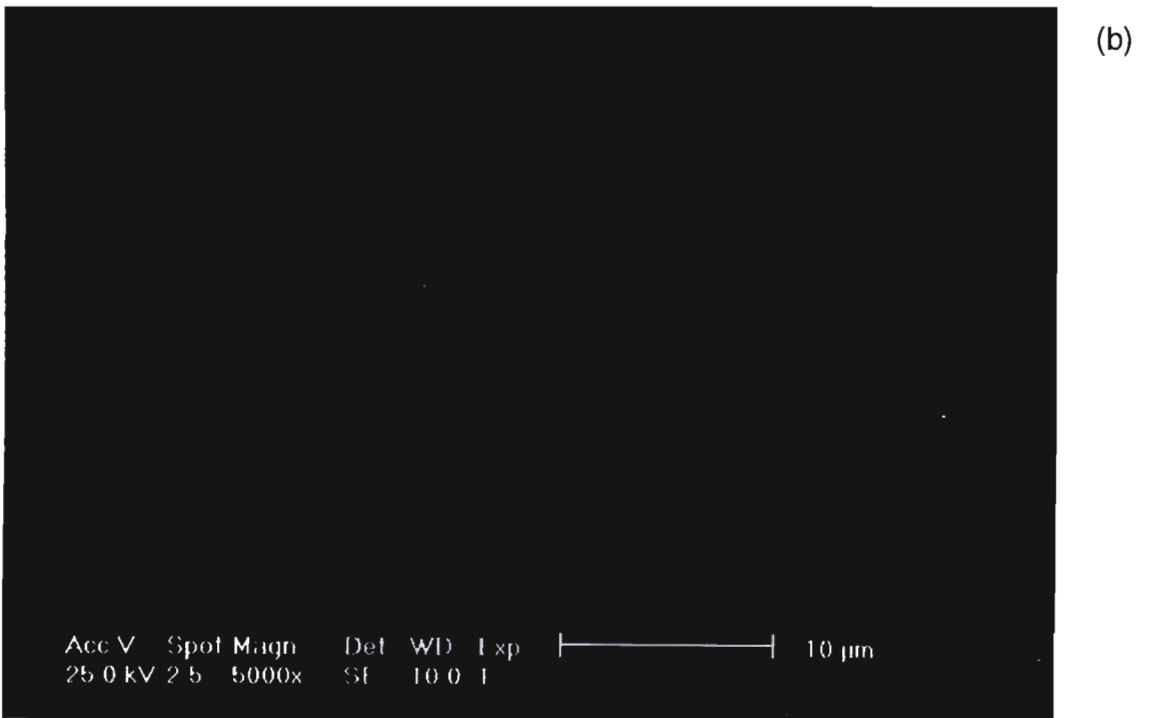
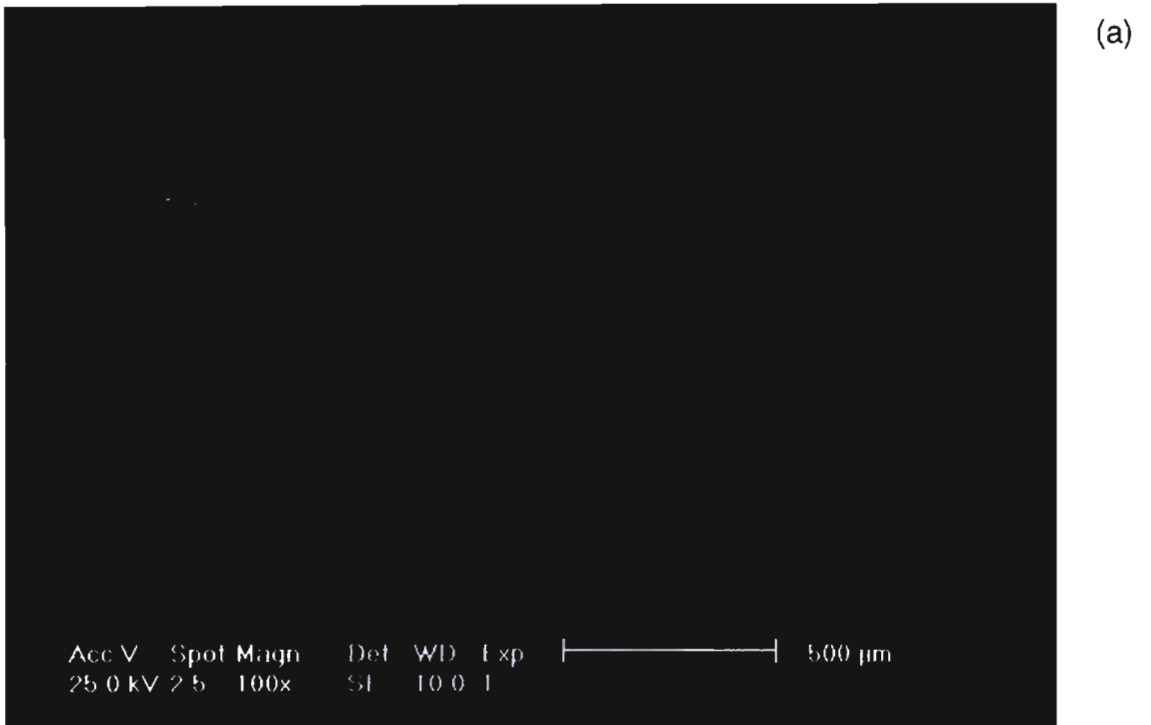


Figure 3.10: SEM micrograph of $\text{Co}_4(\text{CO})_{12}$ pyrolysed for 24 hours at 100°C
(a) 100 x and (b) 5 000 x magnification

3.3 CONCLUSION

The two carbonyl clusters under investigation decomposed at relatively low temperatures under a nitrogen atmosphere. When comparing this work to others, namely Fillman and Tang [133], and Psaro *et al.* [129], it can be seen that the products of thermal decomposition depend largely on the reaction conditions, most notably the rate of pyrolysis and the atmosphere under which pyrolysis takes place.

The aim of the experiments was to determine if the thermal decompositions of the triiron dodecacarbonyl and tetracobalt dodecacarbonyl were suitable for the production of the respective metals. As the presented results show, neither was particularly successful under the prescribed reaction conditions. The final solid products, although both contained metal, were contaminated by the oxide and carbon even though both contained some metal.

Another disadvantage of this technique was briefly discussed previously, and that is the tendency of unsupported carbonyl clusters to aggregate. This leads to larger particle sizes, which are not ideal. Since the starting materials used were purchased from a commercial supplier, the particle sizes were large to start with, so this result could not be properly accessed by this investigation.

Future work in this field would include looking at mixed-metal carbonyl clusters, and possibly a deeper look at the differing products gained by changing the reaction conditions.

EXPERIMENTAL

4. INTRODUCTION

The techniques and methods used for both the oxalate and carbonyl research, used in this dissertation were similar, and thus will be discussed together. Differences will be highlighted where necessary.

4.1 MATERIALS

4.1.1 Oxalate Chemistry

$\text{Fe}(\text{SO}_4)_2 \cdot 7\text{H}_2\text{O}$, $\text{Ni}(\text{SO}_4)_2 \cdot 7\text{H}_2\text{O}$ and $\text{Co}(\text{SO}_4)_2 \cdot 7\text{H}_2\text{O}$ were obtained from Aldrich. Oxalic acid was obtained from SAARChem. All the compounds were chemically pure, and were used without further purification. Milli-Q water was used, and analytical grade sulphuric acid was obtained from SAARChem.

4.1.2 Carbonyl Chemistry

$\text{Fe}_3(\text{CO})_{12}$ and $\text{Co}_4(\text{CO})_{12}$ were obtained from Strem Chemicals. Again the compounds were chemically pure and used without further purification. These compounds were considered air sensitive, and were thus kept under a nitrogen atmosphere in a dry glove box.

4.2 METHODS

4.2.1 4.2.1.Synthesis of Bivalent Transition Metal Oxalates

The metal oxalates of iron(II), cobalt(II) and nickel(II) were prepared using the corresponding sulfate salts. In each case oxalic acid (250 ml of a 0.1M solution) was added to a mixture of water (125 ml) and acetone (125 ml) and heated to 60 °C. A solution (250 ml, 0.1M) of the $\text{MSO}_4 \cdot 7\text{H}_2\text{O}$ (M = Fe, Ni or Co) salt, acidified with three drops of sulphuric acid, was added dropwise over 20 hours. Stirring

was continued for a further 20 hours. The product solution was then left to stand until all the precipitate had settled. The remaining clear solution was decanted. The precipitate was filtered and washed sequentially, several times, with cold, Milli-Q water, followed by ethanol and finally acetone. The precipitate was air-dried during the filtration, and then dried in an oven at 60 °C for 4 hours.

Table 4.1 Mole ratios used in the Binary Coprecipitation Reactions

Exp. #	FeSO ₄ ·7H ₂ O	CoSO ₄ ·7H ₂ O	NiSO ₄ ·7H ₂ O
1(a)	3	1	-
1(b)	1	1	-
1(c)	1	3	-
2(a)	3	-	1
2(b)	1	-	1
2(c)	1	-	3
3(a)	-	3	1
3(b)	-	1	1
3(c)	-	1	3

Coprecipitation of the oxalates was carried out by first mixing the solutions of the transition metal sulfate salts in the required mole ratios (Tables 4.1 and 4.2). All mixed solutions were of concentration 0.1M, in keeping with the procedure described above. The reaction for the preparation of simple oxalates via the sulfate analogue was then followed. In this way the binary and ternary coprecipitated oxalates were formed.

Yields of all the compounds synthesised were above 96 % (Chapter 2), and on this basis it was taken that the coprecipitated compounds had precipitated in the required molar ratios.

Table 4.2 Mole ratios used in the Ternary Coprecipitation Reactions

Exp. #	FeSO ₄ .7H ₂ O	CoSO ₄ .7H ₂ O	NiSO ₄ .7H ₂ O
1	1	1	1
2	8	1	1
3	1	8	1
4	1	1	8

4.2.2 Pyrolysis

Pyrolysis of both the oxalates and the carbonyls was carried out in a dry, nitrogen atmosphere in a tube furnace donated by De Beers Diamond Research Laboratories. The nitrogen gas was first passed through a column of BTS catalyst, made by Fluka, which acts as an oxygen scrubber and then through a column of silica gel layered with magnesium hydroxide. The furnace was flushed with nitrogen for an hour before pyrolysis to ensure the removal of oxygen from the reaction chamber.

4.2.2.1 Pyrolysis of Metal Oxalates

Although the temperatures of decomposition were different for each compound, as found from the thermogravimetric analysis, 390 °C was chosen as the standardised temperature by which all the metal oxalates, single, binary and ternary, would have decomposed. During the course of the investigation, samples were left in the furnace for varying times. It was found that one hour completely pyrolysed the sample, but kept sintering to a minimum. This was the time adopted for all the experiments. Care was taken to ensure that the pyrolysed products did not come into contact with air as the finely divided nature of the powders rendered them very susceptible to oxidation. All pyrolysed products were kept in an inert atmosphere (N₂).

4.2.2.2 *Pyrolysis of Metal Carbonyls*

The metal carbonyls decomposed at much lower temperatures than the oxalates, but had to remain in the furnace much longer in order for the reaction to reach completion. Triiron dodecacarbonyl was pyrolysed at 100°C for 24 hours. This led to the formation of a highly magnetic, pyrophoric powder. In order to increase the ease of handling the material the furnace was taken to 900°C for 48 hours to induce sintering, reducing the surface area, and thus the reactivity, of the powder.

Pyrolysis of tetracobalt dodecacarbonyl was carried out in the tube furnace at 100°C under a nitrogen atmosphere. Samples were taken for characterisation after 24 hours. Another experiment was then carried out where the furnace temperature was taken up to 900°C for 48 hours.

As with the metal oxalate pyrolysis products, the pyrolysis products of the metal cluster carbonyls were considered extremely sensitive to air, and thus every precaution was taken to ensure no contact. The compounds were thus kept under a nitrogen atmosphere in a glove box, and coated with epoxy glue before characterisation.

4.3 INSTRUMENTS

Microanalysis was carried out on a Perkin Elmer 2400 CHN Elemental Analyser. All IR spectra were determined in the solid state using potassium bromide discs. Spectral resolution was 1 cm⁻¹, with an accumulation of 10 scans. The instrument used was a Perkin Elmer Spectrum One, Fourier Transfer IR, with Spectrum Version Three software.

Particle size analysis was done by use of the Malvern Mastersizer X Version 1.2 while the scanning electron micrographs were taken on a Philips ESEM XW1234. All samples for the SEM were coated with a thin, uniform, electrically conductive gold film.

The XRD spectra were measured on a Philips PW 1130-90 X-ray diffractometer using monochromated cobalt radiation ($\lambda=1.7909$) and fitted with an automatic sample changer. The experimental conditions for all the oxalate patterns were, a working voltage of 40 kV; a working current of 40 mA, $2\theta = 15-73^\circ$; a scan speed of $1.0^\circ \text{ min}^{-1}$ and a 0.02° step for intensity integration. The measurements were taken at room temperature (25°C) in air. Sietronics software (SIE122D) was used in the collection of the data. The data were then processed using PeakFit version 4, a peak separation and analysis software package.

Dehydration and decomposition of the oxalates and metal cluster carbonyls were studied by thermogravimetry (TG), on a Perkin Elmer Thermogravimetric Analyser. The experiments were carried out at a heating rate of 5°C min^{-1} under a nitrogen atmosphere (flow of $50 \text{ cm}^3 \text{ min}^{-1}$). Platinum sample pans and sample masses of between 1 and 5 mg were used.

4.4 TECHNIQUES

The 2θ values found in the in the XRD patterns were converted to d-values using Bragg's law.

$$2d_{hkl}\sin\theta_{hkl} = \lambda \quad (1)$$

By rearranging the equation the d-values can be found.

$$d_{hkl} = \lambda / 2\sin\theta_{hkl} \quad (2)$$

Where λ was 1.7909 (cobalt radiation)

REFERENCES

1. J. Macek, R. Hrovat, B. Novosel, *J. Therm. Anal.*, 1993, **40**, 335.
2. F. Fievet, J.P. Lagier, M. Figlarz, *MRS Bull*, 1989, **14 (12)**, 29.
3. J. Livage, M. Henry, J.P. Jolivet, C. Sanchez, *MRS Bull*, 1990, **15 (1)**, 18.
4. C.N.J. Wagner, M.S. Boldrick, *J. Alloys and Comp.*, 1993, **194**, 295.
5. J.J.K. Scholten, J.A. Konvilinka, F.W. Beekman, *J. Catal.*, 1973, **28**, 209.
6. R.M. Wilenzick, D.C. Russel, R.H. Morris, S.W. Marschall, *J. Chem. Phys.*, 1967, **47**, 533.
7. D.W. MacKee, F.J. Norton, *J. Phys. Chem*, 1964, **68**, 481.
8. R.D. Rieke, *Science*, 1989, **246**, 1260.
9. L. Chao, R.D. Rieke, *J. Organomet. Chem.*, 1974, **67**, C64.
10. R.D. Rieke, S.E. Bales, *J. Am. Chem. Soc.*, 1974, **96**, 1775.
11. R.D. Rieke, P.M. Hudnall, *J. Am. Chem. Soc.*, 1972, **94**, 7178.
12. M.J. McCormick, K.B. Moon, S.R. Jones, T.P. Hanusa, *J. Chem. Soc., Chem. Commun.*, 1990, 778.
13. J.H. Jean, T.A. Ring, *Langmuir*, 1986, **21**, 251.
14. H. Bonneman, W. Brijoux, T. Jousen, *Angew. Chem., Int. Ed. Engl.*, 1990, **29**, 273.
15. K.S. Suslick, *Science*, 1990, **247**, 1439.
16. P. Boudjouk, D.P. Thompson, W.H. Ohrbom, B.H. Han, *Organometallics*, 1986, **5**, 1257.
17. K. Tsai, J.L. Dye, *Chem. Mater.*, 1993, **5**, 540.
18. N. Toshima, Y. Wang; *Chem. Soc. Japan, Chem. Lett.*, 1993, 1611.
19. G. Schmid, *Chem. Rev.*, 1992, **92**, 1709.
20. H. Lui, N. Toshima, *J. Chem. Soc., Chem. Commun.*, 1992, 1095.
21. J.S. Bradley, E.W. Hill, S. Behal, C. Klein, *Chem. Mater.*, 1992, **4**, 1234.
22. K. Torigoe, K. Esumi, *Langmuir*, 1993, **9**, 1664.

23. M. Harada, K. Asakura, Y. Ueki, N. Toshima, *J. Phys. Chem.*, 1992, **96**, 9730.
24. N. Toshima, M. Harada, Y. Yamazaki, K. Asakura, *J. Phys. Chem.*, 1992, **96**, 9927.
25. Y. Wang, H. Lui, *Polym. Bull.*, 1991, **25**, 139.
26. K. Esumi, M. Shiratori, H. Ishizuka, T. Tano, K. Torigoe, K. Meguro, *Langmuir*, 1991, **7**, 457.
27. T. Sato, S. Kuroda, A. Takami, Y. Yonezawa, H. Hada, *Appl. Organomet. Chem.*, 1991, **5**, 261.
28. R.D. Rieke, *Organometallics*, 1983, **2**, 377.
29. H. Bonneman, B. Bogdanovic, R. Brinkmann, B. Spliethoff, *J. Organomet. Chem.*, 1993, **451**, 23.
30. W.B. Philips, E.A. Desloge, J.G. Skofronick, *Appl. Phys.*, 1967, **39**, 3210.
31. S.C. Davis, K. J. Klabunde, *Chem. Rev.*, 1982, **82**, 152.
32. K. J. Klabunde, H.F. Hfner, T.O. Murdock, R.J. Ropple, *Am. Chem. Soc.*, 1976, **98**, 1021.
33. K. J. Klabunde, Y.X. Li, B. Tan, *Chem. Mater.*, 1991, **3**, 30.
34. G.N. Glavee, K. J. Klabunde, C.M. Sorenson, G.C. Hadjipanayis, *Langmuir*, 1992, **8**, 771 and references therein.
35. P.G. Fox, J. Ehretsman, C.E. Brown, *J. Catal.*, 1971, **20**, 67.
36. M. Ibl, *Chem. Ing.-Technd.*, 1964, **36**, 601.
37. X. Gao, D. Chen and D. Dollimore, *Thermochim. Acta*, 1993, **220**, 75.
38. A. Furstner, *Angew. Chem., Int. Ed. Engl.*, 1993, **32**, 164 and references therein.
39. D. Dollimore, *Thermochim. Acta*, 1991, **117**, 59.
40. J. Fujita, A.E. Martell, K. Nakamoto, *J. Chem. Phys.*, 1962, **36**, 324, 331.
41. G.M. Begun, W.H. Fletcher, *Spectrochim. Acta*, 1963, **19**, 1343.
42. R.E. Hester, R.A. Plane, *Inorg. Chem.*, 1964, 513.
43. H.G.M. Edwards and P.H. Hardman, *J. Molecular Structure*, 1992, **273**, 73.

44. R.I Bickley, H.G.M. Edwards and S.J. Rose, *J. Molecular Structure*, 1991, **243**, 341.
45. H.G.M. Edwards and N.C. Russell, *J. Molecular Structure*, 1998, **443**, 223.
46. H.G.M Edwards, D.W Farwell, S.J Rose and D.N Smith, *J. Molecular Structure*, 1991, **249**, 233.
47. K. Nakamoto, *Infrared Spectra of Inorganic Coordination Compounds*, John Wiley, London, 1974.
48. S.P. Goel and P.N. Mehrotra, *J. Thermal Anal.*, 1985, **30**, 145.
49. R. Deyreix, C. Berro, A. Penoloux, *Bull. Soc. Chem. Fr.*, 1973, **1**, 25.
50. J.P. Langer, H. Peazat, J. Dubernat, *Rev. Chim. Mineral.*, 1969, **6**, 1081.
51. JCPDS.
52. A. Coetzee, D.J. Eve and M.E. Brown, *J. Thermal Analysis*, 1993, **39**, 947.
53. G. Davidson, *Group Theory for Chemists*, 1991, MacMillan Education, 1st Ed., 100 & 108.
54. D. Dollimore, *Thermochim. Acta*, 1987, **117**, 331.
55. D. Broadbent, D. Dollimore and J. Dollimore, *J. Chem. Soc.*, 1966, 1491.
56. D. Broadbent, D. Dollimore and J. Dollimore, *J. Chem. Soc.*, 1966, 278.
57. P. Jacobs and A. Tariq Kureishy, *Trans. of Faraday Soc.*, 1962, **58**, 551.
58. M. Bark, B. Channaa, M. Lallemand and G. Bertrand, *Thermochim. Acta*, 1986, **97**, 369.
59. M.L. Smith and B. Topley, *Proc. R. Soc., London, Ser. A*, 1931, **134**, 244.
60. S. Gurrieri, G. Siracusa and R. Cali, *J. Therm. Anal.*, 1974, **6**, 293.
61. Y. Masuda, Y. Ho, R. Ho and K. Iwata, *Thermochim. Acta*, 1986, **99**, 205.
62. D. Dollimore, D. Griffiths, D. Nicholson, *J. Chem. Soc.*, 1963, 2617.
63. D. Broadbent, D. Dollimore and J. Dollimore, *J. Chem. Soc.*, 1967, 451.
64. K. Nagase, K. Sato and N. Tanaka, *Bull. Chem. Soc. J.*, 1975, **48**, 439.
65. A.K. Galwey and M.A. Mohamed, *Solid State Ionics*, 1990, **42**, 135.
66. A.K. Vijh, *J. of Mat. Sci. Lett.*, 1988, 513.

67. R.J. Acheson and A.K. Galwey, *J. Chem. Soc. A*, 1967, 1167.
68. E.D. Macklen, *J. Inorg. Nucl. Chem.*, 1968, **30**, 2689.
69. A.K. Galwey and M.A. Mohamed, *Thermochim. Acta*, 1993, **213**, 269.
70. S. Gregg, *J. Chem. Soc.*, 1953, 3940.
71. G. Ellingham, *J. Soc. Chem. Ind.*, 1944, **63**, 125.
72. R. Kornienko, *Ukrain. Khim. Zhur.*, 1957, **23**, 159.
73. J. Robin, *Bull. Soc. Chim. France*, 1953, 1078.
74. D. Dollimore and D. Nicholson, *J. Chem. Soc.*, 1962, 960.
75. G.C. Nicholson, *J. Inorg. Nucl. Chem.*, 1967, **29**, 1599.
76. E.D. Macklen, *J. Inorg. Nucl. Chem.*, 1967, **29**, 1229.
77. H.I. Halsey and A.M. Prichard, *J. Chem. Soc. A*, 1968, 2878.
78. J. MacDonald and C. Hinshelwood, *J. Chem. Soc.*, 1925, 2764.
79. M.E. Brown, D. Dollimore and A.K. Galwey, *J. Chem. Soc. Faraday Trans. 1*, 1974, **70**, 1316.
80. J. Mu and D. Permuter, *Thermochimica Acta*, 1981, **49**, 207.
81. D. Dollimore, *J. Therm. Anal.*, 1992, **38**, 111.
82. G.F. Hüttig, *Kolloid-Z*, 1942, **98**, 6.
83. D. Dollimore and T.E. Jones, *J. Appl. Chem. Biotech.*, 1973, **23**, 29.
84. G. Tamman, *Z. Anorg. Chem.*, 1928, **176**, 46.
85. A. Donia, *Polyhedron*, 1997, **6**, 3013.
86. S. Bhattacharjee, M. Paria and H. Maiti, *Mat. Lett.*, 1992, **13**, 130.
87. H. Gopalakrishna, M. Subba Rao and T. Kutty, *J. Inorg. Nucl. Chem.*, 1976, **36**, 417.
88. A. Vos, J. Mullens, J. Yperman, D. Franco and L. Van Pouke, *Eur. J. Solid State Inorg. Chem.*, 1993, **30**, 929.
89. D. Wickham, *Inorg. Synth.*, 1967, **9**, 152.
90. W. Schuele, *J. Phys. Chem.*, 1959, **63**, 83.

91. P. Gallagher, *Thermochim. Acta*, 1993, **214**, 1.
92. Deyrieux, *Bull. Soc. Chim. Fr*, 1973, 25.
93. A. Donia and D. Dollimore, *Thermochim. Acta*, 1996, **290**, 139.
94. H. Langbein and S. Fischer, *Thermochim. Acta*
95. J. Stark and H. Wallace, *Chemistry Data Book*, 1970.
96. R.K. Sheline and H. Mahnke, *New Synth. Methods*, 1975, **3**, 203.
97. G.R. Dobson, *Acc. Chem. Res.*, 1976, **9**, 300.
98. W.W. Porterfield, *Inorganic Chemistry- A Unified Approach*, Academic Press, Inc., California, 1993
99. R. Colton and C.J. Commons, *Aust. J. Chem.*, 1975, **28**, 1673.
100. C.J. Commons and B.F. Hoskins, *Aust. J. Chem.*, 1975, **28**, 1663.
101. D.P.M. Mingos, I.N. Wilkinson, F.G.A. Stone and E.W. Able, eds., *Comprehensive Organometallic Chemistry*, Vol. 3, Pergamon Press Ltd., Oxford, UK, 1982, Chapter 19, 1-88.
102. K.G. Caulton and R.F. Fenske, *Inorg. Chem.*, 1968, **7**, 1273.
103. W. Hieber and T.Z. Kruck, *Z. Naturforsch*, 1961, **16B**, 709.
104. A. Ceriotti, *Angew. Chem. Int. Ed. Engl.*, 1985, **24**, 697.
105. D.M.P. Mingos, *Nature Phys. Sci.*, 1972, **236**, 99.
106. R. Brill, *Z. Kristallogr.*, 1931, **77**, 36.
107. L.F. Dahl and J.F. Blount, *Inorg. Chem.*, 1965, **4**, 1373.
108. C.H. Wei and L.F. Dahl, *J. Am. Chem. Soc.*, 1969, **91**, 1351.
109. F.A. Cotton and B.F.G. Johnson, *Inorg. Chem.*, 1974, **96**, 4155.
110. C.E. Anson, R.E. Benfield, A.W. Bott, B.F.G. Johnson, D. Braga and E.A. Marseglia, *J. Chem. Soc., Chem. Commun.*, 1988, 889.
111. D. Braga, C.E. Anson, A.W. Bott, B.F.G. Johnson and E.A. Marseglia, *J. Chem. Soc., Dalton Trans.*, 1990, 3517.
112. B.F.G. Johnson and A.W. Bott, *J. Chem. Soc., Dalton Trans.*, 1990, 2437.

113. B.F.G. Johnson, Y.V. Roberts and E. Parisini, *J. Chem. Soc., Dalton Trans.*, 1992, 2573.
114. S. Aime and D. Osella, *J. Organomet. Chem.*, 1981, **214**, C27.
115. M.R. Churchill and J.C. Fettinger, *Organometallics*, 1990, **9**, 446.
116. D.L. Smith, *J. Chem. Phys.*, 1965, **42**, 1460.
117. E.L. Muetterties and M.J. Krause, *Angew. Chem. Int. Ed. Engl.*, 1983, **22**, 135.
118. R. Psaro, C. Dossi, A. Fusi, R. Della Pergola, L. Garlaschelli, D. Roberto, L. Sordelli, R. Ugo and R. Zandoni, *J. Chem. Soc. Faraday Trans.*, 1992, **88**(3), 369.
119. D.A. Hucul and A. Brenner, *J. Am. Chem. Soc.*, 1981, **103**, 217.
120. J.J. Venter, A. Chen and M.A. Vannice, *J. Catal.*, 1989, **117**, 170.
121. J.J. Venter and M.A. Vannice, *J. Mol. Catal.*, 1989, **56**(1-3), 117.
122. I.M. Baibich, A.E. Gerbase, R.G. da Rose, L. Amaral and A. Vasquez, *Spectrochim. Acta*, 1989, **45**, 933.
123. K. Lazar, K. Matusek, J. Mink, S. Dobos, L. Guzzi, A. Vizi-Orosz, L. Marko and W.M. Reiff, *J. Catal.*, 1984, **87**, 163.
124. Z. Schay, K. Lazar, J. Mink and L. Guzzi, *J. Catal.*, 1984, **87**, 179.
125. F. Hugues, J.A. Dalmon, P. Bussiere, A.K. Smith, J.M. Basset and D. Olivier, *J. Phys. Chem.*, 1982, **86**, 5136.
126. D.A. Hucul and A. Brenner, *J. Phys. Chem.*, 1981, **85**, 496.
127. D. Rojas, P. Bussiere, J.A. Dalmon, A. Choplin, J.M. Basset and D. Olivier, *Surf. Sci.*, 1985, **156**(1), 516
128. R. Psaro, A. Fusi, R. Ugo, J.M. Basset, A.K. Smith and F. Hugues, *J. Mol. Catal.*, 1980, **7**(4), 511.
129. L. Guzzi, Z. Schay, K. Matusek, I. Bogyay and G. Steffler, *Stud. Surf. Sci. Catal.*, 1981, **7** (Pt: A, New Horiz. Catal.), 211.
130. L. Guzzi, Z. Schay, K. Matusek, I. Bogyay and G. Steffler, *Stud. Surf. Sci. Catal.*, 1981, **7** (Pt: A, New Horiz. Catal.), 418.
131. H.G. Cutforth and P.W. Selwood, *J. Am. Chem. Soc.*, 1943, **65**, 2414.
132. L.M. Fillman and S.C. Tang, *Thermochim. Acta*, 1984, **75**, 71.

133. C.R. Eady, B.F.G. Johnson and J. Lewis, *J. Chem. Soc., Dalton Trans.*, 1975, 2606.
134. B.F.G. Johnson, and J. Lewis, *Adv. Inorg. Chem. Radiochem.*, 1981, **24**, 225.
135. R.B. King, *J. Am. Chem. Soc.*, 1966, **88**, 2075.
136. R. Pince, R. Queau and D. Labroue, *J. Organomet. Chem.*, 1983, **249(2)**, 405.
137. R. Pince, R. Queau and D. Labroue, *J. Organomet. Chem.*, 1986, **306**, 251.
138. Deyrieux and Peneloux, *Merck Index*, 8th Edition, 456.
139. H. Okamoto, P.R. Subramanian, L. Kacprzak, eds., *ASM International - The Materials Information Society, Binary Alloy Phase Diagrams*, 2nd Edition, 1996.

APPENDIX I

The results of the IR spectroscopy analyses of the coprecipitated binary oxalates of the iron-cobalt and cobalt-nickel systems are given in Tables A1 and A2, respectively. Vibrational assignments were tentatively made by comparison with literature values [39, 42-47].

Table A.1: Infrared spectra and vibrational assignments for the Fe-Co coprecipitated binary oxalates in different molar ratios

Vibrational Assignment	Fe3:Co1 (cm ⁻¹)	Fe1:Co1 (cm ⁻¹)	Fe1:Co3 (cm ⁻¹)
v(OH ₂)	3352 br/s	3354 br/s	3365 br/s
v(OH ₂)	3110 m/sh	3160 m/sh	3110 m/sh
v _{as} (C=O)	1623 s	1612 s	1617 s
v _{sym} (C-O) + v(C-C)	1360 m	1361 m	1360 m
v _{sym} (C-O) + δ(O-C=O)	1315 m	1316 m	1317 m
v(O-M-O)	822 m	823 m	825 m
δ(O-C=O) + v(M-O)	765 m	769 m	755 m
v(O-M-O)	722 m	739 m	627 m
v(M-O) + v(C-C)	492 m	494 m	494 m

Table A.2: Infrared spectra and vibrational assignments for the Co-Ni coprecipitated binary oxalates in different molar ratios

Vibrational Assignment	Co3:Ni1 (cm ⁻¹)	Co1:Ni1 (cm ⁻¹)	Co1:Ni3 (cm ⁻¹)
v(OH ₂)	3375 br/s	3384 br/s	3386 br/s
v(OH ₂)	3110 m/sh	3144 m/sh	3110 m/sh
v _{as} (C=O)	1620 s	1623 s	1622 s
v _{sym} (C-O) + v(C-C)	1360 m	1360 m	1360 m
v _{sym} (C-O) + δ(O-C=O)	1315 m	1315 m	1315 m
v(O-M-O)	828 m	828 m	828 m
δ(O-C=O) + v(M-O)	765 m	746 s	755 m
v(O-M-O)	722 m	607 w	627 m
v(M-O) + v(C-C)	488 m	487 m	488 m

*br (broad); sh (shoulder); s (strong); m (medium); w (weak)